Patrik Kjell Ake Johansson

Investigations of Protein Fiber Structures and the Interactions at Their Interfaces Using Nonlinear Optical Spectroscopy

Patrik Kjell Ake Johansson

A dissertation

submitted in partial fulfillment of the

requirements for the degree of

Doctor of Philosophy

University of Washington

2018

Reading Committee:

David G. Castner, Chair

Patrick Koelsch

Dan Fu

Program Authorized to Offer Degree:

Bioengineering

University of Washington

Abstract

Investigations of Protein Fiber Structures and the Interactions at Their Interfaces Using Nonlinear Optical Spectroscopy

Patrik Kjell Ake Johansson

Chair of the Supervisory Committee:
Professor David G. Castner
Department of Bioengineering, Department of Chemical Engineering

Protein fibers are ubiquitous in nature, either as functional components of cells and tissues, or as hallmarks of severe diseases. Examples include amyloid fibers in the brain of patients with Alzheimer's disease, or collagen fibers in the extracellular matrix of tissues - central design targets for scaffolds in tissue engineering. Characterizing the structure and surface chemistry of protein fibers is therefore vital, but notoriously challenging due to their complexity. In this work, fundamental nonlinear optical properties of type I collagen fibers and amyloid structures from insulin and β-lactoglobulin have been investigated and used for structural characterization. The collagen fibers were characterized with vibrational sum-frequency scattering spectroscopy, in a first demonstration of this technique for protein fiber investigations. Spectral features were shown to be dependent on the scattering angle and the signals away from the phase-matched direction were highly reproducible for samples with random fiber orientations. Furthermore, a scattering

angle of 22° exhibits surface specificity for the fibers when probed in the amide I region, which was utilized to detect the initial effects of treatments with sodium dodecyl sulfate surfactants. Information from such studies of the fiber surface structure may complement the information gained from techniques with sensitivity for the overall structure, such as second-harmonic generation (SHG). For the amyloid structures, the intrinsic linear and nonlinear optical properties were investigated. In the amyloid state, β-lactoglobulin develops a weak fluorescence in the visible regime, which could be identified by tracking the red-edge excitation shift (REES). The intrinsic optical properties allowed imaging of amyloid spherulites from both proteins, with high contrast especially for the nonlinear techniques, which included SHG and two-photon excitation fluorescence (TPEF). By monitoring the total signal from insulin amyloid spherulites in two separate detection channels while shifting the excitation wavelength, indications of the REES in TPEF were observed for the first time. The nonlinear optical techniques and phenomena explored in this work opens up for label-free detection and detailed structural investigations of protein fibers in aqueous and biological 3D environments.

TABLE OF CONTENTS

LIST OF FIGURES

LIST OF TABLES

ACKNOWLEDGEMENTS

All collaborators and co-authors are thanked for their invaluable contributions towards the scientific results included in this dissertation. The work presented in the main body was supported by National Science Foundation Grant No. CBET-1125791 and National Institute of Health Grant No. EB-002027, to the National ESCA and Surface Analysis Center for Biomedical Problems. The Lynn and Mike Garvey Cell Imaging Lab is acknowledged for multiphoton microscope instrument time, for which supervision was provided by Dr. Ron Seifert and Dr. Dale Hailey. Dr. Paul Wiggins gave further advice on the imaging efforts and kindly provided lab space and equipment for cross-polarized microscopy of amyloid spherulites. I thank Dr. Olle Inganäs for personal financial support via the Knut and Alice Wallenberg Foundation, as well as Dr. Niclas Solin for the valuable discussions throughout this work. The work presented in the appendices was funded by the Knut and Alice Wallenberg Foundation, the Swedish Research Council, the National Science Foundation Grant No. ECC-1542101, as well as the aforementioned grant from the National Institute of Health.

DEDICATION

I thank my parents whose encouragement and passive support throughout my life's choices have been unwavering. Without them staying out of my way as I pursuit my dreams and passions, it is doubtful that this body of work would ever have come to pass. I also want to thank my sister, her children, my grandparents, and all my dear friends, without whom life would diminish in value and meaning. However, the ones I owe my biggest gratitude to are all the teachers and mentors that I have had through the years. Those that have inspired and made me curious about life and science and care about truths and facts. In particular, I want to mention Olle Östling, whose great humor and deep knowledge within biophysics, while teaching biology with a relaxed attitude at Forsmark's High School, inspired me to start my academic journey within the field of bioengineering. After completing my M.Sc. in bioengineering at Linköping University, Olle Inganäs kindly supported me for a year, which enabled me to expand my scientific horizon in his laboratory for biomolecular and organic electronics as well as pursue my personal academic goals. During this time, I had the privilege to frequently engage in discussions about science and life with Niclas Solin, an exercise we occasionally still enjoy whenever we get a chance to meet. The informal mentorship and formal support that Niclas has provided through the years have been invaluable. Finally, I want to thank my committee members, Dan Fu, Buddy Ratner, Dan Chiu, and Matthew Bush. The final two members, Patrick Koelsch and Dave Castner, have been my advisors during my time as a graduate student and I cannot thank them enough. Patrick introduced me with enthusiasm to the exciting world of nonlinear optics and taught me how to apply it for materials characterization. His positivism and great friendship have really been something special over the past years. Also, without Dave's support I would definitely not have been able to produce the work summarized in this dissertation. Dave's open mind to my ideas and unusual schedule has enabled me to be creative with a large amount of academic freedom. His broad knowledge within surface science and physical chemistry has also been a great source of inspiration. Patrick and Dave, it is obvious that you care deeply about your students – thank you for all the ways in which you have enriched my graduate school experience and helped me develop into a better scientist.

Chapter 1. INTRODUCTION

Part of this chapter is adapted with permission from a previously published review article (P.K. Johansson et al. *Topics in Catalysis*, Vol 61, Issue 9-11, pp 1101-1124, **2018**, DOI: 10.1007/s11244-018-0924-3). Copyright (2018) Springer Nature.

The structural integrity and mechanical properties of cells and tissues are to a large extent provided by protein fibers, such as collagen fibers that are an essential part of the extracellular matrix.[1-3] A detailed understanding of the structure, interaction, orientation, conformation, and dynamics of these fibers is key for the development of new and improved strategies in the fields of cell biology, materials science, tissue engineering and regenerative medicine.[4, 5] Other fibrillar structures, such as amyloids, are hallmarks for severe diseases like diabetes, Alzheimer's disease, and Parkinson's disease.[6, 7] Insights into how the environment affects their formation and how the mature fibers interact with their surrounding are essential for understanding disease development and could guide the pursuit of new drugs and biomarkers for these severe conditions.[8]

The natural environment for protein fiber structures is three-dimensional and includes aqueous solvents with a range of biomolecules. Therefore, analytical techniques capable to confirm the presence, orientation, conformation, and interactions of chemical groups at the surface of the fibers, as well as their overall structure, within this context is desired. For most techniques, there are often limitations and great challenges when characterizing the structure and surface chemistry of protein fibers. While X-ray photoelectron spectroscopy and time-of-flight secondary ion mass spectrometry provide detailed chemical information with high surface specificity,[9-12] the techniques typically require ultra-high vacuum and extensive sample preparation that may affect the targeted structures and limit the type of systems that can be studied. Similar limitations apply to electron microscopies, which are excellent for high-resolution imaging, but without chemical information. Quartz crystal microbalance with dissipation and surface plasmon resonance are label-free techniques capable of real-time probing of biomolecular interactions on solid/liquid interfaces,[13-17] but also without chemical specificity. Infrared (IR) and Raman spectroscopies, on the other hand, do provide chemical and some structural information;[18] however, the interfacial specificity is often poor or nonexistent. Furthermore, for samples in biological environments, IR spectroscopy suffers from high probe light absorption, while the low cross-section for spontaneous Raman scattering leads to weak signals overwhelmed by background and noise. The techniques mentioned above, and many others, have provided important information crucial for the understanding and development of protein fibers within certain contexts. However, additional techniques with both chemical and interfacial specificity, capable of analyzing biomaterials in aqueous 3D environments, are desired - something that can be realized with nonlinear optics.[19-23] Nonlinear optics is a field that includes a wide range of approaches for non-invasive characterization of materials with high-intensity lasers. Two-photon excitation fluorescence (TPEF) is commonly used for high-quality imaging with low background, while coherent anti-Stokes Raman scattering (CARS) as well as stimulated Raman scattering (SRS) can be performed in microscopy mode and provide images with contrast for specific molecular vibrations.[22] While powerful, these techniques typically lack specificity for interfacial features and ordered structures, which is one of the main strengths of second-harmonic generation (SHG) and sum-frequency generation (SFG).[20] The former is commonly used for label-free imaging of structures that exhibit long-range ordering (i.e. directionality of the molecular groups) in complex biological samples, while the latter is often employed in reflection-mode for vibrational spectroscopy of light-accessible interfaces. SFG typically requires the use of two-dimensional surface models, which has been and continues to be a very useful approach. However, it is not clear how accurately such models capture key characteristics, such as dynamics and interactions, of biomaterials normally found in three-dimensional biological environments. For instance, the curvature of structures may affect the packing, organization and dynamics of species at their surfaces. This can lead to behaviors that would not be predicted based on the results from two-dimensional surface models. Significant effects related to the curvature have been demonstrated for various structures, such as small nanoparticles and liposomes.[24-26]

The origin of the interfacial specificity in SHG and SFG is that net ordering of the probed transition dipole moments is required for strong responses, which normally precludes solvent molecules and other isotropically distributed bulk species from contributing to the signal.[19-21] However, when structures in the bulk of the sample scatter the mixing light beams away from the phase-matched direction, there will be a phase-shift across the scattering objects as well as a significant reduction in the coherence length of the signal. A consequence from this is that scatterers that include ordered species can produce signals detectable in the far field, even if they are isotropically arranged in the sample or if the structures are centrosymmetric.[27, 28] This opens up for spectroscopic analysis of ordered structures and interfaces of biomaterials that scatter the incidence light in biological environments. When applied in this mode, the techniques are called second-harmonic scattering (SHS) and sum-frequency scattering (SFS) and they were first introduced in the late 1990s and early 2000s, respectively.[29, 30] Specialized and expensive equipment as well as complex or non-existent theoretical models have been prohibitive factors for the application of SHS and SFS to samples of biological relevance. However, continuous efforts during the last decade have now provided empirical results and a theoretical framework that make analyses of more complex samples feasible. It is therefore one of the main aims of this work to explore and develop these techniques for the characterization of the structures and interfaces of various biomaterials in biological environments, in particular protein fibers.

1.1 NONLINEAR OPTICS

As mentioned above, nonlinear optics is a field that includes a broad range of techniques, which all have a nonlinear response to the total electric field intensity in the sample. The response is proportional to the square of the induced polarization as given by Eq. 1.1,

$$I \propto |P|^2 = \left|\varepsilon_0\left(\chi^{(1)}E_i + \chi^{(2)}E_iE_j + \chi^{(3)}E_iE_jE_k + \ldots\right)\right|^2 \qquad (1.1)$$

where I is the intensity of the response, P is the induced polarization, $\chi^{(n)}$ is the susceptibility factor for the nth order mixing, and E represents the electric fields of the incoming laser beams. Normally, the susceptibility factors for multi-order induced polarization are very small, leading to a dominating first-order linear response and only weak nonlinear effects. However, with strong peak electric fields realized with short pulsing and focusing of the incoming high-intensity lasers, the higher order terms start to contribute significantly to the induced polarization and detectable signals from these processes may be produced. Some of the processes commonly of interest in nonlinear optical spectroscopy are illustrated in Figure 1.1. In this work, SFG and SFS are of particular interest and thus discussed in more detail below in a separate section. However, to give a more complete introduction to the field of nonlinear optics, brief overviews of the other processes are first provided.

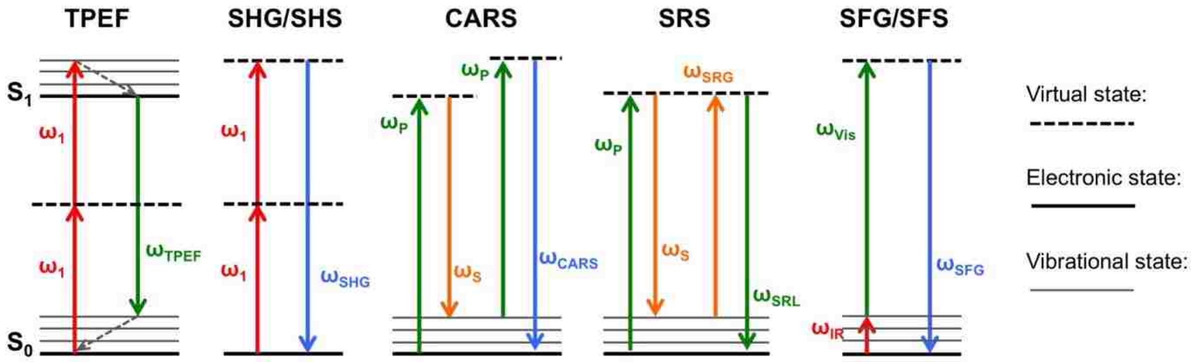

Figure 1.1. Diagrams of nonlinear optical processes.

1.1.1 *Two-Photon Excitation Fluorescence and Second-Harmonic Generation*

TPEF relies on simultaneous absorption of multiple photons by the same molecule. It usually involves a virtual state as an intermediate step to the real excited state that is being probed. TPEF is often performed in confocal scanning mode, where the short-pulsed excitation laser is focused down to one spot, from which the majority of the signal is produced due to the high photon flux in that spot. The quality of the image is given by the point spread function of the imaging system, for which the axial spread is much lower in TPEF compared to the corresponding linear fluorescence process.[31] This is because the signal has a multi-power dependence on the incoming laser intensity, leading to improved spatial resolution in the z-direction (depth-axis). As the excitation wavelength often can be in the IR or near-IR region, the so called "biological window", low absorption allows quite long penetration depths in biological samples and high excitation light intensities may be used while the risk for photo-induced sample damage or bleaching remains low - especially outside the focal plane where there is insufficient photon flux for significant absorption. Also, since the TPEF signal is at a wavelength shorter than the excitation wavelength, background and noise can be relatively low. These features, together with high depth-resolution, make TPEF an increasingly popular nonlinear optical tool for imaging of biological samples.[31-36]

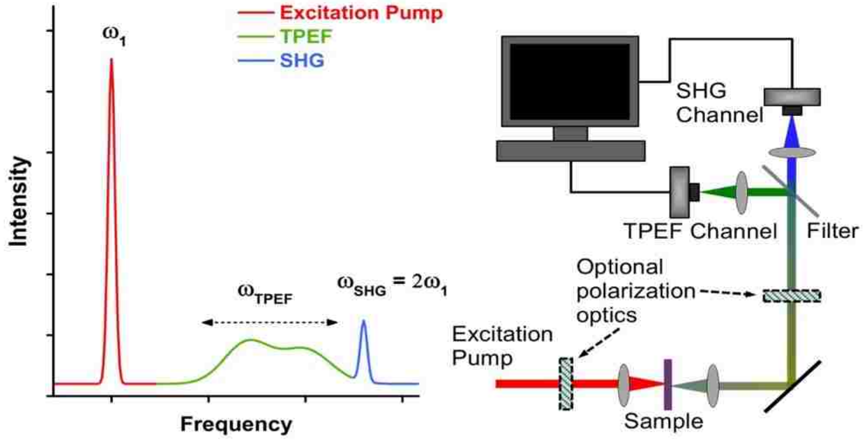

Figure 1.2. Overview of a setup for TPEF and SHG microscopy.

All the virtues of TPEF outlined above are also true for SHG and a schematic of a setup for the two techniques is provided in Figure 1.2. However, the techniques differ in some very important ways.[37-40] First, SHG is a parametric process and does not rely on absorption of photons; however, resonant enhancement of the signal via transitions to real energy levels of the molecules can still occur. Second, electronic relaxation can happen to a variety of vibrational states in TPEF and leads to quite broad spectra, while the parametric SHG process instantaneously yields a signal at the double frequency of the excitation laser light, leaving the system unperturbed. As a consequence, the vibrational relaxation in the excited and ground states yields a Stokes shift in TPEF, which is not the case for SHG. Third, while SHG is a coherent process and exhibits a range of selection rules for the sample symmetry, the broad bandwidth and long lifetime of TPEF destroy the coherence and thereby relax those selection rules. While these distinctions between SHG and TPEF are somewhat related, the final point is particularly important, as it is the origin of the interfacial specificity for coherent, even-ordered nonlinear optical processes. In accordance with Eq. 1.2, the intensity of the SHG signals can be described by

$$I_{SHG} \propto |P_{SHG}|^2 = \left|\varepsilon_0(\chi_{SHG}^{(2)}E^2)\right|^2 \tag{1.2}$$

where E is the electric field of the incoming laser light and $\chi_{SHG}^{(2)}$ is the susceptibility tensor for the SHG process, which can be divided into 27 different tensor elements, $\chi_{ijk}^{(2)}$, where the ijk goes over all possible combinations of the lab coordinates x, y and z.[39, 40] In this notation, *i* represents the electric field direction of the SHG signal, while *j* and *k* represent the electric field directions of the two incoming laser photons in the mixing process. If one inverts the sample that is probed, it is clear that one consequence is that all molecules would experience a flip in sign of all the electric field components that mix in the process, including the electric field of the SHG signal. In other words, a positive induced polarization should become negative under this operation, which requires $\chi^{(2)}_{SHG}$ to flip its sign according to Eq. 1.2. However, if the sample is isotropic, the inversion should yield a situation that is macroscopically indistinguishable from the starting point. Since $\chi^{(2)}_{SHG}$ is a macroscopic sample property, it should therefore not change. The only way $\chi^{(2)}_{SHG}$ can flip in sign and simultaneously keep its value is if it is zero for isotropic samples. A more physical way of looking at this is that for each molecule with its dipole moment in a certain direction, another molecule will exist within the coherence length that is positioned and/or orientated so that it effectively cancels out the signal from the first in an isotropic sample. Such signal cancellation requires the process to be coherent, which connects the phenomenon to the third point made earlier with respect to the differences between TPEF and SHG. A more detailed discussion on the selection rules for sample symmetries is included in the section about vibrational SFG spectroscopy, which is broadly applicable also to SHG. As samples with inversion symmetry do not yield SHG signals, it is an excellent method for label-free detection and/or imaging of non-centrosymmetric structures that exhibit long-range ordering (and that are thus non-isotropic). One example is collagen fiber networks in tissues and many publications that include high-contrast SHG images are available in the scientific literature.[37, 41-48] In addition to imaging, structural analysis of the fibers is possible by relating the relative signal intensities for various polarization directions of the incoming laser beams to the contribution of various SHG tensor elements for the sample. This can identify the type of collagen in the sample and provide molecular level details, such as the pitch angle (tilt relative the fiber axis) for the carbonyl group of the peptide unit or the methylene groups in the side chains.[48, 49]

1.1.2 *Coherent anti-Stokes Raman Scattering and Stimulated Raman Scattering*

While SHG and TPEF can provide images with high structural contrast, they typically do not provide contrast with molecular specificity. However, CARS and SRS, two nonlinear vibrational spectroscopy methods, are commonly used for imaging with high sensitivity and can provide chemical information with high spatial resolution. CARS is a coherent parametric 3rd-order process, in which one intense laser beam acts as pump and probe (called pump from here on), while a second tunable laser acts as a Stokes beam that guides the molecules to select Raman active vibrations.[50-53] The signal intensity is thus described by

$$I_{CARS} \propto |P_{CARS}|^2 = |\varepsilon_0(\chi_{CARS}^{(3)} E_P^2 E_S)|^2 \tag{1.3}$$

where $\chi_{CARS}^{(3)}$ is the nonlinear susceptibility factor for the CARS process, E_P is the electric field of the pump beam, and E_S is the electric field of the Stokes beam. Being an odd-ordered process, the flip in sign of the induced polarization for an inversed sample is already realized by the sign switch for E_P and E_S, allowing $\chi_{CARS}^{(3)}$ to be non-zero even for isotropic samples. Therefore, CARS is not surface or interface specific. A more physical way of looking at it is that the beating frequency between the pump and Stokes beams ensures that the vibrational modes of the stimulated Raman resonances oscillate so that the emitted CARS photons have the same phase regardless of molecular orientation or position - analogous to how stimulated emission in a laser leads to a build-up of photons with the same phase. Therefore, no cancellation of signals will occur, even if the sample is isotropic. Ignoring possible contributions from resonant electronic transitions, the nonlinear susceptibility factor is given by

$$\chi_{CARS}^{(3)} = \chi_{NR}^{(3)} + \sum_q \frac{A_q}{\omega_q - (\Omega) - i\Gamma_q} \tag{1.4}$$

where $\chi_{NR}^{(3)}$ is a nonresonant contribution, A_q, Γ_q and ω_q are the amplitude, width and wavenumber of the qth Raman active vibrational mode, while $\Omega = \omega_P - \omega_S$ is the difference frequency between the pump and Stokes beams. $\chi_{CARS}^{(3)}$ is a rank four tensor and the magnitude of A_q is dependent on the total contribution of the tensor elements (γ_{abcd}) of the molecular hyperpolarizabiliy (also a rank four tensor) to the nonlinear susceptibility tensor elements probed with the chosen polarization combination. When the difference frequency equals the frequency of a Raman transition, ω_q, a signal enhancement will occur at the CARS frequency,

$$\omega_{CARS} = 2\omega_P - \omega_S \tag{1.5}$$

where ω_P and ω_S are the frequencies of the pump and Stokes beams, respectively. The CARS photons add up coherently in the far field, which yields a quadratic dependence on the number of probed molecules. This feature, together with the nonresonant contribution to $\chi^{(3)}_{CARS}$ as well as the imaginary component of the resonant parts that yield phase-relations, leads to CARS line shapes that typically differ from those in spontaneous Raman spectra. While this is not a problem in itself, the nonresonant contribution makes spectroscopic interpretation more difficult and limits the spectral contrast, in particular for the amide I and fingerprint regions. This is challenging to circumvent in a reliable and robust way. However, one method is to utilize the nonresonant background as a heterodyne amplification signal and post-process the data to retrieve the imaginary part of the CARS signal via a time-domain Kramers-Kronig transform.[54, 55] A setup for this that includes a three-color excitation scheme with broad-band pump/Stokes beams and a narrowband probe beam was previously reported.[53] Despite the difficulties with nonresonant backgrounds, CARS microscopy is commonly used for imaging of specific chemical groups in biological samples and has provided much useful information. High-contrast imaging of myelin fibers in brain tissue[56] and the identification of lipids co-localized with fibrous amyloid plaques in Alzheimer's diseased human brain tissue[57] are two examples.

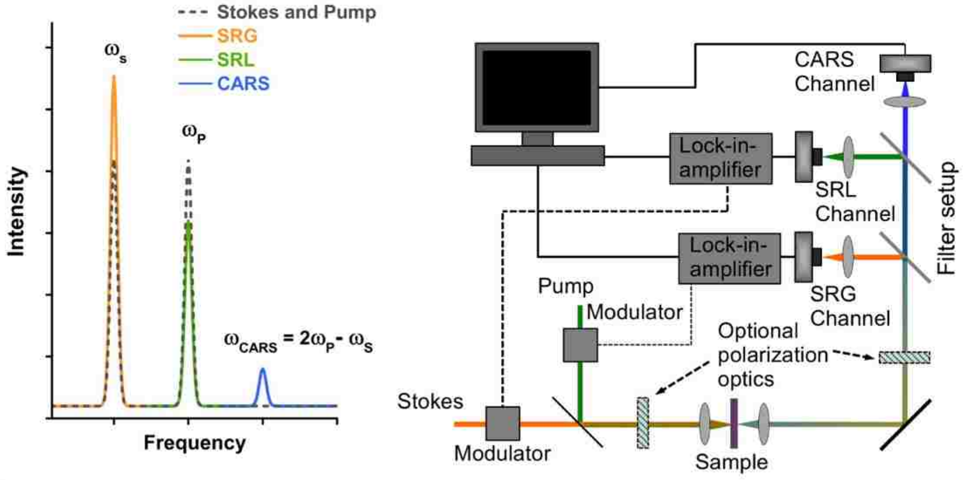

Figure 1.3. Overview of a setup for CARS and SRS microscopy.

Figure 1.3 includes the schematic of a setup for CARS, as well as another 3rd-order coherent Raman scattering process called SRS, where the frequency of the induced polarization matches either the pump frequency or the Stokes frequency (sometimes called probe frequency). In the far field, the produced SRS signal will interfere with and thereby modulate the intensity of the pump or Stokes beams in accordance with,

$$I_{SRS} = |E_i + E_{SRS}|^2 \tag{1.6}$$

where E_{SRS} is the electric field of the SRS. For SRS signals with the same frequency as the pump beam, E_i denotes the pump electric field, E_P. In this case, the phase difference between the interfering fields is -π/2, which leads to a signal loss at the pump frequency. This stimulated Raman loss (SRL) is then dependent on E_P and the Stokes electric field E_S in the following way,

$$I_{SRL} = |E_P|^2 + |E_{SRS}|^2 - 2|E_P^2||E_S^2|Im\{\chi_{SRS}^{(3)}\} \tag{1.7}$$

If the SRS signals instead occur at the same frequency as the Stokes beam, E_i denotes the Stokes electric field, E_S. The phase difference between the interfering fields in this case is +π/2, which leads to a signal gain at the Stokes frequency. The dependence of the stimulated Raman gain (SRG) on E_P and E_S is thereby described by

$$I_{SRG} = |E_S|^2 + |E_{SRS}|^2 + 2|E_P^2||E_S^2|Im\{\chi_{SRS}^{(3)}\} \quad (1.8)$$

Normally, the pump and Stokes beams are much more intense than any nonresonant background signals, which eliminates potential problems with interference between $\chi_{NR}^{(3)}$ and the resonant components of $\chi_{SRS}^{(3)}$. However, one problem with detection at these frequencies is laser intensity noise. Such noise is mainly of low frequency, which means that a rapid modulation (>1 MHz) of the non-detected beam's intensity (or frequency, phase, wavelength, and polarization) will yield a signal modulation of the other beam that can be identified and detected with a lock-in amplifier. Such a detection scheme can reduce the noise of the system down to the shot noise level of the detector. While the loss and gain signals have a quadratic dependence on both the incoming pump and Stokes E-fields (which can be normalized away), the dependence on the molecular concentration is linear. This together with the absence of nonresonant background signals mean that, in contrast to CARS, the SRS line shape will be identical to conventional spontaneous Raman spectra. SRS data can thus be fitted with regular Lorentzian functions and one can easily show that the imaginary part of the resonant 3rd-order susceptibility in Eq. 1.4 (which also applies to SRS) has a Lorentzian line shape. The doubly intensity dependence on the pump and probe beams ensures that the signal is only produced from the focus spots of the lasers, which allows for optical sectioning in 3D, just as in TPEF and SHG microscopy. The above virtues of the technique have resulted in the number of SRS publications focused on imaging biological samples increase rapidly, despite it being less than a decade since the first demonstration on such materials.[58-60] An important comment is that although the diagram of the SRS process in Figure 1.1 appears to be parametric, it is actually not since less energetic photons at the Stokes frequency are produced at the expense of the more energetic ones at the pump frequency, making the process dissipative. In other words, energy in the form of excited molecular vibrations is deposited into the sample.

Although local molecular ordering is not a requirement for CARS and SRS signal production, the angle between the induced dipole moments and the mixing E-fields is still important for the ability of the molecules to produce a signal. Therefore, it is theoretically possible to extract the local average orientation for molecules with these techniques by using various polarization directions for plane-polarized pump and Stokes beams.[61-63] Techniques based on CARS and SRS are thus growing increasingly popular for detailed molecular characterization of biomaterials. In recent years, multiplex versions have been developed, combining a picosecond narrowband laser with a femtosecond broadband laser. The narrowband laser ensures high spectral resolution, while the broadband gives the bandwidth for multiplex acquisition and this allows rapid detection of spectra enabling studies of dynamic processes in real time. Some technical difficulties with multiplex SRS, associated with the lock-in-amplifier detection, have prompted further developments. For instance, chirped femtosecond laser pulses where the well-controlled temporal delay between them determines the beat-frequency have successfully been used for rapid hyperspectral SRS imaging.[64]

1.1.3 *Sum-Frequency Generation*

The first reports of vibrational SFG spectroscopy were published in 1987.[65-67] It is a 2nd-order process that exhibits similar selection rules as SHG, which means that isotropic samples typically do not yield a signal. As molecules tend to order themselves and thereby yield sample anisotropy at interfaces, SFG is considered interfacial sensitive. The technique utilizes one visible (or near IR) laser beam at a fixed narrowband frequency and one tunable (narrowband or broadband) IR laser beam. The pulsed and high-intensity beams need to be overlapped spatially and temporally on the sample, from which the produced SFG signal intensity then is given by

$$I_{SFG} \propto |P_{SFG}|^2 = \left|\varepsilon_0 \chi_{SFG}^{(2)} E_{\omega_{Vis}} E_{\omega_{IR}}\right|^2 \tag{1.9}$$

where $\chi^{(2)}_{SFG}$ is the effective susceptibility factor for SFG, while $E_{\omega_{Vis}}$ and $E_{\omega_{IR}}$ are the electric fields of the visible and IR laser beams respectively. Just as for SHG, $\chi^{(2)}_{SFG}$ is a tensor that can be divided into 27 tensor elements.[40] Vibrational SFG spectroscopy are traditionally performed in both reflection mode and transmission mode, of which the former is the most common for surface studies.[68, 69] For such experiments, the SFG-active vibrational modes can be probed at any interface accessible by the visible and IR beams; for example solid/liquid, solid/air and liquid/air interfaces in geometries illustrated in Figure 1.4.

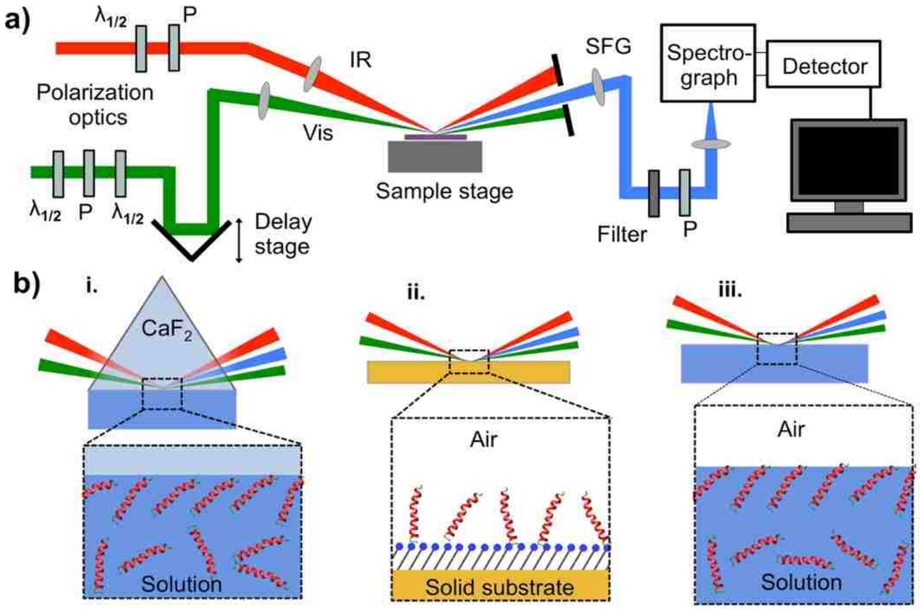

Figure 1.4. Overview of setups for SFG spectroscopy. a) Typical beam geometries for probing a sample on a sample stage. b) SFG is capable to probe the solid/liquid, solid/air, and liquid/air interface, if accessible by the mixing beams.

In SFG experiments, it is possible to control the polarization state of the SFG, visible, and IR beams, and thereby probe only a subset of the 27 possible $\chi^{(2)}_{ijk}$ tensor elements (where i is the direction of the SFG electric field, j is the direction of the visible electric field, and k is the direction of the IR electric field). Using the notation of p-polarization for electric fields oscillating in the x-z incidence plane, and s-polarization for electric fields oscillating in the perpendicular y-direction, there are eight possible settings with clean polarization states of the three mixing beams. The corresponding effective susceptibilities, $\chi^{(2)}_{eff}$, probed and the tensor elements, $\chi^{(2)}_{ijk}$, they include are outlined in Table 1.1, as well as the rules for the various tensor elements for a few common interfacial symmetries. Observe that the achiral and chiral assignments assume that a sample symmetry line is aligned with the plane of incidence.

Table 1.1. The tensor elements probed by the effective susceptibilities. Observe that the achiral and chiral assignments assume that a sample symmetry line aligns with the incidence plane.

$\chi^{(2)}_{eff}$	**ijk of probed $\chi^{(2)}_{ijk}$**	**ijk of the non-vanishing $\chi^{(2)}_{ijk}$ depending on the sample symmetry**		
		symmetry	*achiral elements*	*chiral elements*
$\chi^{(2)}_{ppp}$	zzz, zxx, xzx, xxz xxx, xzz, zxz, zzx	C_1	All tensor elements are nonvanishing and independent.	
$\chi^{(2)}_{ssp}$	yyz, yyx	C_2	zzz, zxx, xzx, xxz, yyz, yzy, zyy	xzy, zxy, xyz, zyx, yxz, yzx
$\chi^{(2)}_{sps}$	yzy, yxy	C_{2v}	zzz, zxx xzx, xxz, yyz, yzy, zyy	–
$\chi^{(2)}_{pss}$	zyy, xyy	C_3	xxy = xyx = yxx = -yyy, xxz = yyz xyy = yxy = yyx = -xxx, xzx = yzy zxx = zyy, zzz	xzy = -yzx, zxy = -zyx, xyz = -yxz
$\chi^{(2)}_{sss}$	yyy	C_{3v}	xyy = yxy = yyx = -xxx, xxz = yyz xzx = yzy, zxx = zyy, zzz	–
$\chi^{(2)}_{pps}$	xzy, zxy, zzy, xxy	C_4; C_6; C_∞	zzz, zxx = zyy, xzx = yzy, xxz = yyz	xzy = -yzx, zxy = -zyx, xyz = -yxz
$\chi^{(2)}_{psp}$	xyz, zyx, zyz, xyx	C_{4v}; C_{6v}; $C_{\infty v}$	zzz, zxx = zyy, xzx = yzy, xxz = yyz	–
$\chi^{(2)}_{spp}$	yxz, yzx, yzz, yxx	D_∞	–	xzy = -yzx, zxy = -zyx, xyz = -yxz

When molecules adsorb on an interface, they often do so with a preferred orientation relative to the surface normal due to intermolecular forces, such as electrostatics, dipole-dipole interactions and hydrogen bonds. However, such interactions do not normally lead to long-range net directionality of the molecules within the x-y interfacial plane. In this case, the probed molecular groups in a sample would exhibit azimuthal isotropy with an average tilt angle, θ, at the interface. Such samples can be rotated by any angle around their z-axis (surface normal) without changing the value of the tensor elements. This is called C_∞ symmetry, for which it is easy to show that many of the $\chi^{(2)}_{ijk}$ tensor elements must be zero and the non-vanishing ones are the seven achiral elements $\chi^{(2)}_{xxz} = \chi^{(2)}_{yyz}, \chi^{(2)}_{xzx} = \chi^{(2)}_{yzy}, \chi^{(2)}_{zxx} = \chi^{(2)}_{zyy}, \chi^{(2)}_{zzz}$, and the six chiral elements $\chi^{(2)}_{xyz} = -\chi^{(2)}_{yxz}$,

$\chi^{(2)}_{xzy} = -\chi^{(2)}_{yzx}, \chi^{(2)}_{zxy} = -\chi^{(2)}_{zyx}$. The six latter are the tensor elements with perpendicular directions for all the electric fields of the mixing beams, for which only samples with intrinsically chiral groups or chiral organizations of (coupled or uncoupled) achiral groups can have nonzero values.[70] A surface without such chiral contributions will have vertical mirror symmetry, $C_{\infty v}$, in which case only the first seven achiral elements can be nonzero. However, biomolecules - such as proteins - often include chirality. The fact that it is possible to selectively probe the chiral vibrations with the *psp*, *spp*, or *pps* polarization combinations, can facilitate the assignment of detected spectral features and the structural analysis of such samples.[71-74] For instance, it has been shown that α-helices in several proteins and peptides exhibit achiral but not chiral signals in the amide I region, while β-sheets produce amide I signals in both the achiral and chiral polarization combinations. If azimuthal isotropy (C_∞, $C_{\infty v}$, or D_∞) is not part of the symmetry of the interface, or if the molecular groups have a preferred twist angle at the interface, it can become possible for achiral molecular hyperpolarizabilities to contribute to the chiral macroscopic nonlinear susceptibility tensor elements. In such cases, macroscopic SFG chirality is not automatically synonymous to interfacial molecular chirality.

As mentioned above, the SFG susceptibility is a macroscopic sample property. However, there is a connection between $\chi^{(2)}_{ijk}$ and the microscopic hyperpolarizability, β_{abc}, of the vibrational modes of the individual molecules in the sample. β_{abc} is also a tensor with 27 tensor elements that scale with the changes in polarizability, α_{ab}, as well as the dipole moment, $\vec{\mu}_c$, along the normal mode coordinate, Q_q, for the q^th vibrational mode.

$$\beta_{abc,q} \propto \frac{\partial \alpha_{ab}}{\partial Q_q} \frac{\partial \vec{\mu}_c}{\partial Q_q} \qquad (1.10)$$

This means that a vibrational mode must be both Raman and IR active in order to have a nonzero $\beta_{abc,q}$ and exhibit signal enhancement in a vibrational SFG spectrum. It also means that the relative strengths of the hyperpolarizability tensor elements of a vibrational transition can be estimated by quantum mechanical calculations of its change in polarizability and transition dipole moment.[75] This is often helpful for the interpretation of SFG spectra,[76-79] as the tensor elements of the nonlinear susceptibility probed in an SFG experiment can be described as a linear combination of $\beta_{abc,q}$ according to Eq. 1.11,

$$\chi^{(2)}_{ijk,q} = N \sum_{a,b,c} \langle R_{ia} R_{jb} R_{kc} \rangle \, \beta_{abc,q} \tag{1.11}$$

where N is the number density of the probed molecules, while $\langle R_{ia} R_{jb} R_{kc} \rangle$ are elements from the average transformation matrices that rotate each $\beta_{abc,q}$ element in the molecular coordinate system (x', y' and z') onto the i, j, and k coordinates of the lab coordinate system (x, y, and z). As the probed effective susceptibility is a linear combination of the $\chi^{(2)}_{ijk,q}$ elements, which in turn are a linear combination of $\beta_{abc,q}$, the line shape of a vibrational SFG spectrum is dictated by the line shape of the probed hyperpolarizabilities. When the SFG signal and the visible laser beam are far off-resonance from electronic transitions, the line shape of $\beta_{abc,q}$ is a Lorentzian curve with a real and an imaginary component, plus a potential nonresonant background. The following function is then used to fit the effective nonlinear susceptibility of an SFG spectrum,

$$\chi^{(2)}_{SFG} = \chi^{(2)}_{NR} + \sum_q \frac{A_q}{\omega_q - \omega_{IR} - i\Gamma_q} \tag{1.12}$$

where $\chi^{(2)}_{NR}$ is the nonresonant contribution, A_q, Γ_q and ω_q are the amplitude, width and frequency of the q^th vibrational mode, and ω_{IR} is the frequency of the infrared beam. It can here be seen that the chemical specificity of vibrational SFG spectroscopy arises from a signal enhancement when the IR light matches a Raman and IR active vibrational mode with a net orientation at the interface. It is also apparent that the resonant contributions are complex, which allows for interference between neighboring peaks, or with the nonresonant signal.

$$\begin{pmatrix} R_{xx'} & R_{xy'} & R_{xz'} \\ R_{yx'} & R_{yy'} & R_{yz'} \\ R_{zx'} & R_{zy'} & R_{zz'} \end{pmatrix} = \begin{pmatrix} \cos\psi & -\sin\psi & 0 \\ \sin\psi & \cos\psi & 0 \\ 0 & 0 & 1 \end{pmatrix} \begin{pmatrix} \cos\theta & 0 & \sin\theta \\ 0 & 1 & 0 \\ -\sin\theta & 0 & \cos\theta \end{pmatrix} \begin{pmatrix} \cos\phi & -\sin\phi & 0 \\ \sin\phi & \cos\phi & 0 \\ 0 & 0 & 1 \end{pmatrix} \tag{1.13}$$

The matrices above include a rotation of ψ (twist angle) around the molecular z' axis, a rotation of θ (tilt angle) towards the lab z coordinate, and a rotation of ϕ (azimuthal angle) around the lab z coordinate. This represents the transformation from the molecular hyperpolarizability to the lab coordinate system mentioned above and the appropriate matrix elements that go into Eq. 1.11 are defined on the left-hand side. If we consider molecular groups with inherent C_{3v} symmetry, such as methyl groups, adsorbed at an interface with isotropic azimuthal and twist angles (i.e. $C_{\infty v}$ interfacial symmetry), the non-zero nonlinear susceptibility tensor elements for the asymmetric stretches in the sample will depend on the molecular tilt as described in Eqs. 1.14-1.16.[40]

$$\chi^{(2)}_{zzz} = N[\langle\cos\theta\rangle - \langle\cos^3\theta\rangle]\beta_{z'x'x'} \tag{1.14}$$

$$\chi^{(2)}_{xxz} = \chi^{(2)}_{yyz} = \frac{N}{2}[\langle\cos^3\theta\rangle - \langle\cos\theta\rangle]\beta_{z'x'x'} \tag{1.15}$$

$$\chi^{(2)}_{xzx} = \chi^{(2)}_{yzy} = \chi^{(2)}_{zxx} = \chi^{(2)}_{zyy} = \frac{N}{2}\langle\cos^3\theta\rangle\beta_{z'x'x'} \tag{1.16}$$

The effective susceptibilities probed by different polarization combinations include unique subsets of these tensor elements, as shown in Table 1. For the case of CH_3 vibrations, which is discussed above, it is convenient to consider the signals defined by the effective susceptibilities $\chi^{(2)}_{ssp}$ and $\chi^{(2)}_{sps}$, for which the full expressions are

$$\chi^{(2)}_{ssp} = L_{yy,SFG}L_{yy,Vis}L_{zz,IR}\sin\alpha_{IR}\,\chi^{(2)}_{yyz} \tag{1.17}$$

$$\chi^{(2)}_{sps} = L_{yy,SFG}L_{zz,Vis}L_{yy,IR}\sin\alpha_{Vis}\,\chi^{(2)}_{yzy} \tag{1.18}$$

where $L_{ii,j}$ are the Fresnel factors for the respective beams and α_j are the incidence (or reflection) angles relative the surface normal, which is needed to get the z-components of the *p*-polarized IR and visible beams via $\sin\alpha_j$ ($\cos\alpha_j$ would be needed for x-components). Provided that the interfacial Fresnel coefficients can be estimated, it is thus possible to directly relate the ratios of peaks obtained in *ssp* and *sps* polarization combinations with the corresponding ratio of two unique tensor elements for the sample, which contain information about the tilt angle of the CH_3 groups.[80-84] Similar analyses have been performed for the secondary structures in proteins, such as enzymes immobilized on surfaces.[85-89] One thing to keep in mind is that the angle brackets in Eqs. 1.14 - 1.16 represent cosine averages of the angle distributions, which usually can be well approximated with gaussian distribution functions. However, if the widths of these distributions are broad, all average tilt angles converge to approximately the same ratio for the tensor elements. This means that even small experimental uncertainties will yield inconclusive results, as a broad range of average tilt angles will be in agreement with the data. This can be a problem for systems where a range of orientations are already inherently included in the structure of interest, such as large proteins with hundreds of peptide units and CH_x groups in various directions. However, as mentioned above, $\beta_{abc,q}$ can be theoretically evaluated and recent developments in SFG theory now allow such quantum mechanical calculations for proteins, based on their structure from crystallography data or molecular dynamic simulations. This enables simulations of SFG spectra in various polarization combinations as a function of the protein orientation. By converging the line shapes from the simulation with the spectra obtained experimentally in various polarization combinations, it is possible to get a detailed molecular level description of the sample corroborated by SFG data.[75, 78, 79, 89]

One issue with traditional (homodyne) SFG is the inability to distinguish between orientations rotated by 180°. As a consequence, there is always an ambiguity regarding the positive and negative directions of the sample symmetry axis. However, one can conclusively determine the direction of the probed molecular groups by performing phase-resolved (heterodyne) SFG.[79, 90-92]

The idea is to let the signals from the sample interfere with a time-delayed non-resonant signal from a local oscillator. The resulting signal is described by

$$I_{SFG} = |E_{LO} + E_R|^2 = |E_{LO}|^2 + |E_R|^2 + E_R E_{LO}^* + E_R^* E_{LO} \quad (1.19)$$

$$E_R E_{LO}^* + E_R^* E_{LO} \propto \chi_{SFG} A_{LO} e^{i(\varphi+\omega\tau)} + \chi_{SFG}^* A_{LO} e^{-i(\varphi+\omega\tau)} \quad (1.20)$$

where A_{LO} is the amplitude of the local oscillator field E_{LO}, χ_{SFG} is the SFG nonlinear susceptibility, φ is the phase difference between the resonant SFG field E_R and E_{LO} at zero time delay, while $\omega\tau$ represents an additional phase for E_{LO} due to a delay of τ between the two signals. The cross terms on the right hand side of Eq. 1.19 represent the phase-sensitive SFG signal, which is enhanced by a strong local oscillator signal. Inverse Fourier transformation of the SFG signal from the frequency domain into the time domain separates the cross terms by +τ and -τ, respectively, which allows selective filtering to isolate one of them. After Fourier transforming the chosen cross term back to the frequency domain, the complex $\chi_{SFG}^{(2)}$ can be retrieved by division through the corresponding signal of a purely nonresonant spectrum (e.g. gold, quartz or GaAs), since E_{NR} often can be considered a constant that just carries the information of E_{LO}. Retrieving the imaginary part of the complex $\chi_{SFG}^{(2)}$ in this way is particularly useful for resolving the ambiguity for molecular orientations in a sample, as the sign for each resonant peak is independent of the wavenumber and directly informs about the positive and negative direction of the sample symmetry axis. However, deducing the exact molecular orientations angles with precision still requires knowledge of the molecular hyperpolarizability tensor elements and further analysis of the signal strengths and/or line shapes in various polarization combinations.

In summary, SFG has high interfacial specificity and sensitivity, and provide detailed information about samples due to the selection rules and phase-relations discussed above. It is an increasingly popular tool for analysis of biomolecules at interfaces. The technique has been used to probe the orientation and structure of proteins[93-102] as well as protein fiber formation at interfaces,[103-106] the phase transitions and vanishing asymmetries via flip-flopping in supported lipid bilayers,[107-109] the surface chemistry of functionalized nanoparticles,[110, 111] the orientation and hybridization of DNA at interfaces,[112-115] the signatures of molecular substrates through living cells,[116-118] and many other systems of biological relevance.[119, 120] SFG has also been used for imaging, with similar virtues as in SHG microscopy, but with contrast for specific chemistries.[121, 122] Recently, a collinear heterodyne setup capable of phase sensitive SFG microscopy was reported, which can be used to characterize spatially heterogeneous surfaces and get local molecular orientations with relatively high resolution.[123] However, SFG in reflection or transmission mode cannot readily probe interfaces in three-dimensional environments that are isotropic on long scales. This is the case for many types of biomaterials, for which signals may be produced via scattering processes instead. This is the topic of the next and final section of this introduction into the theory and application of nonlinear optics for interfacial and structural analysis.

1.1.4 *Sum-Frequency Scattering*

Both SHG and SFG can be performed in scattering mode, abbreviated SHS and SFS respectively, which allows spectroscopic investigation of ordered regions and interfaces of scattering structures in bulk environments. This can be done even for centrosymmetric structures that are isotropically arranged, such as spherical particles in suspension for which there are numerous examples in the scientific literature.[27-30, 124-149] Examples with SHS include monitoring of molecular adsorption onto gold nanoparticles[124, 135] and the molecular transport across liposome bilayers,[125-127] while examples for SFS include the orientation and state of water at hydrophobic interfaces.[136, 141] There are two key principles that make these techniques possible for these types of samples. The first is a phase-shift for the mixing beams across the scattering object due to a difference in path length at angles away from the phase-matched direction, which ensures that signals from molecular groups with opposite orientations on either side of the object will not completely cancel each other out in the far field. Figure 1.5 illustrates an example of this for spherical structures. The second principle is that signals scattered at an angle away from the phase-matched direction have a significantly reduced coherence length. This means that a higher concentration of isotropically arranged scatterers is allowed before the average distance between them leads to signal cancelation, as they start to contribute coherently to the signal. However, signal production still requires local ordering of the probed vibrational modes within, or on the surface of, each scatterer. This leads to a quadratic dependence on the number density of molecules that contribute coherently to the signal from each scattering object. In contrast, there is a linear dependence on the concentration of the scattering object, as the signal is the incoherent sum of their individual contributions (up to the point where their average distance to each other falls below the coherence length). Qualitatively, the connection between SHG and SHS is similar to the connection between SFG and SFS. Therefore, only the latter case will be discussed below, as SFS is one of the key techniques in this dissertation.

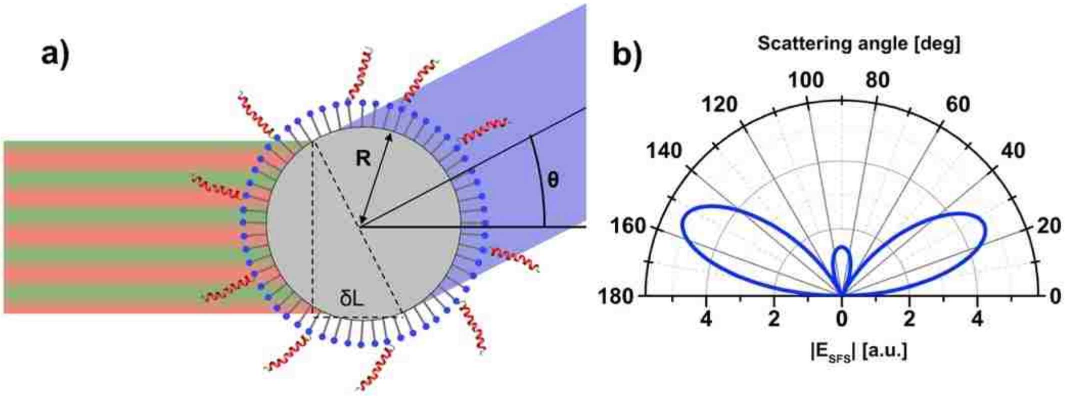

Figure 1.5. Illustration of SFS from a particle. a) With a colinear setup, the SFS signal is produced thanks to a phase-shift across the particle diameter due to different traveling paths at scattering angles >0°. b) A simulated scattering pattern with several maxima at angles away from the phase-matched direction (0°).

For the case where molecules on the surface of particles are probed, the tensor elements of the effective susceptibility for SFS (for which the symbol $\Gamma_{SFS}^{(2)}$ is used) will be a linear combination of the effective susceptibilities for SFG on a corresponding planar interface with the molecules oriented similarly relative to the surface normal.[30, 142, 145] In other words, it is possible to use equations similar to the ones for SFG to fit SFS spectra, with parameters representing the corresponding physical quantities (see Eqs. 1.9 and 1.12).

$$I_{SFS} \propto |P_{SFS}|^2 = \left|\varepsilon_0 \Gamma_{SFS}^{(2)} E_{\omega_{Vis}} E_{\omega_{IR}}\right|^2 \tag{1.21}$$

$$\Gamma_{SFS}^{(2)} = \Gamma_{NR}^{(2)} + \sum_q \frac{A_q}{\omega_q - \omega_{IR} - i\gamma_q} \tag{1.22}$$

A theoretical framework for calculating the expected SFS scattering patterns and relative signal strengths of various polarization combinations has been developed for molecules on the surface of arbitrarily shaped particles.[150] However, for clarity, the most common case of spherical particles will be focused on here. For a particle with spherical symmetry, it is natural to define the tensor elements of its effective susceptibility in terms of components perpendicular and parallel to the particle surface. Different subsets of these tensor elements will be probed, depending on the polarization combination in the experiment. With the polarization states defined as *p* for electric fields within the incidence plane of the visible and IR beams and *s* for electric fields perpendicular to this plane, the four non-zero achiral effective susceptibilities for spherical particles are $\Gamma_{ppp}^{(2)}$, $\Gamma_{ssp}^{(2)}$, $\Gamma_{sps}^{(2)}$ and $\Gamma_{pss}^{(2)}$. They can be expressed as linear combinations of gamma-factors that depend on the beam geometries in the following way,[142]

$$\begin{aligned}\Gamma_{ppp}^{(2)} = {} & \cos\left(\frac{\theta}{2}\right)\cos\left(\frac{\theta}{2} - \alpha\right)\cos(\frac{\theta}{2} - \alpha + \beta)\Gamma_1 + \cos(\theta - \alpha + \beta)\cos\left(\frac{\theta}{2} - \alpha\right)\Gamma_2 \\ & + \cos(\theta - \alpha)\cos\left(\frac{\theta}{2} - \alpha + \beta\right)\Gamma_3 + \cos(\beta)\cos\left(\frac{\theta}{2}\right)\Gamma_4\end{aligned} \tag{1.23}$$

$$\Gamma_{ssp}^{(2)} = \cos\left(\frac{\theta}{2} - \alpha\right)\Gamma_2 \tag{1.24}$$

$$\Gamma_{sps}^{(2)} = \cos\left(\frac{\theta}{2} - \alpha + \beta\right)\Gamma_3 \tag{1.25}$$

$$\Gamma_{pss}^{(2)} = \cos\left(\frac{\theta}{2}\right)\Gamma_4 \tag{1.26}$$

where θ and α are the angles for the detected SFS signal and the incidence IR laser beam relative the phase-matched direction, while β is the angle between the IR and visible laser beams. Various combinations of the effective susceptibility tensor elements referenced to the particle geometry are included in the gamma-factors, which are defined as $\Gamma_1 = \Gamma_{\perp\perp\perp}^{(2)} - \Gamma_{\parallel\parallel\perp}^{(2)} - \Gamma_{\parallel\perp\parallel}^{(2)} - \Gamma_{\perp\parallel\parallel}^{(2)}$, $\Gamma_2 = \Gamma_{\parallel\parallel\perp}^{(2)}$, $\Gamma_3 = \Gamma_{\parallel\perp\parallel}^{(2)}$, and $\Gamma_3 = \Gamma_{\perp\parallel\parallel}^{(2)}$. These gamma-factors can conveniently be connected to the $\chi_{ijk}^{(2)}$ elements for a corresponding flat surface geometry using the following matrix representation:[142]

$$\begin{pmatrix}\Gamma_1\\ \Gamma_2\\ \Gamma_3\\ \Gamma_4\end{pmatrix} = \begin{pmatrix}2F_1 - 5F_2 & 0 & 0 & 0\\ F_2 & 2F_1 & 0 & 0\\ F_2 & 0 & 2F_1 & 0\\ F_2 & 0 & 0 & 2F_1\end{pmatrix}\begin{pmatrix}\chi_1\\ \chi_2\\ \chi_3\\ \chi_4\end{pmatrix} \tag{1.27}$$

where $\chi_1 = \chi_{\perp\perp\perp}^{(2)} - \chi_{\parallel\parallel\perp}^{(2)} - \chi_{\parallel\perp\parallel}^{(2)} - \chi_{\perp\parallel\parallel}^{(2)}$, $\chi_2 = \chi_{\parallel\parallel\perp}^{(2)}$, $\chi_3 = \chi_{\parallel\perp\parallel}^{(2)}$, and $\chi_3 = \chi_{\perp\parallel\parallel}^{(2)}$. The factors inside the square matrix are form factor functions that connect the planar geometry to the spherical geometry via the scattering vector norm, q, and the radius, R, of the particle[142]

$$F_1 = 2\pi i\left(\frac{\sin(qR)}{(qR)^2} - \frac{\cos(qR)}{qR}\right) \tag{1.28}$$

$$F_2 = 4\pi i\left(3\frac{\sin(qR)}{(qR)^4} - 3\frac{\cos(qR)}{(qR)^3} - \frac{\sin(qR)}{(qR)^2}\right) \tag{1.29}$$

$$q = \|\vec{q}\| = 2\left\|\vec{k}_0\right\|\sin\left(\frac{\theta}{2}\right) \tag{1.30}$$

where $\vec{k}_0$ is the wave vector for a signal in the phase matched direction, while θ and $\vec{q}$ are the scattering angle and scattering vector away from this direction.

Eqs. 1.28-1.30 connect the effective susceptibilities probed in SFS experiments with the tensor elements for the corresponding situation on a planar interface. As discussed in the previous section about SFG, the χ_i elements in Eq. 1.27 can ultimately be described as linear combinations of the molecular hyperpolarizabilities, with factors that depend on the average molecular orientation relative the surface normal. For the case where achiral molecules do not exhibit a preferred rotation angle around their axis, while being arranged isotropically around the surface normal of the structure they are adsorbed to, the χ_i factors above depend on the molecular tilt θ as[142]

$$\begin{pmatrix} \chi_1 \\ \chi_2 \\ \chi_3 \\ \chi_4 \end{pmatrix} = \frac{N\langle\cos\theta\rangle}{2} \begin{pmatrix} 5D-3 & 0 & 0 & 0 \\ 1-D & 2 & 0 & 0 \\ 1-D & 0 & 2 & 0 \\ 1-D & 0 & 0 & 2 \end{pmatrix} \begin{pmatrix} \beta_1 \\ \beta_2 \\ \beta_3 \\ \beta_4 \end{pmatrix} \tag{1.31}$$

where N is the molecular number density and D is the ratio $\langle\cos^3\theta\rangle/\langle\cos\theta\rangle$. The β-factors are defined as $\beta_1 = \beta_{ccc}^{(2)} - \beta_2 - \beta_3 - \beta_4$, $\beta_2 = \left(\beta_{aac}^{(2)} + \beta_{bbc}^{(2)}\right)/2$, $\beta_3 = \left(\beta_{aca}^{(2)} + \beta_{bcb}^{(2)}\right)/2$, and $\beta_4 = \left(\beta_{caa}^{(2)} + \beta_{cbb}^{(2)}\right)/2$. From this, it becomes clear that if the relative strengths of the hyperpolarizability tensor elements are known, SFS can be used to probe the average tilt of molecules at the interfaces of spherical structures by measuring the relative strengths of the effective susceptibilities in different polarization combinations.

While the model above is applicable for molecules adsorbed on the surface of spherical particles, it is also possible to use SFS to investigate protein fibers. However, per definition, protein fibers include repeating units that provide long-range ordering of molecular groups, not only at the surface of the fibers but also in the bulk region of them. This means that SFS signals from protein fibers will include contributions from the surface region as well as the interior of the fibers. Complete separation of these is not possible, but it is likely possible to tune the detection scattering angle to emphasize contributions from the surface region. The models for arbitrarily shaped structures are dependent on precise knowledge about the geometry of the scatterers and assume negligible difference in the refractive indices between the scatterer and the surrounding media. This makes theoretical evaluation of angles with enhanced surface-specificity challenging for self-assembled biological macrostructures, in particular if the sample is polydisperse and include a range of protein fiber diameters, persistence lengths, and orientations. However, SFS signals can nevertheless be acquired and qualitative statements about the structures can be made. With further developments, quantitative and detailed conclusions about protein fiber structures and interfaces, as well as their interactions may become possible.

1.2 PROTEIN FIBERS

Protein fibers are ubiquitous in nature. As part of the cytoskeleton, they support the shape and mechanical resistance of cells and play key roles for cell migration and signaling pathways. In the extracellular environment, protein fibers are major components of the matrix that provide structural integrity to tissues. In tissue engineering, the design of scaffolds that mimic these structures is a main goal, as they are crucial for cell survival, proliferation, and differentiation in regenerative medicine. Protein fibers also exist outside living organisms. Examples include hair that include the fibrous protein keratin, and the β-sheet rich protein assemblies of spider silk – both of which have attracted considerable attention in materials science research due to their remarkable mechanical properties, with strengths comparable to steel at a fraction of the density. In addition to functional protein fibers, there are also numerous fibrous structures that are linked to severe diseases. The most striking examples are amyloid fibers that arise from misfolding and aggregation of a wide range of proteins. Assemblies of such fibers are hallmarks of several neurodegenerative conditions, including Alzheimer’s disease and Parkinson’s disease.[151-153]

Due to their hierarchical structure in large supramolecular assemblies of biomacromolecules, detailed studies of protein fiber structures and their interactions are notoriously challenging. However, such information is imperative in order to understand their role in the contexts mentioned above. Exploring new techniques capable of protein fiber characterization in their natural environments is therefore of great importance, as it may provide avenues that, for example, lead to new insights for improved tissue engineering strategies or treatments of amyloid diseases.

1.2.1 *Collagen Fibers*

Collagens are the most abundant proteins in mammals and the main structural component of the extracellular environment and connective tissues. At least 28 different types of collagen exist, numbered in the order of discovery, and they can be divided into several families. The fiber forming family include collagen types I, II, III, V, XI, XXIV, and XXVII.[154] Collagen fibers are hierarchical super-structures (Figure 1.6) in the extracellular matrix (ECM) that provide support for cells, and promote cell proliferation, migration, and cell survival, for example via activation of focal-activated kinase proteins.

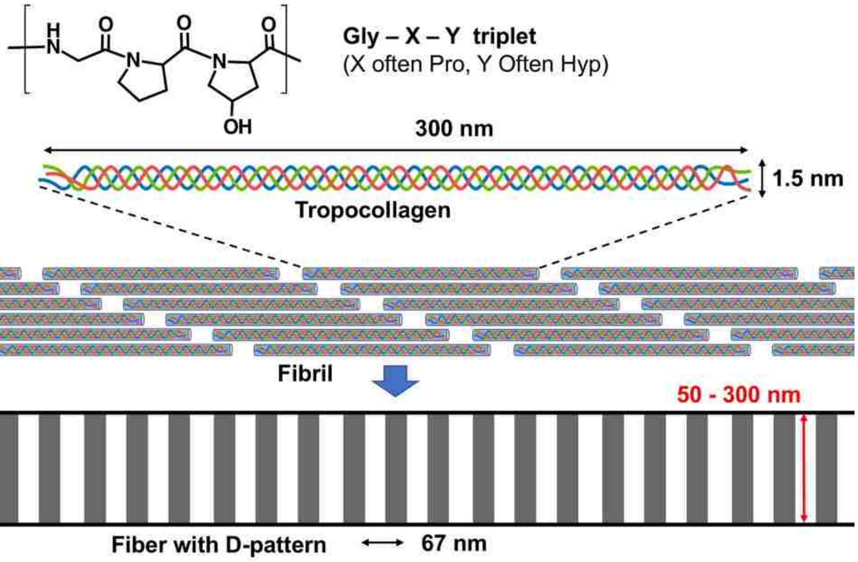

Figure 1.6. Hierarchical structure of collagen fibers. On the primary level, there are Gly-X-Y triplets that form left-handed α-helices, which bundle together to form a right-handed triple-helical structure called tropocollagen. Tropocollagen is the building block for fibrils that make up big fibers that exhibit a characteristic 67 nm D-period.

At the primary level, the collagen structure consists of repeating Gly-X-Y peptide triplets in long α-chains, where X is often a proline, while Y is commonly a hydroxy-proline. As a result, the chains, which typically consist of >1000 peptide units, twist into left-handed helices. Three such helices bundle together to form the right-handed triple-helical building block for collagen fibers called tropocollagen, which is a unit 300 nm long and ~1.5 nm in diameter. Tight packing of the triple-helices is realized by the small glycine residues at the center of the tropocollagen, which can be either homo- or heterotrimers. Collagen types I, II and III represent >80 % of all collagen, of which type I is the most abundant. It exists generally as a heterotrimer, with two α_1(I) chains and one α_2(I) chain, although homotrimers that include only the former have also been identified. All the known collagen types and triple-helical assemblies are listed in Table 1.2.

Table 1.2. Collagen types and compositions. Collagens in the fiber forming family are noted with an ‘f’ superscript (except XXIV and XXVII).

Collagen type	**α-chains**	**Composition**
I^f	α_1(I), α_2(I)	$[\alpha_1(I)_2\ \alpha_2(I)]$ $[\alpha_1(I)_3]$
II^f	α_1(II)	$[\alpha_1(III)_3]$
III^f	α_1(III)	$[\alpha_1(III)_3]$
IV	α_1(IV), α_2(IV), α_3(IV), α_4(IV), α_5(IV), α_6(IV)	$[\alpha_1(IV)_2\ \alpha_2(IV)]$ $[\alpha_3(IV)\ \alpha_4(IV)\ \alpha_5(IV)]$ $[\alpha_5(IV)_2\ \alpha_6(IV)]$
V^f	α_1(V), α_2(V), α_3(V), α_4(V)	$[\alpha_1(V)_2\ \alpha_2(V)]$ $[\alpha_1(V)_3]$ $[\alpha_1(V)_2\ \alpha_4(V)]$
VI	α_1(VI), α_2(VI), α_3(VI), α_4(VI), α_5(VI), α_6(VI)	$[\alpha_1(VI)\ \alpha_2(VI)\ \alpha_3(VI)]$ $[\alpha_1(VI)\ \alpha_2(VI)\ \alpha_x(VI)]$
VII	α_1(VII)	$[\alpha_1(VII)_3]$
VIII	α_1(VIII), α_2(VIII)	$[\alpha_1(VIII)_2\ \alpha_2(VIII)]$ $[\alpha_1(VIII)\ \alpha_2(VIII)_2]$ $[\alpha_1(VII)_3]$
IX	α_1(IX), α_2(IX), α_3(IX)	$[\alpha_1(IX)\ \alpha_2(IX)\ \alpha_3(IX)]$ $[\alpha_1(IX)_3]$
X	α_1(X)	$[\alpha_1(X)_3]$
XI^f	α_1(XI), α_2(XI), α_3(XI)	$[\alpha_1(IX)\ \alpha_2(IX)\ \alpha_3(IX)]$ $[\alpha_1(IX)\ \alpha_1(V)\ \alpha_3(IX)]$
XII to XXVIII	α_1(XII to XXVIII)	All homotrimers

Due to its high abundance and ease of extraction from readily available sources, type I collagen is commonly used in scientific research. The two main extraction methods are pepsin extraction and acid extraction. The former leads to solubilized atelocollagen, while the latter solubilizes collagen but preserves the integrity of the telopeptides. Both varieties lead to well-ordered fibers when self-assembled *in vitro* and their inherent fiber structure seems only moderately influenced by the telopeptides, as the triple-helical part of the tropocollagen is the main determinant for the self-assembly. However, collagen with intact telopeptides self-assembles faster *in vitro* and the resulting fiber network has enhanced mechanical properties, when compared to atelocollagen. It is yet an open question exactly how the telopeptides facilitate the fiber formation, but studies have demonstrated enhanced transient collagen-interactions and it is hypothesized that the C-terminal of the telopeptides interacts with the matrix metalloprotease binding region. *In vivo*, the contribution of telopeptides to enhanced mechanical properties, such as increased tensile strength, is more obvious as they form cross-links that significantly stabilize the organization and yield cooperative strength of collagen fibers connected in networks.[155] There are many parameters in addition to the telopeptides that influence not just the rate of formation, but also the fiber structure. The temperature, collagen concentration, pH, phosphate level, ionic strength, flow of the solution, are some examples.[156-158] Therefore, it is important to strictly adhere to the same protocol in order to reproduce the properties of the fibers. When highly ordered fibers are achieved, the tropocollagens pack together side-by-side, typically yielding a fiber diameter of about 50 – 300 nm and the total fiber length and persistence length can be considerable (many micrometers). When the tropocollagens assemble with a 67 nm displacement relative one another, a characteristic pattern referred to as D-periods is observed in high-resolution imaging. Alterations to this pattern can be used for qualitative assessment of fiber structures. For detailed analysis of the inner structure of collagen fibers in biological samples, techniques based on nonlinear optics have been applied, while X-ray diffraction (XRD) has been used to investigate engineered collagen-like peptides. Information gained from this includes average pitch angles (tilt relative the fiber axis) for the carbonyls in the peptide units and the methylene groups of the side-chains. For collagen I-like heterotrimers, the XRD data gave 46.3° for the peptide and 97.5° ± 43.9° for the methylene pitch angles. From SHG polarization analyses of type I collagen fibers in rat tail tendons, the retrieved pitch angles were 45.8° ± 0.5° and 94.8° ± 1.0°, which is in good agreement with the XRD results.[49] Corresponding analyses were also made for collagen II-like homotrimers (pitch angles of 44.8° and 109.0° from XRD) and type II collagen fibers in rat trachea cartilage (pitch angles of 45.7° ± 1.2° and 97.8° ± 1.8° from SHG). While the quantitative difference for these angles seem small between type I and II collagen fibers, they actually translate into significantly different values for the average SHG tensor element ratios χ_{zzz}/χ_{zxx} (1.51 for type I and 1.26 for type II) and χ_{xxz}/χ_{zxx} (0.62 for type I and 0.39 for type II). Not only does this allow specific detection of collagen fibers of different types in nonlinear microscopy of tissues, but it also confirms the sensitivity of nonlinear optics for studies of the detailed molecular structure of collagen fibers. For this reason, sum-frequency scattering (SFS) has been explored for collagen fiber analysis in this work, and the results are presented in Chapters 3 and 4. The scattering mode provides an additional level of structural sensitivity as distinct regions of the fibers may be probed at specific angles, while the signal enhancement for ordered IR *and* Raman active vibrational gives direct chemical specificity. This is in contrast to the SHG approach, for which the chemical specificity relies on a theoretical model that yields distinct polarization dependencies for the tensor elements that contribute to the signal.

1.2.2 *Amyloid Fibers and Spherulites*

Under mild denaturation, many proteins misfold and aggregate into amyloid structures. In fact, this property has been proposed as a generic feature of polypeptides, provided that the right conditions for the aggregation can be found. The detailed structure of amyloid fibers depends on the source protein and preparation method, but the structures generally include packing of β-strands into sheets that extend long distances along the fiber axis. Normal fiber dimensions are a diameter of 5 to 20 nanometers and persistence lengths up to several micrometers, but it varies considerably. Due to their connection to severe diseases and their material properties, the interest for amyloid structures have been substantial within the biomedical and materials science communities.

Table 1.3. A selection of amyloid related diseases and the associated proteins. Size refers to the number of residues in the protein.

Disease	**Protein**	**Size**
Alzheimer's disease	Amyloid β	40 or 42
Parkinson's disease	α-synuclein	142
Huntington's disease	Huntingtin	3144
Spongiform encephalopathies	Prion protein	253
Senile systemic amyloidosis	Transthyretin	127
Fibrinogen amyloidosis	Fibrinogen α-chains	27 to 81
Lysozyme amyloidosis	Lysozyme mutants	130
Type II diabetes	Amylin (hIAPP)	37
Amyotrophic lateral sclerosis	Superoxide dismutase 1	153
Hemodialysis-related amyloidosis	β_2-microglobulin	99

About 50 diseases are associated with protein misfolding and formation of insoluble aggregates, most notably amyloid fibers.[153] Included in these disorders are type II diabetes, Parkinson's disease and Alzheimer's disease (AD). AD is a neurodegenerative condition responsible for over 70 % of dementia, which afflicts over 46 million people worldwide and the accumulated costs related to healthcare for the patients exceed $800 billion annually. The amyloid hypothesis for AD states that the disease is caused by the accumulation of amyloid β (Aβ) proteins that misfold and aggregate into fibrillar structures, forming amyloid plaques in the brain extracellular matrix (ECM). It is generally believed that the early oligomeric stages of the amyloid fibers are the toxic species, while the mature fibers are more inert. However, it has also been suggested that the build-up of amyloid fibers into senile plaques is not the cause of AD, but instead a correlated process. Regardless, the formation of amyloid plaques is a hallmark of AD that may provide insights into the disease pathology, which could lead to new biomarkers and potentially a cure for the disease. A selection of amyloid related conditions and the associated proteins are listed in Table 1.3.[152, 153] In addition to the pathophysiological relevance of amyloids in severe diseases, much research has been focused at amyloid structures due to their chemical, mechanical, and optical properties.[34, 35, 159-161] As mature fibers are not cytotoxic and they can be made from cheap proteins not related to any known degenerative condition, they have been considered as functional materials in biomedical applications. For example, many amyloid fibers are resistant against proteases and have therefore been suggested as delivery vehicles for ingestible drugs, securing the passage through the stomach to the gut where they may be released.[162] Rigid amyloid fibers also tend to have a Young’s modulus similar to silk and tensile strength comparable to steel, which make them attractive as biological nanowires.[163] This could be useful in e.g. bioelectronic applications, as the nanowires may be coated with conductive polymers and used to interface biological systems with electronic conductors.[164, 165] As amyloid fibers can be readily functionalized by supramolecular coating or embedding of molecules in the structures while preparing them, they have also found use in a range of nonbiological applications. For example, as a dispersing material of phosphorescent molecules in white organic light emitting diodes (OLEDs), which enhances the external quantum efficiency by reducing energy back-transfer to the fluorescent polymer matrix, while also providing a more favorable device morphology.[166, 167] Additional features that make amyloid fibers interesting from a fundamental materials science point of view are intrinsic linear and nonlinear optical properties that emerge in the amyloid state. This include intrinsic fluorescence in the blue/green regime of the visible spectrum, as well as enhanced multiphoton absorption with cross-sections comparable to those of good two-photon dyes.[168] Multiple hypotheses have been proposed for the origin of these phenomena with no consensus yet. Through-space dipolar coupling between excited states of aromatic amino acids densely packed in the fiber structures has been proposed for the multiphoton absorption, as it seems dependent on the presence of tyrosine in the protein. However, the intrinsic fluorescence can appear even without ring-structures in the protein sequence and requires thus alternative explanations. The phenomenon may be multifaceted and hypotheses include proton transfer, electron delocalization mediated through hydrogen bonding, and quantum confinement of the peptides.[159, 161, 169, 170] As some amyloid fibers have been shown to intrinsically conduct electronic currents, mechanisms that allow charge carriers to travel along the fibers are particularly intriguing, such as the electron delocalization hypothesis.

Amyloid-forming proteins do not only assemble into individual fibers, but can also form large structures called amyloid spherulites.[171-178] The size of these spherical objects ranges from about 10 up to several 100s of micrometers, depending on the conditions during the aggregation process. Amyloid spherulites typically include an amorphous core, which can vary in size from being almost non-existent to a considerable fraction of the spherulite volume, from which β-sheet-rich amyloid fibers grow out radially. While the exact mechanism for the formation of these structures has not been described in detail, they are likely formed through specific self-assembly pathways of the source protein, rather than aggregation of mature amyloid fibers. Amyloid spherulites are birefringent, which means that they can be imaged with cross-polarized optical microscopy (Figure 1.7). The alignment of the amyloid fibers radially from the center of the spherulite yields a characteristic Maltese cross pattern when viewed in this way, as fibers orientated parallel or perpendicular to the electric field do not turn the polarization direction of the light. In amyloid diseases, aggregates have been shown to exhibit features characteristic of spherulites.[179, 180] One of the more striking examples is the aforementioned Maltese cross pattern that sometimes appears in cross-polarized microscopy of senile plaques in the brain tissue of AD patients. This is an indication that the amyloid deposits in AD are not random aggregates of preformed fibers, but rather the assembly of proteins through specific pathways that may be related to the ones for amyloid spherulites *in vitro*.

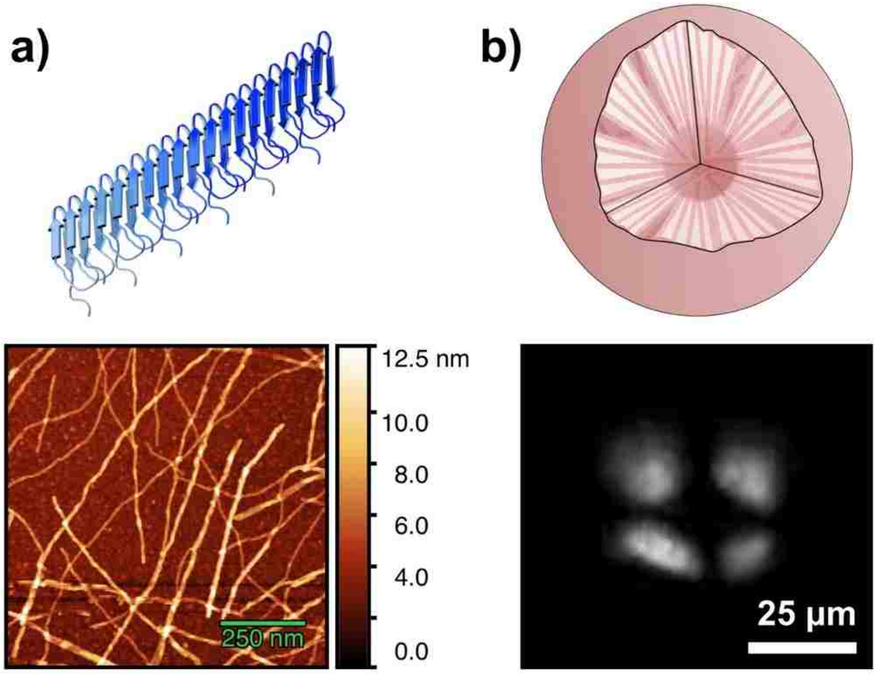

Figure 1.7. Amyloid fibers and spherulites. a) Schematic structure of an amyloid fiber, with β-sheets along the fiber axis. The AFM image shows amyloid fibers from insulin adsorbed onto a Si substrate. b) Schematic structure of amyloid spherulites. A cross-polarization microscope image reveal the typical Maltese cross pattern for an amyloid spherulite formed from insulin.

Studies of amyloid structures with coherent second-order optical techniques (i.e. SHG and SFG) are surprisingly few, given the high inherent ordering of these fibrous structures that may be formed from a variety of proteins with connections to many severe diseases. One contributing reason to this may be the fact that the structures are rich in β-sheets, which have relatively low hyperpolarizabilities for the amide I groups due to their unfavorable symmetry with alternating directions of the carbonyls. Nevertheless, a few studies have been focused at amyloid fibers from β-lactoglobulin (β-LG) and human islet amyloid polypeptides (hIAPP). When amyloid fibers are formed from β-LG at high concentrations (7.5 % w/v) the morphology and persistence length of the fibers are more "worm-like" compared to when they are formed at lower concentrations (3.0 % w/v), which yields longer and more ordered fibers.[105, 106] By adsorbing β-LG fibers formed under the two conditions onto mica and acquiring SFG data in reflection mode from the surface, it was shown that these structural differences are correlated with the secondary structure of the fibers. The long and ordered fibers had almost exclusively β-sheets, while the "worm-like" fibers included more α-helices. The hIAPP fibers, which are related to type II diabetes, have been studied with SFG on the water/air interface in the presence of dipalmitoylphosphoglycerol (DPPG) lipids.[71, 181] After establishing that α-helices lack chiral signals in the amide I region, but appears in the N-H stretching region, it was demonstrated that β-sheet rich hIAPP amyloid fibers grow at the water-lipid interface via a transient α-helical stage with a peak maximum at about 3 h, for the experimental conditions used.[71] Additional SFG studies of amyloid fibers are warranted, to elucidate further details regarding the dependence of secondary structure on the fiber forming conditions and the existence of transient stages during amyloid growth. However, in this work, the intrinsic linear and nonlinear optical properties (fluorescence, TPEF, and SHG) of amyloid structures from insulin and β-LG have been investigated and the results are presented in Chapter 5.

Chapter 2. MATERIALS AND METHODS

In this chapter, broad discussions regarding the materials, principles for sample preparation, and overviews of the main analytical techniques applied for their characterization are provided. More detailed descriptions of the specific experiments are then supplied within each chapter.

2.1 SAMPLE PREPARATION

In this work, type I collagen fibers and amyloid structures from insulin and β-lactoglobulin (β-LG) have been investigated. They have all been prepared by self-assembly *in vitro* and the resulting structures are dependent on the conditions under which they form, which is discussed below.

2.1.1 *Type I Collagen Fiber Assembly*

The specific structure and quality of fibers self-assembled from type I collagen depend heavily on a range of factors, such as the pH, temperature, collagen concentration, ionic strength, phosphate concentration, presence of specific ions, and flow of the solution.[156-158] It is tempting to think that the hydrophobic effect is the main driving force for collagen self-assembly. However, there are studies indicating that water-mediated hydrogen bonding between polar residues is more important.[182] In contrast to when a protein folds into its tertiary structure and thereby hides hydrophobic residues from the surrounding solvent, the assembly of collagen is not a three-dimensional reorganization of residues but rather packing of many tropocollagen triple-helices side by side. Therefore, while hydrophobic residues most likely come into contact when the fibers form, the interior of the fibers is not likely to be much more hydrophobic than the fiber surface, which may explain why driving forces other than the hydrophobic effect may dominate the process. Type I collagen can be kept soluble at low pH and is often stored in 0.01 M HCl or 0.2 M acetic acid solutions. By mixing with a buffer and adjusting the pH closer to the isoelectric point (pI) of the collagen, self-assembly may be initiated. A wide range of values have been claimed for the pI of collagen, from 4.7 up to 9.3. The most commonly quoted values for the pI are close to 8 and it is probably more accurate to consider pH 7.0 to 8.5 an isoelectric zone. Within this region, D-banded fibers may form, although the *specific* structure is likely sensitive to the exact pH value, as well as the other aforementioned factors. It has been shown that fibers with homogeneous morphology require the presence of phosphate, with optimal concentrations exceeding those normally used in PBS 1x. However, too high concentrations can reduce the fiber formation rate, and the optimal phosphate range seems to be about 20 – 30 mM. The collagen concentration also affects the fiber quality and rate of formation. For type I collagen with preserved telopeptides, lower concentrations favor ordered fibers and optimal levels have been suggested to be <0.5 mg/mL. One reason for this could be that high concentrations rapidly lead to fibers with a structure determined by kinetics rather than thermodynamics, while slower assembly from lower concentrations allows reorganization to more energetically favorable structures that are highly ordered. If so, it is likely that the corresponding optimal concentrations for pepsin digested collagen (atelocollagen that lacks the rate-enhancing telopeptides) are somewhat higher, as the formation rate is lower. Naturally, the rate of formation is also heavily dependent on the temperature during the assembly. Below 10 ˚C, the rate is negligible, which is convenient as the solutions can be kept on ice to prevent premature fiber formation during the preparation until optimal conditions for the all parameters have been reached, at which point the temperature can be raised. Highly ordered fibers form at 20 – 30 ˚C, but a higher yield and reproducibility may be reached at temperatures closer to 37 ˚C. One final comment, is that before the temperature is raised to initiate the fiber formation, it is a good idea to centrifuge the collagen mixture, to remove potential aggregates that may have formed during the preparation, which could act as nucleation sites for growth of amorphous collagen structures.

2.1.2 *Amyloid Structures from Insulin and β-lactoglobulin*

While the ability to form amyloid structures has been suggested a generic property of polypeptides, conditions for the formation of both fibers and spherulites have only been identified for a few proteins. Two of them are insulin and β-LG. Insulin is famous for its importance in regulating blood sugar levels by promoting uptake of glucose in liver, fat, and skeletal muscle cells. While no disease has been identified as the cause of insulin amyloidosis, it is a rare complication at the injection site for patients with diabetes, which may interfere with the dose-response and lead to poor glycemic control. β-LG is a whey protein found in the milk of many mammals, however, not humans. It is a lipocalin protein and may function as a modulator for hydrophobic ligand uptake, such as cholesterol or vitamin D_2.

Both insulin and β-LG typically exist as multimers under physiological conditions. By reducing the pH below 3, which is significantly under the pI of the proteins (5.3 for insulin and 5.2 for β-LG),[183-185] the proteins dissociate into monomers and undergo conformational changes that promote the formation of amyloid structures[186] if mild denaturation is induced by heating the solutions to ~70 ˚C for insulin and ~85 ˚C for β-LG. Other conditions that induce mild denaturation may also lead to the formation of amyloid structures, but the ones given above are the most studied and lead to amyloids at high rates and with high reproducibility. Additional parameters that affect the process include protein concentration, ionic strength, and stirring. These factors can be tuned so that either the formation of fibers or spherulites are favored. In general, spherulites may appear if the solution is not stirred. For insulin, a protein concentration of about 5 mg/mL and inclusion of NaCl in the solution (up to 25 mM with an optimal value of 5 mM) appears to promote spherulite formation over free fibers. Optimal conditions have not been identified for β-LG, however, the rate of spherulite growth (i.e. the kinetics of radii increase) is enhanced by higher concentrations (up to at least 30 mg/mL) and the preferred NaCl concentration is about 5 mM. When forming amyloid structures from proteins, there is usually a lag phase of a few hours, followed by a growth phase and finally a plateau. The kinetics depend on the parameters discussed above, but the plateau is usually reached within a few days and the dynamics may be probed with amyloid specific dyes, such as thioflavin T. However, the lag phase can be shortened and almost completely bypassed by seeding the solution with preformed fibers or spherulites.[176] The fact that seeding works also for spherulites indicates that they grow by the addition of monomers, rather than aggregation of mature fibers, which shows that the spherulites are their own class of amyloid structures.

2.2 MAIN TECHNIQUES

In an SFG experiment, the signal can either be considered in the time domain or the frequency domain. In the time domain, the visible field instantaneously probe the free-induction decay stimulated by the IR beam. Mathematically, this is represented by a product of the visible field with a convolution of the IR field and the time-response function of the nonlinear susceptibility, $\chi^{(2)}(t)$. After transformation into the frequency domain, this translates to a product between the IR field and $\chi^{(2)}$ for each frequency, which is then convoluted with the field for the visible laser. In other words, unless the visible field is a δ-function in the frequency domain, the line shapes of the probed peaks will be broadened in an SFG experiment. How much the peaks are broadened depends therefore on the pulse length, line shape, and temporal delay for the visible beam in the time-domain.[69] In general, the longer the visible pulse is and the bigger part of the free-induction decay that it captures without distortion, the higher will the frequency resolution of the spectra be. Sometimes, it may be desirable to capture the actual time-response function, $\chi^{(2)}(t)$, which is done in SFG free-induction decay experiments. However, this requires ultra-short pulses for both the visible (for time-resolution) and IR fields (to avoid $\chi^{(2)}(t)$ distortions in the free-induction decay).

2.2.1 *Vibrational Sum-Frequency Generation with a Nd:YAG picosecond Laser*

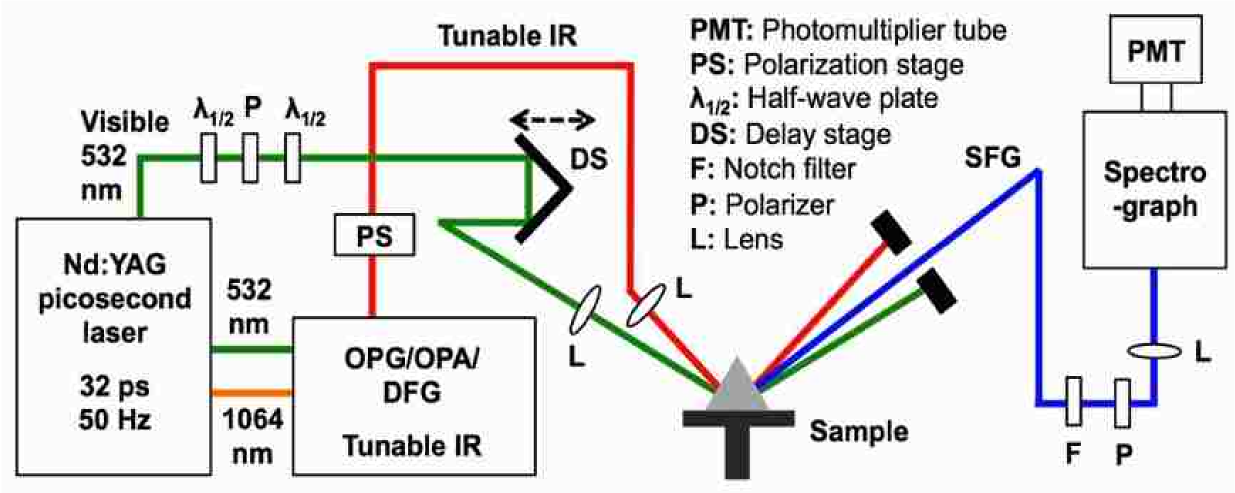

Figure 2.1. Schematic overview of the picosecond SFG system for experiments in reflection mode. The typical pulse length of the visible is 30-32 ps, which allow high resolution SFG, limited by the frequency bandwidth of the IR beam, and the spectrograph.

In this work, a picosecond Nd:YAG laser system was available for SFG experiments in sequential scanning mode, and a schematic of the setup is provided in Figure 2.1. It was primarily used for reflection experiments, for which a pre-designed sample stage was available. The pulse length of the visible beam (532 nm, frequency doubled from the 1064 nm fundamental wavelength of the Nd:YAG) was about 32 ps. This pulse length translates into a FWHM of about 0.5 cm^{-1}, assuming a Gaussian beam profile. This means that broadening of peaks in the spectra will be negligible, and the resolution is limited by the production of narrow-band IR pulses and the spectrograph before the detector (about 4 to 6 cm^{-1}). The IR beam was generated by an OPG/OPA/DFG unit, pumped by a 1064 nm beam and a frequency doubled beam at 532 nm from the Nd:YAG laser. The temporal overlap was adjusted by a manual delay stage for the visible beam, for which the power and polarization state was controlled with two half-wave plates on either side of a Glan-

Laser polarizer. The polarization of the IR beam was controlled by a polarization stage, and the SFG signal was filtered with a Glan-Laser polarizer as well as notch filters. Further filtering and spectral narrowing were provided by a spectrograph, before the signals reached the photomultiplier tube detector. In most experiments, the solid/liquid interface of a CaF_2 prism (sometimes modified with a thin film) was probed and the incidence beams of the IR and visible were typically adjusted to just under the critical angle for total internal reflection. While the signal intensity can be probed in real time for a specific wavenumber with this instrument, capturing of full spectra is relatively slow due to the 50 Hz repetition rate and sequential scanning mode.

2.2.2 *Vibrational Sum-Frequency Scattering with a $Ti:Al_2O_3$ femtosecond Laser*

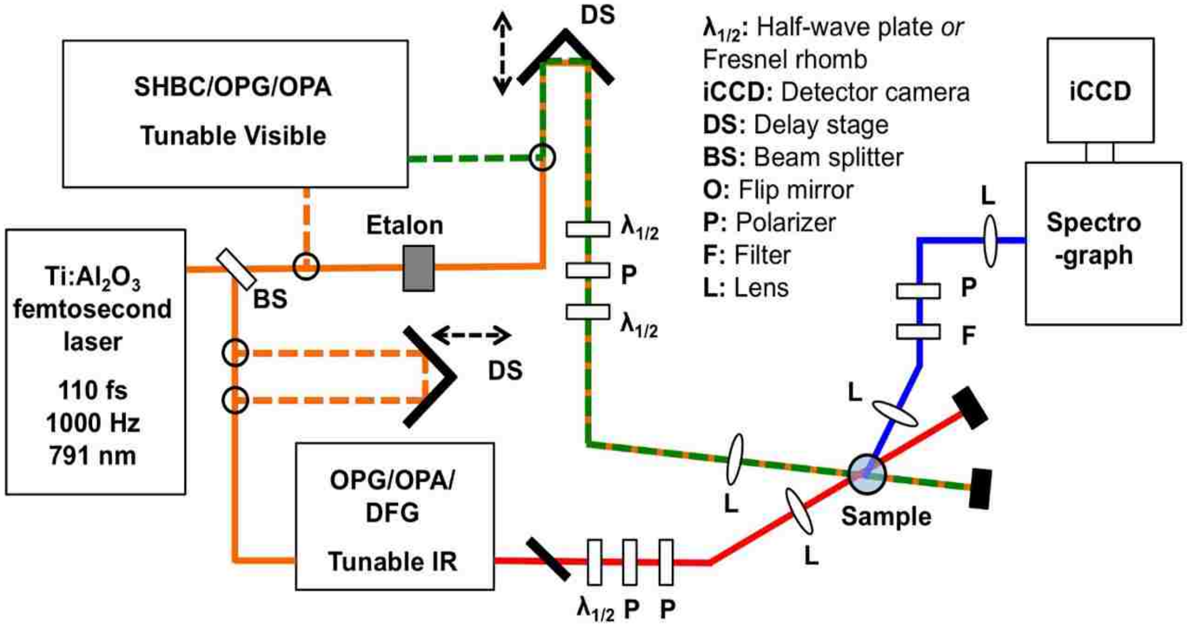

Figure 2.2. Schematic overview of the femtosecond SFS system for experiments in scattering mode. The typical pulse length of the visible is ~2 ps, which broadens the signal and limits the resolution. In the setup, the picosecond visible can either be achieved by etalon-filtering or by pumping an SHBC coupled with an OPG/OPA for production of a tunable visible beam. The latter approach requires a delay of the pump for the IR generation.

For SFS experiments, a femtosecond Ti:Al_2O_3 laser system was used and a schematic is provided in Figure 2.2. The short pulse length requires inclusion of a range of frequencies in order to not break the transform limit and violate the Heisenberg uncertainty principle. As a consequence, the FWHM of the beam is approximately 140 cm^{-1}, which means that each pulse of the IR beam will include a range of wavenumbers. This allows capturing of entire spectral regions in real-time, if the detection scheme includes a spectrograph and an appropriate detector. In our setup, we used an intensified charge coupled device (iCCD), which was typically operated at gain 90 and a gate width of 40 ns or less. In order to minimize peak broadening, the visible/nIR beam was filtered through an etalon, which produces a visible profile with a maximum followed by an exponential decay in the time-domain. The approximate pulse length was about 2 ps, which gave a FWHM for the visible/nIR of about 15 cm^{-1}. Just as for the picosecond system, the power and polarization of the visible/nIR was controlled with half-wave plates on either side of a Glan-Laser polarizer. The power and polarization of the broadband IR was controlled with a half-wave plate (optimized for the amide I region) and two wire-grid polarizers, while the signal was filtered with premium edge-pass filters and a Glan-Laser polarizer. Instead of filtering the visible/nIR with the etalon, a narrow-band visible pulse could also be achieved via a second-harmonic bandwidth converter (SHBC, Light Conversion) that subsequently pumps an OPG/OPA (TOPAS-400-WL, Light Conversion). The resulting Gaussian-like beam is tunable in the region 480 – 2400 nm, with a pulse length 1 – 4 ps and typical FWHM of about 15 cm^{-1}. Experiments with this beam requires a delay of the pump for the generation of the broadband IR, however, no examples where this was used are included in this dissertation, in part because it was observed that the stability of signals from collagen fibers was lower with shorter wavelength, probably due to higher absorption. However, further efforts may be warranted, since the SFS signal is highly dependent on the visible wavelength (at least by $\sim 1/\lambda^4$ due to the Raman scattering cross-section), which could allow lower powers for the visible. Another consideration for the visible produced via the SHBC and the etalon-shaped visible/nIR is the meaning of optimal temporal delay. In general, slightly higher signals are produced when the pulses arrive shortly after the IR beam, but the line shape and broadening of peaks are also affected by this. If possible, it is optimal to gather many spectra at various (equally spaced) temporal delays. If the sample and IR beam remain similar throughout the acquisitions, then each position for the visible beam will interrogate the same free-induction decay in the time-domain. Provided that the visible profiles for the various positions add up to a homogeneous and long net pulse in the time-domain, the signal in the frequency domain should not suffer significant broadening and potential problems with residual chirps of the IR and/or the visible/nIR should also be mitigated.

Finally, the sample cell and collection of the SFS signal will be addressed. Two sample cells have been used in this work: flat windows (CaF_2 on incidence side and SiO_2 on the signal side) with a 200 μm spacer, and hemicylindrical CaF_2 prisms with an 800 μm rubber gasket making space for the sample. When working with a gel-like collagen fiber network, the flat window works for acquisition at specific scattering angles, but it does not allow capturing of complete scattering patterns, nor comparison of various polarization combinations. Two reasons for this is that the flat windows refract the mixing beams and the short spacer forces the fiber network to be compressed in the sample, which can induce long-range ordering of the fibers. Both these effects can distort the scattering patterns and the signal strengths of various polarization combinations. However, the longer spacer between the hemicylindrical prisms, that also do not have preferred escape directions for the produced signals, circumvent these problems. The detection of scattering patterns can be achieved by rotating a collecting lens around the focus point in the sample, where the beams are mixing (Figure 2.3). Lenses with a short focal length are better at collimating the signal, which can subsequently be directed more easily to the detector. Reducing the spread of angles probed can be achieved with apertures directly after the collecting lens and the signal strength should be approximately quadratically dependent on the radius of the apertures. Collagen fibers exhibit strong SFS responses, which allow acquisition of signals with a narrow angle spread (about ±2.5° or less). As it takes long times to acquire complete scattering patterns for any sample, angle-multiplexing the signal in setups that utilize both the width and height of the iCCD detector chip would be desirable. However, in such efforts, it would be very important to calibrate the angular patterns against the sequential acquisition approach, which should be considered the "gold standard". Optimization of such detection schemes would be labor-intensive and has not been explored in this work, but represents a potential outlook for future work within this area.

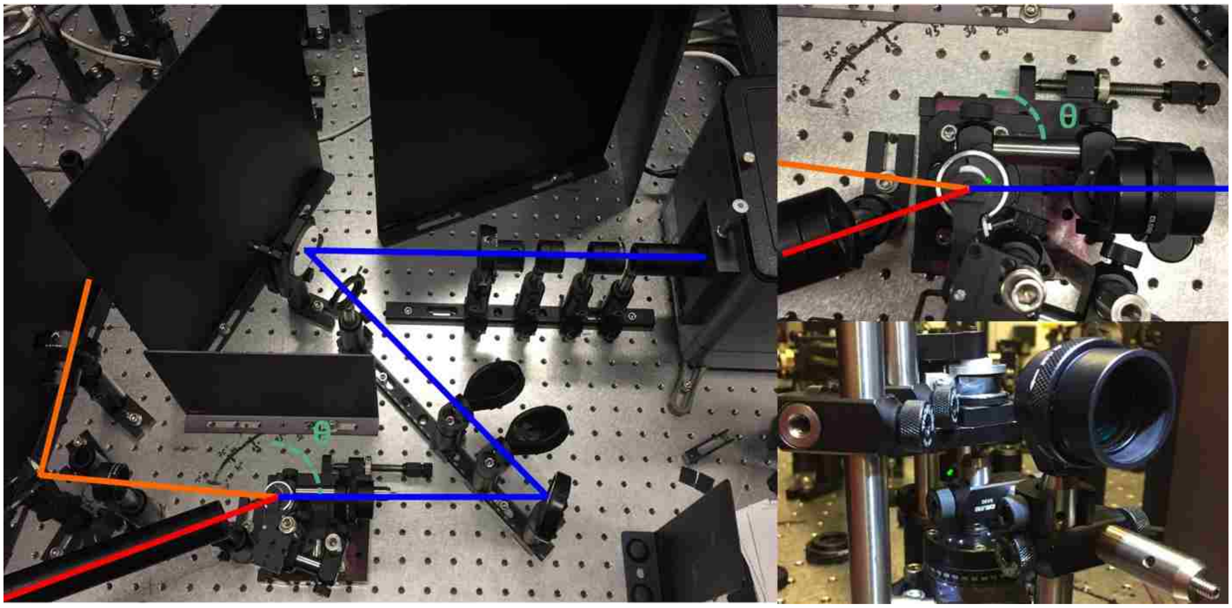

Figure 2.3. The SFS sample stage. The IR (red) and visible/nIR (orange) are overlapped on the sample in between two hemicylindrical lenses. The collection angle is defined by a lens mounted to an arm, which is connected to a post secured with a goniometer centered beneath the sample holder. An aperture mounted on the lens holder limits the spread of angles collected.

2.2.3 *Two-Photon Excitation Fluorescence and Second-Harmonic Generation with a Nonlinear Optical Microscope*

In this work, TPEF and SHG imaging were performed simultaneously with a two-photon microscope (Olympus, FV1000 MPE BX61) pumped with a tunable nIR laser (Spectra-Physics Mai Tai HP) with 80 MHz repetition rate and 100 fs pulse width. The broad emission profile of the Ti:Al_2O_3 crystal in the laser allows tuning of the lasing wavelength between 690 nm to 1040 nm, with maximum power close to 800 nm. The instrument was equipped with filter cubes that split the signal into two detection channels, in our case 420 - 460 nm and 495 - 540 nm. This allowed SHG to be detected in the lower channel with an excitation wavelength, λ_{exc}, 840 - 920 nm. For samples with significant TPEF, λ_{exc} was 910 nm, to minimize TPEF in the SHG channel. However, for samples with low TPEF, λ_{exc} was 860 nm, as it gave stronger signals. The PMT detectors captured the signals in the epi-direction, which means that the SHG signal had to be back-scattered. A 25X/1.05 XL Plan water immersion objective was used and the images were typically scanned at 100 µs/pixel, with pixel sizes <200 nm, so that maximum resolution for the system always was achieved. In experiments, the risk for photodegradation always need to be considered. However, since SHG is a parametric process and the samples in this work exhibited low absorption at the wavelengths used, the excitation powers at the sample could be increased significantly.

Chapter 3. VIBRATIONAL SUM-FREQUENCY SCATTERING FOR DETAILED STUDIES OF COLLAGEN FIBERS IN AQUEOUS ENVIRONMENTS

This chapter is reprinted with permission from a previously published communication (P.K. Johansson and P. Koelsch, *J. Am. Chem. Soc.*, Vol 136, Issue 39, pp 13598-13601, **2014**, DOI: 10.1021/ja508190d). Copyright (2014) American Chemical Society.

3.1 SUMMARY

Protein fibers play a crucial role in many disease related phenomena and biological systems. Structural analysis of fibrous proteins often requires labeling approaches or disruptive sample preparation while lacking chemical specificity. Here we demonstrate that the technique of vibrational sum-frequency scattering (SFS) provides a label-free pathway for chemical and structural analysis of protein fibers in solution. By examining collagen, the most abundant protein in mammals, we show that the SFS signal of fibers can be detected in the NH, CH stretching and bending, and amide I regions. SFS spectra were found to depend on the scattering angle, implying the possibility to selectively probe various features of the fibers. Fitting of the data and maximum entropy method analysis revealed a different phase for side-chains and carbonyl contributions, helping identifying these otherwise overlapping spectral peaks and providing the possibility to perform orientational analysis. Our findings suggest that SFS opens up for greater understanding of protein fibers in solution, which is important for e.g. designing scaffolds in tissue engineering or developing cures for diseases associated with protein fibers.

3.2 RESULTS AND DISCUSSION

3.2.1 *Detection of Collagen Fibers with Second-Harmonic Generation Imaging and Vibrational Sum-Frequency Scattering Spectroscopy*

Protein fibers are a common motif in nature, often essential for the structural integrity of living entities. Collagen fibers, for example, are a major component in the extracellular matrix of connective tissue, while actin filaments are an important part of the intracellular cytoskeleton. Amyloid fibers are associated with several severe diseases, such as Alzheimer's disease[6] and diabetes mellitus;[187] hence, it is of great importance to perform detailed analysis of protein fibers, especially in aqueous environments and with chemical and structural specificity. Electron microcopy[157, 188] and atomic force microscopy[189, 190] have been used for studies of collagen fiber morphology. X-ray crystallography,[191, 192] and nuclear magnetic resonance (NMR)[193] have been used for chemical and structural investigations of collagen-like fibers; however, these techniques typically demand extensive sample preparation and high sample purity, while the analysis can get complicated and requires additional computational efforts.

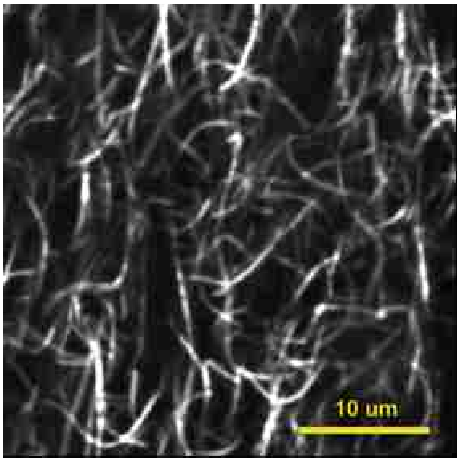

Figure 3.1. SHG image of collagen fibers recorded in back-scattering mode using a confocal upright microscope with excitation wavelength 860 nm. The fibers exhibited intrinsic ordering resulting in high contrast images and were evenly distributed throughout the sample.

Optical imaging techniques such as those based on second harmonic generation (SHG, Figure 3.1), are useful tools to visualize fibers in various environments,[42] however they also lack chemical specificity. Optical spectroscopic techniques like FTIR and Raman do have chemical specificity, but cannot differentiate between chemical species in the surrounding media and those within or on the fibers, so only purified samples can be analyzed. Vibrational sum-frequency-generation (SFG), in reflection or transmission geometries, has previously been used on collagen fibers,[194, 195] but requires the fibrils to be attached to a substrate in an aligned fashion to produce a signal. To overcome all these constraints, we are suggesting using sum-frequency scattering (SFS) for studying protein fibers in solution. This technique is based on the same principles as SFG, but the scattering process allows studies of ordered structures in solution. SFS was first demonstrated by Roke et al.[30] and has since been used for e.g. surface molecular orientation analyses on spherical particles[28, 142] or spectroscopic detection of liposomes.[138, 140] In our study, we used SFS to study collagen type I (PureCol™, Advanced Biomatrix Inc.) fibers. The collagen self-assembled in phosphate buffered saline (150 mM NaCl, 10 mM phosphate) at pH 7.5 into gel-like fibrillar networks (Figure 3.1). The sample preparation procedure has been described elsewhere.[158] After fibrillation, the buffer was exchanged with D_2O to avoid extensive IR absorption from H_2O in the SFS experiments. A fs-pulsed laser system (Quantronix, Integra HE with ~110 fs pulses and Palitra-FS) was used with less than 10 µJ per pulse at the sample stage for the IR and (etalon-shaped) visible beams. The incidence angle between the IR and visible beams was 25°. The IR beam was focused with a lens of 50 mm focal length on the sample to a 50 – 100 µm beam diameter depending on the wavelength. The visible beam was focused about 1 cm beyond the sample cell with a lens of 150 mm focal length, giving a beam diameter of about 500 µm at the sample. The sample cell consisted of a quartz plate (Hellma, 106 QS with a 200 µm spacer) and a CaF_2 detachable window (CeNing Optics Co.) that faced the incoming IR and visible beams (see experimental set-up in Figure 3.2). The SFS signal was collected with a lens of 25 mm focal length and detected with a spectrograph and intensified charge coupled device camera (iCCD, Princeton Instruments, SpectraPro 2300i and Pi-Max 4). Each spectrum was a sum of accumulations with a 50 cm^{-1} IR step size, where each accumulation was normalized to the respective IR intensity, accumulation time and IR profile. The latter was recovered from the third-harmonic signal (difference frequency generation between two visible and one IR photon) from the CaF_2 window. No further data treatment was performed. The scattering angle is defined as the angle between the wave vector in forward direction, $\overrightarrow{k_0}$, and the SFS wave vector $\overrightarrow{k_{0'}}$, which is determined by the scattering vector $\vec{q}$ (Figure 3.2).

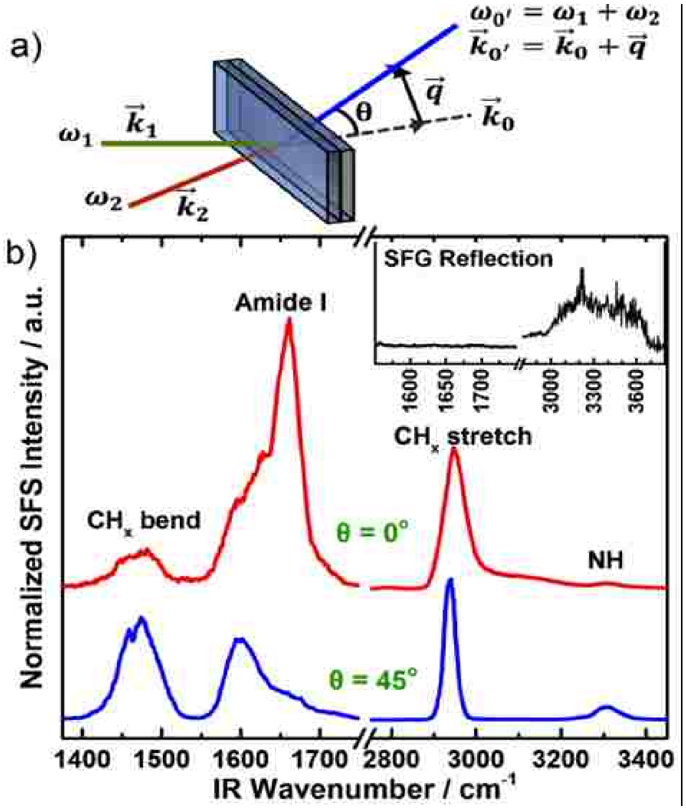

Figure 3.2. Setup and first collagen SFS spectra. a) The experimental set-up. b) Wide SFS_{ssp} spectra of collagen type I fibers in D_2O collected at 0° (top/red) and 45° (bottom/blue) respectively. Inset is an SFG spectra in reflection mode of a similar sample. sample.

We recorded SFS spectra for collagen fibers by placing the collecting lens at scattering angles θ = 0° and θ = 45°. The polarization combination in the experiment was *ssp* (SFS *s*-polarized, Vis *s*-polarized and IR *p*-polarized) where *p* denotes polarization in the incidence plane for the IR and Vis beams, while *s* denotes polarization perpendicular to this plane. The spectra can be divided into four main regions: 1400 - 1600 cm^{-1}, with mainly C-H_x bends from side-chains; 1600 - 1700 cm-1, with the amide vibrations revealing the protein secondary structure; 2800 - 3000 cm^{-1} with C-H_x stretches; and 3200 - 3400 cm^{-1}, with N-H stretches. The spectra at the various scattering angles exhibit some major differences (Figure 3.2). The amide signal at about 1650 cm^{-1} (typical for α-helices) is much stronger at 0°, while the N-H features at about 3300 cm^{-1} are more clear at 45°. Also, the side-chain features at 1400 - 1600 cm^{-1} are more pronounced and the C-H_x stretch signals at 2800 - 3000 cm^{-1} are narrower at 45°. Previous discussions for non-linear scattering from spherical particles revealed that SFS signals at θ = 0° are related to bulk contributions, while signals at higher scattering angles originate from the surface of the particles.[196] A similar mathematical framework for fibers will help us identifying relations between scattering angles and regions probed within fibers in future studies. Another issue to consider is that chiral features may have a scattering maximum in the forward direction, while achiral ones might be emphasized at a certain scattering angle.[144] Control SFG spectra were measured using a CaF_2 prism solid/liquid interface with a ps-pulsed laser system (EKSPLA, Nd:YAG and OPA/OPG/DFG) and incident angles of 60° and 62° relative to the surface normal for the IR and visible beams. The *ppp* polarization combination was used to provide the strongest possible signal in reflection. The spectra did not show any features from collagen, only O-H contributions from water at 3000 - 3700 cm^{-1}. The CaF_2 surface is probably unable to induce ordering to the collagen fibers. This confirms that the spectra are SFS signals and not SFG from the sample cell interface.

3.2.2 *Analysis of Sum-Frequency Scattering Spectra*

The SFS theory has been sorted out for spherical particles and to some extent for other shapes.[144-146, 150] As has previously been done for SFS spectra from spherical particles,[30, 140] we use familiar expressions for SFG[68] to qualitatively analyze the data from the collagen fibers. The SFS signal intensity is then described by

$$I_{SFS} = \left|\Gamma^{(2)} \cdot E_{\omega_{Vis}} \cdot E_{\omega_{IR}}\right|^2 \tag{3.1}$$

where $E_{\omega_{Vis}}$ and $E_{\omega_{IR}}$ are the electric fields of the Vis and IR beams, respectively, and $\Gamma^{(2)}$ is the effective susceptibility for the material under study. $\Gamma^{(2)}$ is a material property that can be divided into a potential non-resonant part and a sum of resonant parts:

$$\Gamma^{(2)} = \Gamma_{NR}^{(2)} + \sum_k \frac{A_k}{\omega_{IR} - \omega_k - i\Upsilon_k} \tag{3.2}$$

with ω_{IR} and ω_k being the wavenumbers of the IR and the kth vibrational mode respectively. Υ_k is a damping factor and A_k is the amplitude for the kth IR and Raman active vibration. The primary structure of fibrillar collagen is Gly-X-Y, where X often is a proline (Pro) and Y is commonly a hydroxyproline (Hyp). The high abundance of Pro and Hyp in the structure makes the peptide chains fold into left-handed α-helices. Three such helices twine together to form a 300 nm long right-handed triple-helix called tropocollagen, which is the building block for larger fibers.[197, 198] The tight packing at the center of the three helices is realized by the smallest amino acid glycine (Gly) in every third residue in the primary structure. IR spectroscopy studies of synthesized collagen-related peptides (poly-glycine, poly-proline and poly-tripeptides),[199] and combined FT-IR and molecular dynamic simulations[200] have shown that the high abundance of Gly, Pro and Hyp in collagen makes it possible to divide the amide I region into three contributions. This has been used in previous SFG-studies and we utilize this scenario in our analysis of the spectra at 1400-1775 cm^{-1}, which were fitted with Eq. 3.2. We split up the amide I region into three different peaks at 1623 cm^{-1}, 1654 cm^{-1} and 1667 cm^{-1}, assigned to Pro, Gly, and Hyp, respectively. The side-chain peaks were found at 1454 - 1490 cm^{-1} and 1595 cm^{-1}. Figure 3.3 shows the fits and peak amplitudes in the amide I region for the two spectra. Gly has the strongest contribution to the amide I signal for both spectra, which is reasonable as it is the main residue in collagen and it agrees with earlier IR spectroscopy studies.[199, 200] The overall peak amplitudes for the amide I vibrations are lower at 45°, with Pro constituting the major difference. The less significant signal decrease for Gly and Hyp may be related to the fact that Gly is buried inside the triple-helical tropocollagen and Hyp can H-bond with the surrounding environment with its extra hydroxyl group, making these residues potentially more stable in their conformation throughout the collagen fiber structure.

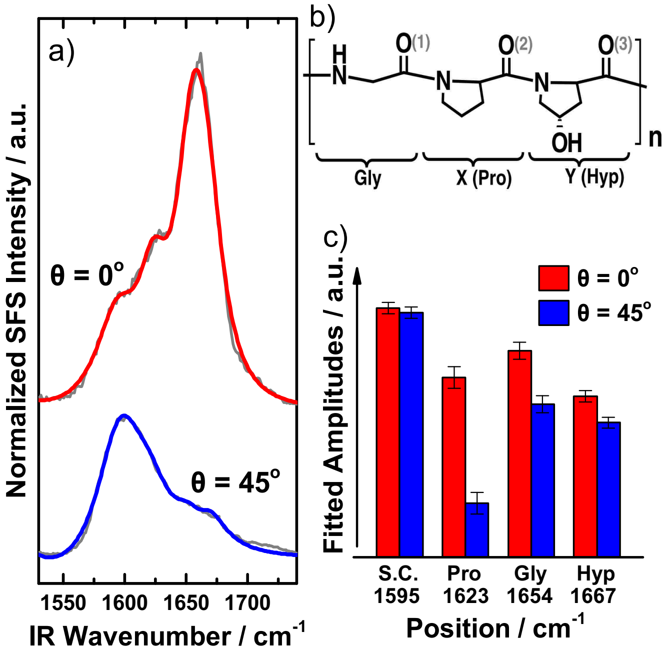

Figure 3.3. Fits of SFS amide I spectra. a) Fits from equation 3.2 of the spectra at 0° (top/red) and 45° (bottom/blue). The grey lines are the raw spectra. b) A simplified overview of the Gly-X-Y primary structure of collagen type I, where X is often a Pro and Y is often a Hyp. c) Bar plot of the positions, amplitudes and assignments for the peaks in the amide I region. Gly, the main residue in collagen, is the strongest contributor.

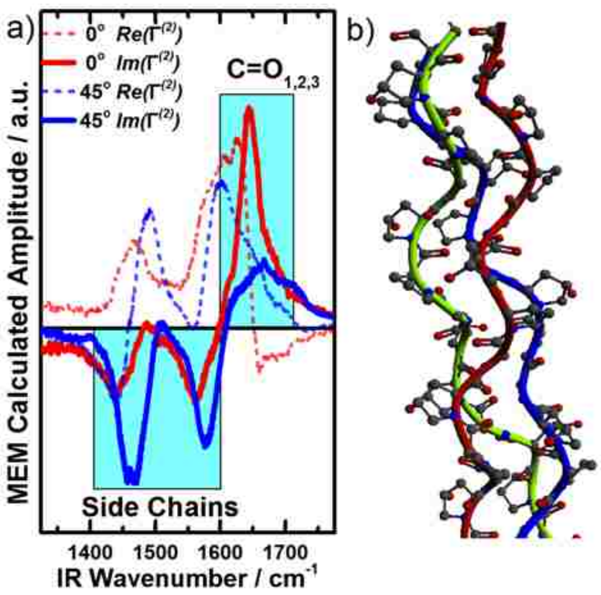

Figure 3.4. MEM analyses of the spectra at 0° and 45° (a) showing that the imaginary parts for the side-chains and the carbonyls differ in sign. Collagen triple-helix structure (b), extracted from the RCSB Protein Data Bank, based on X-ray crystallography studies from Berman et al.[192]

We further analyzed the data using the maximum entropy method (MEM), which allows to derive real and imaginary parts of $\Gamma^{(2)}$ from an intensity spectrum.[201] The MEM analysis is based on performing a Fourier transform of the spectra to the time domain, which gives the autocorrelation function, $R(t)$. The limited spectral resolution in the frequency spectra gives an $R(t)$ only up to a certain time. By expanding $R(t)$ beyond this time, while keeping the resonances exponentially decaying and not adding new information to the original spectra (and thus keeping the spectral entropy at maximum), it becomes possible to calculate a complex $\Gamma^{(2)}$ for the spectra. The only parameter left is an error phase, which is typically adjusted to accommodate reasonable spectral features. While there may be some flexibility in this procedure, it is important that the error phase itself does not alter the phase relation between individual spectral contributions. Therefore, MEM derived imaginary parts, even without error phase adjustments, allow to identify phase relations between peaks. For our data, the MEM algorithm provides a complex solution for $\Gamma^{(2)}$ with opposing signs in the imaginary part for the side-chain peaks and the amide I peaks respectively

(Figure 3.4). In fact, we also realized this phase relation while fitting the spectra, as we could only retrieve reasonable fits with opposing phases for the two spectral regions. As orientation and phases are closely related to each other, we can take advantage of such an analysis in order to (i) differentiate overlapping spectral contributions, and (ii) provide orientational relationships between different chemical groups identified in the SFS spectra.

Previous X-ray crystallography[191, 192] and NMR[193] studies are suggesting that the carbonyls are oriented away from the fiber axis (Figure 3.4), stabilizing the triple helix by forming hydrogen bridge bonds to neighboring strands. In such a scenario, the directions of the carbonyl and the side chains are not opposite, but instead rather similar. If the sign of the hyperpolarizability were equal for both vibrational features, it would lead to a similar phase for the groups. Since our results suggest a different sign of the phase for both contributions, an opposing sign in the hyperpolarizability for carbonyls and side chains seems likely. When such relations between various vibrations are theoretically available, SFS will become a powerful tool for evaluating relative orientations of molecular species in protein fibers.

3.3 CONCLUSIONS

To summarize, we have for the first time recorded SFS spectra of protein fibers. In the case of collagen, there are major distinctions between spectra collected at 0° and 45° scattering angles. Fitting of the spectra shows that it is possible to split up the amide I region into contributions from Gly, Pro and Hyp, respectively, while a MEM analysis revealed that side-chains and the carbonyls have opposing phases. Hypotheses explaining these qualitative results were provided. We believe that SFS studies of protein fibers will become a valuable asset for applications such as tissue engineering and amyloid disease prevention.

Chapter 4. VIBRATIONAL SUM-FREQUENCY SCATTERING AS A SENSITIVE APPROACH TO DETECT STRUCTURAL CHANGES IN COLLAGEN FIBERS TREATED WITH SURFACTANTS

A version of this chapter is being prepared for submission to a journal for biophysics or physical chemistry and may appear as a formal publication of scientific research.

4.1 SUMMARY

Optimizing protocols so that the structure of the collagen fibers in the extracellular matrix remains intact during the decellularization process requires techniques with high structural sensitivity, especially for the surface region of the collagen fibers. Here, we demonstrate that vibrational sum-frequency scattering (SFS) spectroscopy in the protein-specific amide I region provides vibrational spectra and scattering patterns characteristic of protein fiber networks self-assembled *in vitro* from collagen type I, which are kept in aqueous environments during the analysis. At scattering angles away from the phase-matched direction, the relative strengths of the various polarization combinations are highly reproducible, and changes in their ratios can be followed in real-time during exposure to sodium dodecyl sulfate surfactant solutions. For the fibers in this work, we observed a scattering angle of about 22° provides surface specificity, as it allowed monitoring of early structural changes to the fibers during the surfactant exposure. With further development, we hypothesize that the information from SFS characterization of collagen fibers may complement information from other techniques with sensitivity to overall structure, such as second-harmonic generation imaging and infrared spectroscopy, and provide a more complete understanding of the fiber molecular structure during exposure to various environments and conditions.

4.2 INTRODUCTION

One important goal in tissue engineering is to supply organs to patients without the risk of rejection by immune response, which remains a major issue for transplanted donor organs. For example, about 30 - 40 % of heart recipients experience acute rejection within the first year[202] after transplantation, which directly accounts for about 10 % of patient deaths.[203] Triggering of allograft pathologies and an increased risk of infection due to immunosuppressive therapies are other factors associated with acute rejection, contributing to additional fatalities. Decellularization of native tissue yields natural scaffolds that may be combined with patient-specific cells, which is one strategy for successful regeneration of organs that do not trigger the foreign-body reaction. Heart,[204] liver,[205] kidney,[206] lung,[207, 208] and pancreas[209] are examples of organs that have been created using biologic scaffolds obtained through this approach and short-term *in vivo* functions have been demonstrated. With an increasing shortage of donor organs, improving the success of transplanted organs by reducing the risk of acute rejection through tissue engineering is highly desirable, especially if it would allow the use of organs from animal sources.

Effective decellularization is characterized by lysis of cells and removal of all cellular materials, while the collagenous extracellular matrix (ECM) remains intact. However, optimizing the protocols for this remains a challenge and the unique composition and molecular organization of each tissue require specific combinations of the tunable parameters, such as pH, ionic strength, temperature, time, flow, and concentrations of specific decellularization agents.[210] Protocols often include detergents for lysing cells and washing away cellular materials and two of the most common examples are the ionic sodium dodecyl sulfate (SDS) and the non-ionic Triton X-100. While SDS is more effective at removing the cells, Triton X-100 is better at preserving the ECM components.[211] Systematic investigations of the impact of decellularization agents on the ECM structures are challenging, in particular for the collagen fibers that provide structural support in many tissues. Scanning and transmission electron microscopies (SEM and TEM) are commonly used to evaluate the architecture of ECM collagen fibers.[212] However, these techniques require staining of the fibers and extensive sample preparations for analysis in the vacuum chamber. Furthermore, information on the molecular structure is typically not available and quantification of the level of fiber destruction is challenging, which makes correlations with scaffold performance difficult. Infrared (IR) spectroscopy and second-harmonic generation (SHG) microscopy have been used for characterization of collagen fiber molecular structures.[42, 43, 213, 214] However, signal alterations associated with subtle changes to the structure or surface chemistry of the fibers upon surfactant treatment may be too small for reliable detection, but the impact on the scaffold's ability to support cell growth may nevertheless be substantial. Much of the progress in the field has therefore relied on trial and error, leaving gaps in the molecular understanding for why certain decellularization protocols are more successful than others. Recently, a collagen hybridizing peptide (CHP) was designed that specifically binds individual collagen chains.[215-217] By fluorescent labeling of the CHP with carboxyfluorescein, low levels of molecular denaturation of collagen can be detected and visualized in decellularized tissues, which is useful for developing improved protocols. However, it is not possible to follow the collagen denaturing in real-time, as the CHP self-assembles, which also puts constraints on the sample preparation. Additional techniques capable to detect changes to the molecular structure of collagen fibers in real time are thus desired.

With this goal in mind, vibrational sum-frequency generation (SFG) spectroscopy provides a promising avenue, as it combines the specificity for structural symmetries of SHG with the molecular specificity of IR *and* Raman spectroscopy. The sample property probed by SFG is the second-order susceptibility factor, $\chi^{(2)}$, which is a tensor comprised of 27 elements, one for each unique combination of the spatial directions for the three mixing electromagnetic fields. The relative magnitude of these tensor elements depends on the hyperpolarizability, β, of the molecular species contributing to the signal and their organization in the sample relative the sample symmetry axis. Conveniently, unique subsets of the tensor elements can be probed by controlling the polarizations of the mixing beams. For example, $\chi^{(2)}_{ssp}$ (s-polarized SFG and visible light, p-polarized IR) specifically probes $\chi^{(2)}_{yyx}$ and $\chi^{(2)}_{yyz}$, if the z and x directions define the incidence plane. By comparing the signal strengths for various polarization combinations, the relative orientation of the identified species may be deduced.[81, 85-89, 97] This exercise is often facilitated by the fact that several tensor elements must be zero for certain sample symmetries. For example, all tensor elements with an odd combined number of x and y indices vanishes for samples with C_∞ symmetry. For such cases, specific detection of chiral molecules or superstructures is also possible, as the *spp*, *psp*, and *pps* polarization combinations only probe tensor elements that include all three spatial directions (i.e. x, y *and* z). This is useful for characterization of protein structures, since it has been shown that right-handed α-helices often do not appear in chiral SFG spectra for the amide I region, while β-sheets do appear in chiral amide I spectra. This has, for example, been utilized to probe transient stages during amyloid fiber formation.[71, 120]

Collagen fibers have a C_∞ symmetry axis along the fiber direction. This means that only a subset of the effective hyperpolarizability, β_{eff}, tensor elements can be nonzero. The origin and magnitude of, β_{eff}, for various types and sources of collagen has been the focus of several studies.[41, 48, 218, 219] The contribution of the tensor elements to the nonlinear susceptibility of the sample further depends on the fiber orientation relative the geometry of the mixing laser beams. Early work on the molecular origin of the second-order susceptibility of type I collagen fibers from rat tail tendons was performed in transmission mode with the fibers aligned in the x-direction (x and y defined the sample plane),[195] which allowed separate detection of achiral and chiral signals and an approximately equal contribution to the nonlinear susceptibility was demonstrated.

Subsequently, it was shown that spectral differences in achiral and chiral spectra for the collagen fibers originate from distinctions in the relative signal contributions from the glycine, proline, and hydroxyproline residues, which are the main residues in the Gly-X-Y triplet that defines collagen peptides.[194] Based on vibrational SFG spectra that provide this level of molecular understanding for the nonlinear susceptibility of collagen fibers, a model was created to extract the average pitch angles (tilt relative the fiber axis) for the amide I carbonyl and methylene groups in rat tail collagen fibers from polarization SHG experiments. With 45.82° ±0.46° for the peptide groups and 94.80° ±0.97° for the methylene groups, the values were in good agreement with X-ray diffraction studies of collagen type I model peptides.[49] More recently, the organization and absolute molecular orientation of collagen fibers in tissue samples have been visualized with hyperspectral, phase-sensitive and polarization sensitive SFG microscopies,[220-222] which further demonstrate the detailed information that can be obtained through these approaches.

While vibrational SFG spectroscopy informs on the detailed molecular structure of collagen fibers, it is still not certain that the subtle changes (beginning at the fiber interface) from treatment with surfactants during decellularization would be readily detectable. Therefore, to enhance the structural sensitivity of SFG, we used it in the scattering mode. Vibrational sum-frequency scattering (SFS) was pioneered by Roke et al. and has primarily been applied to spherical sub-micron structures in solution,[28, 30, 136, 138-140, 142-145, 148, 223] for which many of the theoretical details have been described. Recently, we used the technique for the first time to analyze collagen fiber networks in aqueous 3D environments and demonstrated that the spectra are dependent on the angle of detection relative the phase-matched direction.[149] In this work, we show that the scattering patterns in the amide I region are sensitive towards the fiber structure and propose that the technique is suitable to probe subtle changes to the structure of collagen fibers during treatment with SDS solutions. We hypothesize that changes to the SFS signals from the collagen fibers in tissue during decellularization may be correlated with the performance of biologic scaffolds in organ regeneration, providing unprecedented molecular level insights to the collagen fiber structure.

4.3 MATERIALS AND METHODS

4.3.1 *Collagen fiber preparation and SDS treatment*

The fibers were self-assembled in solution from acid extracted bovine collagen type I (TeloCol-5225, AdvancedBiomatrix, Lot #7688). During preparation, all solutions were kept in an ice bath to avoid premature fibrillation. Collagen stock solution was added to a phosphate buffered saline (PBS, 137 mM NaCl, 2.7 mM KCl, 20 mM Na_2HPO_4, 4 mM KH_2PO_4) to reach a final collagen concentration of 1 mg/mL. Before adding the collagen, the PBS had been degassed under vacuum and sonication for 1h and the pH had been adjusted with 0.1M NaOH so that the final pH after addition of the collagen was 7.4. After adding the collagen, 1 mL aliquots were centrifuged at 10,000 g for 45 min at 6 °C. After centrifugation, the supernatants were transferred to new Eppendorf tubes that were immediately incubated at 37 °C for fibrillation. After 24h, the samples were centrifuged at 10,000 g for 5 min at room temperature and the supernatants were replaced three times with a similar PBS solution prepared with D_2O (Sigma Aldrich, 1581882). The pellets of the collagen fiber networks were then stored in the D_2O PBS buffer at 4 °C until use. Some samples were monitored with SHG imaging and SFS spectroscopy while being treated with surfactant solutions, which consisted of 3.5 mM deuterated SDS (d_{25}-SDS, CDN Isotopes, D-2552) in the aforementioned D_2O PBS buffer. This concentration of d_{25}-SDS corresponds to a 0.1 % (w/v) of undeuterated SDS, which has previously been used as a low surfactant concentration decellularization protocols.

4.3.2 *UV-Vis absorption*

In each step of the collagen fiber preparation, randomly selected aliquots were chosen for UV-Vis spectroscopy to keep track of the collagen concentration. The supernatants and collagen fiber network samples were dissolved by mixing with 25 mM HCl to obtain a final pH of ~2. Calibration curves were established using reference samples with known concentrations prepared from the collagen stock solution. The absorption was measured at 275 nm with a UV-Vis Varian Cary 5000.

4.3.3 *Vibrational SFS spectroscopy*

For scattering experiments, 75 % of the power from a femtosecond Ti:Al_2O_3 laser (Integra-HE, Quantronix) with 1 kHz repetition rate, 791 nm wavelength, and 110 fs pulse width was used to pump an OPG/OPA/DFG system (Palitra FS, Quantronix) to get a tunable broadband IR beam (~140 cm^{-1} FWHM). At the IR output of the OPG/OPA/DFG, a germanium plate at the Brewster angle blocked residual idler beam in the IR path. The IR path to the sample stage traveled through evacuated lens tubes to minimize absorption in the ambient atmosphere. On the way to the sample stage, a half-wave plate followed by a pair of wire-grid polarizers controlled the power and polarization of the IR beam. The remaining 25 % of the 791 nm pump laser was used to obtain a narrowband (~15 cm^{-1} FWHM) visible/nIR laser beam by filtering the beam with an etalon. Before the sample stage, the power and polarization of the visible/nIR beam were controlled with halfwave plates on either side of a Glan-Laser polarizer. Typical powers at the sample were 10 mW for the IR and 25 mW for the visible/nIR, unless otherwise noted. A motorized delay stage allowed precise control of the temporal overlap between the IR and visible/nIR beams at the sample. For acquisition of scattering patterns and the relative strengths of the various polarization combinations, the total signal intensities were obtained by software binning and the temporal delay was consistently adjusted to yield the highest signal. For acquisition of spectra showing the full line shapes of the amide I region in various polarization combinations and scattering angles, the signal was acquired while slowly scanning the motorized delay stage, to avoid potential issues with temporal chirps of the IR profiles (which were obtained in a similar fashion from a nonlinear optical crystal). While the IR beam was focused directly at the sample (using a CaF_2 lens with 100 mm focal length), the visible/nIR beam was focused about 1.5 cm behind the sample (using a N-BK7 lens with 150 mm focal length), and the incidence angle, γ, between the beams was 10°. The sample was placed between two hemicylindrical CaF_2 prisms with an 800 μm thick rubber gasket spacer. The signal was collected and collimated using a N-BK7 lens with 50 mm focal length, mounted on an arm that rotated around the sample holder. Two apertures were used to limit the spread of collected angles to ±2.5°. The SFS signal was then directed by two silver mirrors through a Glan-Laser polarizer, two premium short pass filters (750 nm cut-off) and one premium long pass filter (650 nm cut-off), before being focused by a N-BK7 lens with 75 mm focal length on to the entrance slit of a spectrograph (IsoPlane-160, Princeton Instruments) operated with a 1200 g/mm grating. The SFS signal was detected with an intensified charge coupled device camera (iCCD, PI-MAX4, Princeton Instruments) operated at 90 gain and with a 40 ns gate width. The number of acquisitions varied between 2,000 and 12,000, depending on the signal strength in the experiment, which was averaged over at least 15 exposures. A schematic overview of the SFS setup is presented in Figure 4.1.

4.3.4 *SHG microscopy*

The SHG images were acquired with a multiphoton microscope (Olympus, FV1000 MPE BX61) pumped with a tunable nIR laser (Spectra-Physics, Mai Tai HP) with 80 MHz repetition rate and 100 fs pulse width. The excitation wavelength was 860 nm and the power was adjusted to about 120 mW at the sample, which did not yield any detectable photodegradation during the acquisition. The setup included two detection arms with photomultiplier tube detectors and a filter cube (FV10-

MR V/G) with bandpass regions of 420-460 nm for the SHG channel and 495-540 nm for the second channel where two-photon excitation fluorescence (TPEF) may appear. Negligible signals were obtained in the TPEF channel and when moving the excitation light to 820 nm, the signal in the SHG channel vanished, which confirmed that the signal indeed was SHG. A 25X/1.05 XL Plan water immersion objective was used and the images were scanned at 100 μs/pixel, with pixel sizes <100 nm (oversampling). The signal was Kalman filtered over 5 sequential acquisitions for each image.

4.4 RESULTS

From the UV-vis experiments (Figure 4.6), the collagen concentration was determined to be 0.54 mg/mL at the start of fibrillation, and the yield was about 92 %. As it takes several hours to acquire a complete SFS scattering pattern for a sample, the signal stability had to be established. The signal strengths in the SPP polarization combination at 0° and 22° for various intensities of the visible/nIR and IR beams were captured and almost perfect linear dependencies for each excitation beam and scattering angle were obtained, as expected (Figure 4.7). After compensating for fluctuations of the IR intensity (the visible/nIR is very stable), the signal captured in the SPP polarization combination at 22° scattering angle was very stable over time and decreased only by a few percent during the first 10h, when the visible/nIR and IR powers were 27.5 mW and 12 mW, respectively (Figure 4.8). The SFS signal at 0˚ decreased slightly more during the same time period with similar incidence beam intensities, but it was also noted that this is not always the case and sometimes the signal in this direction even increases slightly over time. As the signal in the phase-matched direction should be very sensitive towards the organization and preferred orientation of the fibers (see discussion), it is likely that the change in signal strength is due to initial subtle movements of the fibers as the high-powered laser beams are introduced. Regardless, the signal stability, in particular at higher angles, is more than sufficient for reliable investigations of the scattering patterns and the relative SFS intensities in various polarization combinations. It should be mentioned, however, that once the visible power was increased above 30 mW, the SFS signal decreased substantially within tens of minutes (data not shown) due to photodegradation of the sample, which eventually could be observed as a burned spot in the sample by the naked eye. For all subsequent experiments, the visible/nIR and IR powers were thus kept at 25 mW and 10 mW respectively, safely below the damage threshold.

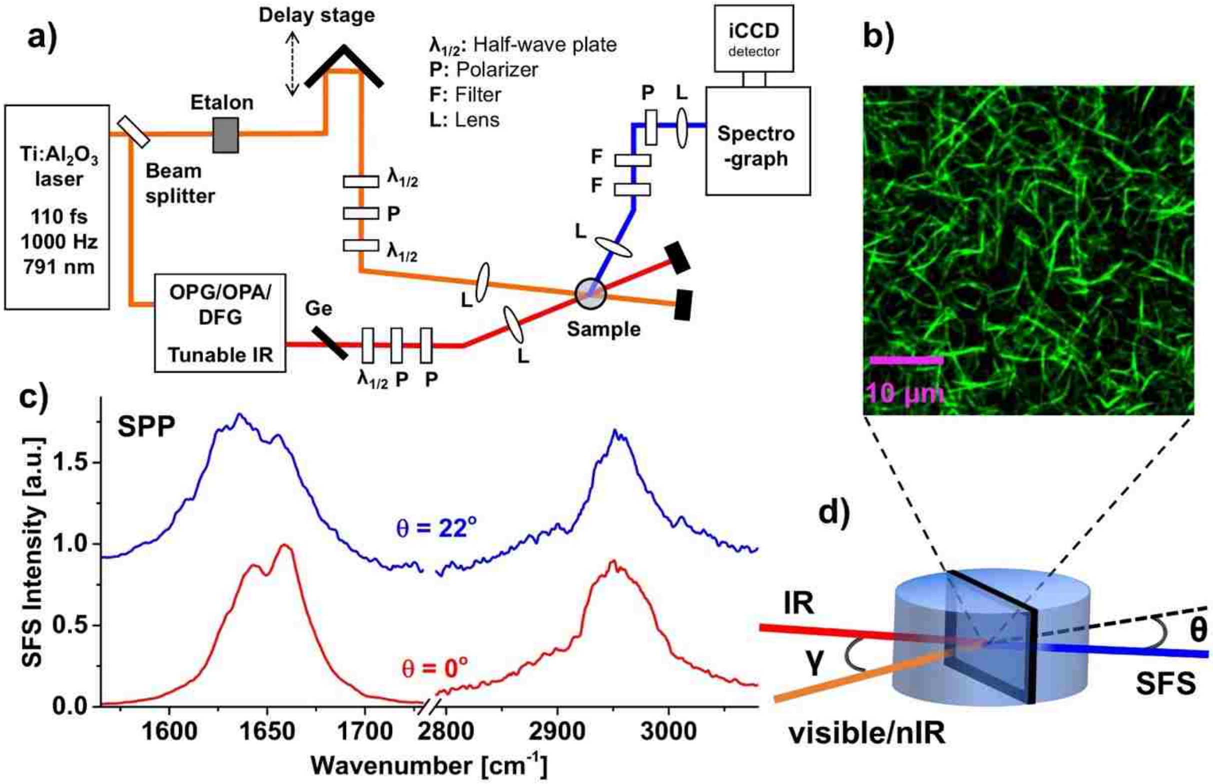

Figure 4.1. SFS setup and spectra from collagen fibers. a) A schematic of the setup for SFS experiments. b) An SHG image of a collagen fiber network in PBS buffer, scale bar is 10 µm. c) Vibrational SFS spectra in the amide I and C-Hx stretching regions for a corresponding collagen fiber network sample, captured at 0° and 22° with the *spp* polarization combination. Note the shift in peak position for the amide I signal with increasing angle. d) A schematic of the sample holder for SFS experiments.

In Figure 4.1, an SHG image of a representative collagen fiber sample is shown and the SFS spectra of the C-H_x stretching and the amide I regions are presented for the *spp* polarization combination. As would be expected for unguided self-assembly in solution, the collagen fibers seem randomly oriented in the sample. This means that chiral signals would be emphasized in the phase-matched direction, as achiral signals are suppressed from samples that are close to isotropic (see discussion). Indeed, when turning the polarization direction of the visible/nIR and IR beams and capturing at the phase-matched SFS signal polarized parallel and perpendicular to the E-fields of the incidence beams, the signal varies with the ability of the polarization combination to probe chiral signals (Figure 4.9), despite the fact that the beam geometries highly disfavors chiral signals in this direction. It turns out that this dominance of the chiral signal in the phase-matched direction is an important indicator for reproducible relative signal strengths of the various polarization combinations at higher scattering angles, which is discussed in more detail below. Another interesting feature demonstrated in Figure 4.1, is the different spectral features observed for the amide I vibrations at the two different angles, with the peak shifting to lower wavenumbers at higher angles.

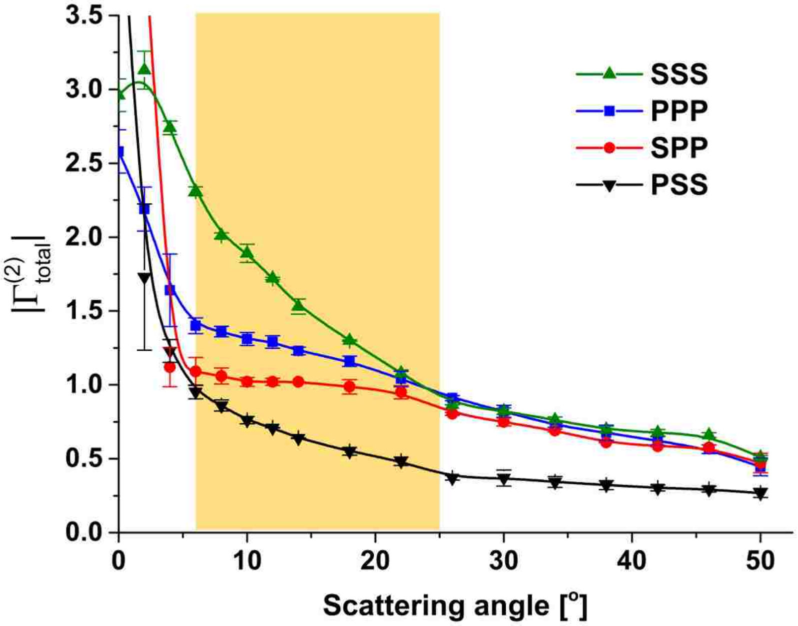

Figure 4.2. The amide I scattering patterns for the square root of the total signal, i.e. $\left|\Gamma^{(2)}_{total}\right|$, captured in the amide I region with *sss, ppp, spp,* and *pss* polarization combinations. The highlighted region denotes strong signal and low standard deviation, determined by measuring three different spots in one sample.

In Figure 4.2, the scattering patterns from 0° up to 50° are presented for *spp, ppp, pss,* and *sss* polarizations. The patterns are captured from three different spots of one sample, which gave very small standard deviations for scattering angles greater than 6° and demonstrates the high reproducibility when capturing SFS patterns from collagen fibers. As the signals in the phase-matched direction are dominant, in particular for the *spp* combination, the graphs in Figure 4.2 are cut-off at 3.5 a.u. and depict the square-root of the signal intensity (which is proportional to the effective susceptibility of the sample, $\left|\Gamma^{(2)}_{eff}\right|$), to clearly visualize how the signal changes at higher angles. This means that the signal is vanishing rather quickly at angles above 25°. At the same time, the standard deviations of the signals at angles below 6° are high. Therefore, it seems like the optimal region for monitoring SFS signals from collagen fibers is within this range. Accordingly, we probed the relative signal strengths of all polarization combinations at 12° and

22˚, as well as complete amide I spectra in *spp, ppp, psss*, and *sss* polarizations at 22°. The phase-matched direction (0°) was also included in all experiments for comparison, as the high signal strengths at this angle allowed rapid acquisition.

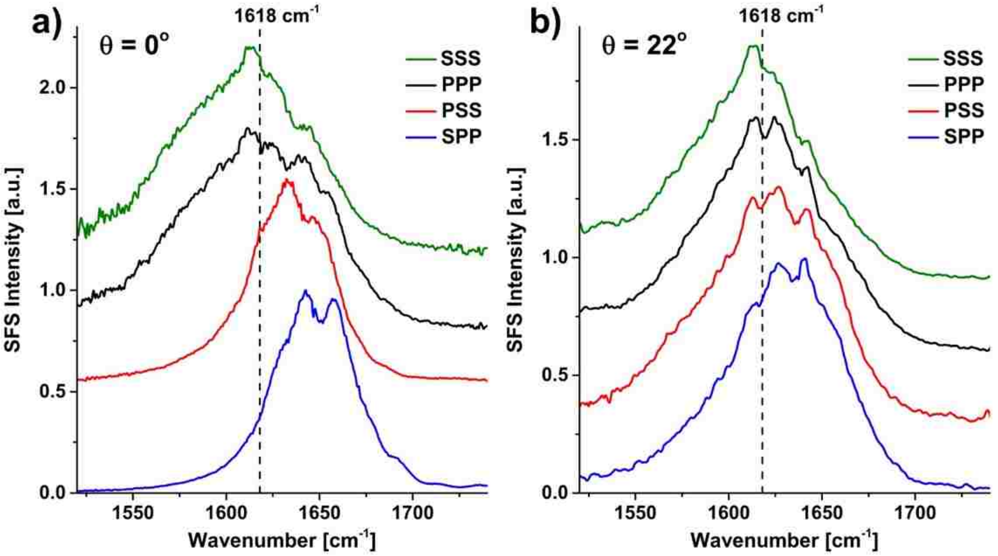

Figure 4.3. The SFS spectra of collagen in *spp, ppp, sss, and pss*. a) The chiral polarization (*spp*) combination appear at higher wavenumbers in the phase-matched direction. b) At 22° all polarizations yield spectra at lower wavenumbers. The dashed lines are guides for the eye.

The spectra are shown in Figure 4.3 and were captured in two steps with the IR peaks centered at ~1580 cm^{-1} and ~1710 cm^{-1} (the IR profiles are shown in Figure 4.10). In the phase-matched direction, the most striking differences are between the chiral (*spp*) and two of the achiral (*ppp* and *sss*) polarization combinations, with a higher peak wavenumber for the former. The remaining polarization (*pss*) appears in between. This is consistent with previous reports that have probed transmission SFG signals in chiral and achiral polarization combinations for collagen fibers aligned on a surface.[194, 195] At higher angles, the peak in *spp* shifts to lower wavenumbers, which may be due to achiral features contributing to the signal. Additional hypotheses for this observation are given in the discussion.

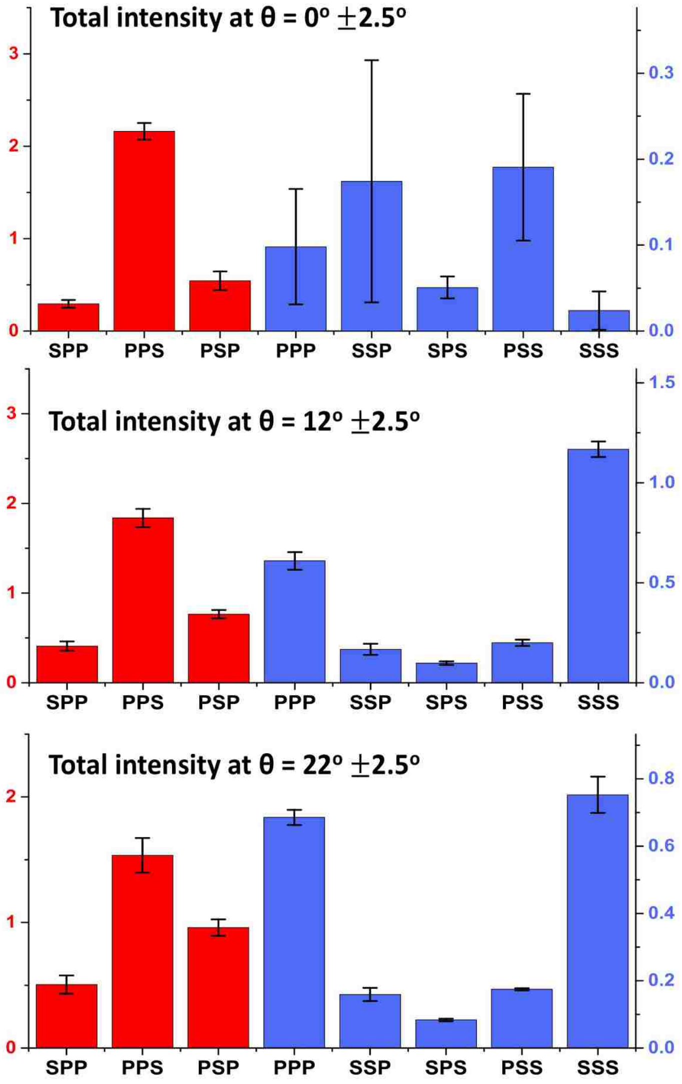

Figure 4.4. The total intensities and St. Dev. for all polarization combinations in the amide I region captured at 0° (top), 12° (middle) and 22° (bottom) scattering angles, from one spot each of three different samples. The achiral (blue) signals varies strongly in the phase-matched direction, but are reproducible at higher angles, while the chiral (red) signals are consistent for all angles.

Figure 4.4 shows the total intensity for all the different polarization combinations at 0°, 12°, and 22°, captured from one spot each of three different samples. The red columns represent the chiral polarization combinations and the blue columns represent the achiral ones. The most striking feature concerns the standard deviations, which are large for the achiral signals in the phase-matched direction, but relatively low for the achiral signals at higher scattering angles as well as the chiral signals at all scattering angles. Empirically, for the beam geometries in these experiments, with a 10° incidence angle between the visible/nIR and the IR beams, it was observed that the relative signal intensities for the achiral signals away from the phase-matched direction were highly reproducible when the sum of the chiral signals at 0° was at least 5 times higher than the sum of the achiral signals, which was the case for all samples probed in Figure 4.4. When the achiral signals at 0° approaches or exceeds the chiral signals in magnitude, it is an indication that the fibers have a preferred orientation, which affects the SFS signal strengths for the various polarization combinations at higher angles and probably also the scattering patterns. However, as long as the fibers are randomly oriented, the scattering patterns and relative signal strengths should primarily be determined by the size and molecular structure of the fibers. Therefore, the relative signal strengths of *spp, ppp, pss,* and *sss* polarization combinations were monitored at a scattering angle of 22° for a sample with $\sum I_c/\sum I_a \approx 8.2$ at 0° while the fibers were exposed to a 3.5 mM d_{25}-SDS solution in PBS buffer at pH 7.4 (Figure 4.5b).

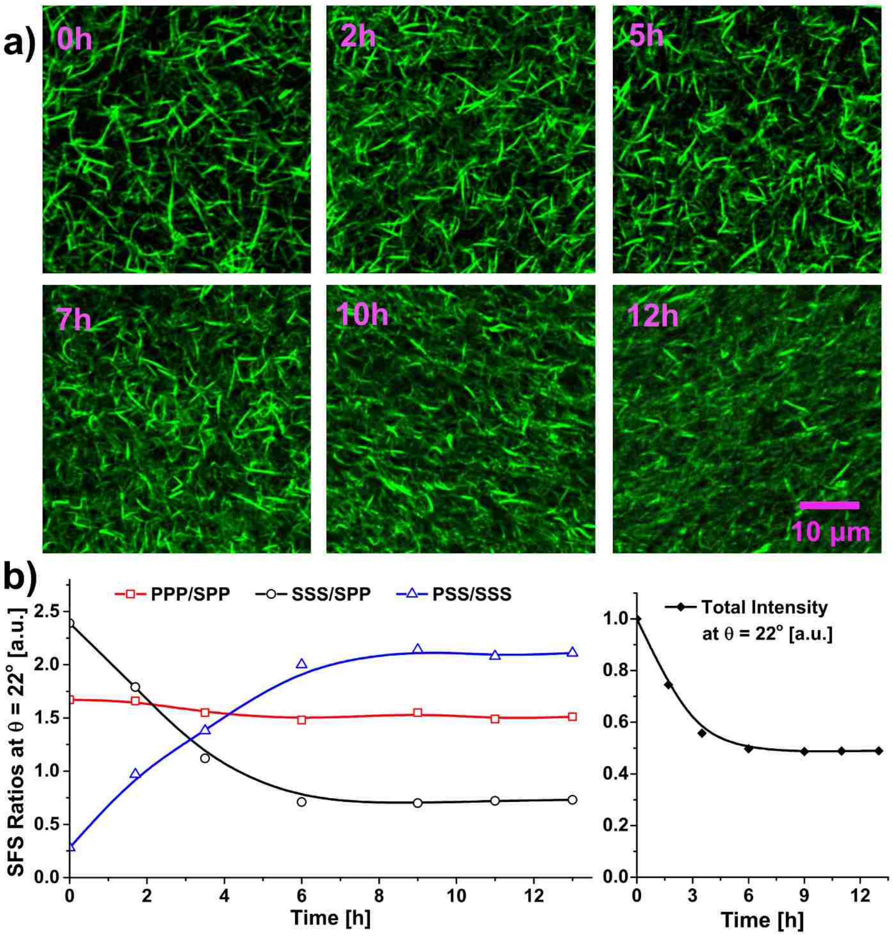

Figure 4.5. SHG images and SFS intensities during d_{25}-SDS treatment. a) SHG images of a collagen fiber network while being exposed to 3.5 mM d_{25}-SDS at 0h, 2h, 5h, 7h, 10h, and 12h. Eventually, the fibers lose their structure and almost "melt" together, before being completely dissolved. b) Polarization combination ratios, *ppp/spp* (red squares), *sss/spp* (black circles), and *pss/sss* (blue triangles) captured at θ = 22°. The changing ratios are accompanied with a reduction in the combined intensity of the four polarization combinations (right panel), which also stabilizes after 6h.

A similar experiment was performed while the fibers were imaged with SHG microscopy (Figure 4.5a) that clearly shows the fiber structures are affected by the treatment. The sample goes from a network of individual fibers with high contrast to less defined structures that appear to partially "melt" together after 12h. When exposed to higher concentrations of d_{25}-SDS during agitation on an orbital shaker at 300 rpm, the fibers were completely dissolved within one day. It is thus clear that the fibers are severely affected by the surfactant treatment, and it is therefore not surprising that the ratios of the various polarization combinations in SFS are changing over time (Figure 4.5). However, changes are readily observable with this technique already at short time periods (<6h), after which the signals in the various polarization combinations stabilize, while the SHG imaging more clearly detects changes to the collagen structure at longer time scales (>6h).

4.5 DISCUSSION

Most SFS studies have been performed on spherical structures where the probed molecular groups reside on the surface, but theoretical models for molecules adsorbed at the surface of arbitrarily shaped particles have also been developed.[150] The collagen fibers are different, however, as they are long cylindrical structures with ordered groups also in the bulk region of each fiber. No theoretical model for the expected scattering patterns of such structures exists today, but many of the general principles regarding sample symmetries and chirality should still hold, which allows a qualitative discussion of the results. For instance, arbitrary sample rotations around any axis should yield a situation with the same nonlinear optical response, provided that the fibers are isotropically arranged. If the fibers contribute coherently to the signal, it would lead to contradictions in the achiral tensor element, unless they are close to zero. However, this is not the case for the chiral tensor elements, which therefore should dominate the signal in the phase-matched direction (which has a long coherence length) for isotropic samples.[70, 144, 224, 225] The chiral polarization combinations were dominant, even when a small angle between the incidence beams ($\gamma = 10°$) was used that geometrically disfavors the chiral tensor elements in the phase-matched direction, which is a strong indication that the samples studied in this work were near-isotropic. This is expected for fibers that have been randomly self-assembled in solution and visual inspection with SHG imaging confirms this conclusion. However, occasionally, the handling of the fiber networks (e.g.

the centrifugation step in the preparation and when placing them in the SFS sample holder) seemed to induce regional long-range ordering of the fibers, which lead to strong achiral responses in the phase-matched direction. The scattering patterns were not reproducible for such samples and have not been included in this work. Elucidating the impact of macroscopic directionality of the fibers will be important for the application of SFS to real tissue samples, in which the collagen fibers often are aligned, but this is beyond the scope of this work. Empirically, it was noted for our setup that the scattering patterns and relative signal strengths of various polarization combinations were readily reproducible when the sum of the chiral signals dominated over the achiral signals by at least a factor of 5 (i.e. $\sum I_c / \sum I_a > 5$) in the phase-matched direction (0° scattering angle).

The large standard deviations for the phase-matched achiral signals in Figure 4.4 are also related to the fact that the fibers are arranged randomly. For a random arrangement of molecules, the sum-frequency response is expected to grow linearly with the molecular number density (a combined effect of a random walk in 3D and the square dependence on the nonlinear susceptibility). For such cases, the low hyperpolarizability, β, of the individual molecules yields a response below the detection limit, precluding signal contributions from e.g. the solvent. However, for collagen fibers, which contain millions of ordered amide groups adding constructively to each other, the effective hyperpolarizability, β_{eff}, is very large. As a result, achiral signals may be produced in the phase-matched direction, even if the fibers are randomly arranged and the nonlinear susceptibility tensor elements would normally be close to zero. However, as discussed above, the achiral response is still much weaker than the chiral signal, which is quadratically dependent on the fiber number density. Nevertheless, detectable achiral signals may be produced to some extent but the signal strengths for various polarization combinations would be heavily dependent on the specific direction of the small random anisotropy of the sample, which yields large standard deviations.

As the scattering angle is increased, the fibers start to add incoherently to the SFS response, and the suppression of achiral signals vanishes. This means that the small random anisotropy has less impact on the signal strength of the various polarization combinations, which leads to small standard deviations. Also, the signal strengths of the chiral and achiral polarization combinations become more similar. As the *spp* polarization combination shifts its peak position to lower wavenumbers similar to those for *sss* and *ppp*, it appears the chiral and achiral β_{eff} cross over the sample susceptibilities, which is not the case for molecules adsorbed at the surface of spherical particles.[144] However, such a distinction would not be surprising, as the fibers have a clear symmetry axis for which all orientations are represented in the sample, in contrast to spherical structures with no specific symmetry axis. In fact, if the individual fibers have C_∞ symmetry, so that the rotation angle around their axes cannot modulate the signal, it is easy to show theoretically that achiral tensor elements of β_{eff} will appear in susceptibility tensor elements probed by chiral polarization combinations. Another possible contribution to the shifting peak positions are that different regions of the fibers are emphasized at different angles, depending on how the phase-shifts across the fibers yield constructive and destructive interferences between the molecular groups in the structure. For this reason, there should be a scattering angle where the surface region of the fibers is enhanced. This angle was not known *a priori* for the samples in this work, but the data from the fibers treated with d_{25}-SDS indicate that 22° provides at least partial specificity for the interface of fibers.

As the collagen fibers in this work were self-assembled in solution, without any cross-linking agents or other stabilizing material, it is reasonable that the weak intermolecular forces make them more sensitive towards environmental conditions than the fibers found in tissue. Therefore, the fibers were treated with relatively low concentrations of d_{25}-SDS surfactants (3.5 mM) without agitation, as they would otherwise rapidly dissolve. In the SHG imaging, it was observed that the fibers eventually lose their structure and almost melt together during the treatment and finally become completely dissolved. However, the early effects of the surfactant treatment, when the d_{25}-SDS interacts with and affects the interfacial structure of the fibers were not readily observed with SHG imaging. In contrast, SFS at 22° showed changing ratios of the polarization combinations, as well as an associated signal reduction over time, during this early phase of the treatment. The fiber number density may have been slightly different for the samples, which could affect the dynamics of the process (i.e. the sample in the SFS experiment may have reached the "melted" stage sooner). However, it is clear that the two techniques provide different and complementary information, since the changes in the SHG imaging did not appear until longer times when the overall structure of the fibers was affected. We hypothesize that the immediate trends observed for SFS at 22° is due to specificity for the surface region of the fibers, which is the first part of the fibers to be affected by the d_{25}-SDS treatment. As the fibers approach the "melted" stage, the surface region of the fibers appears to reach a steady state with little change to the SFS signals at 22° as time progresses. A few data points for the SFS polarization ratios were also probed at 12° scattering angle (data not shown), but no clear trends could be observed, which is likely because the surface specificity was not as high at this angle. A final comment is that the surfactants in solution do not appear in SFS spectra, but they may produce a signal if they interact with the fibers and adopt a preferred orientation at the fiber surface. SFS provides thus an avenue to directly probe these interactions and correlate them with the changes to the fiber structure. Optimizing the setup for such investigations would be challenging and is not addressed here, but this work shows that a good starting point for such efforts might include monitoring the response at a scattering angle of approximately 22° (however, the optimal angle is expected to depend on the IR wavelength). Finally, while this work is focused at the protein-specific amide I region, the collagen fibers also exhibit strong C-H_x stretching signals. Differences in the organization for these groups may yield distinct scattering patterns and sensitivities towards structural changes of the fibers, which represents another avenue for future SFS investigations of collagen fibers.

4.6 CONCLUSIONS

In this work, we have investigated the SFS patterns and relative signal strengths of various polarization combinations in the amide I region for hydrated collagen type I fiber networks. We showed that for randomly oriented fibers the chiral signals are dominant in the phase-matched direction, and that the achiral signals are not reproducible for this direction. In contrast, achiral and chiral signal strengths are comparable at scattering angles above 6° with high reproducibility. When treated with surfactants, the SFS polarization ratios at a scattering angle of 22° can be used to monitor early changes to the collagen fiber structure. This sensitivity towards subtle changes is hypothesized to result from specificity to the surface region of the fibers, which is more adversely affected during the initial phase of the SDS treatment. This shows that SFS may become an important technique that provides information on the surface structure and chemistry of protein fibers, complementary to what can be obtained from other techniques that primarily probe the bulk of the fibers, such as SHG imaging or IR spectroscopy. Such information could be vital for the molecular level understanding of the structural changes to the collagenous ECM of tissues during decellularization and could help optimize the protocols to enhance the success rate of tissue engineered organs.

4.7 SUPPLEMENTARY INFORMATION

As the quality of collagen fibers is dependent on the collagen concentration during the self-assembly process, it was important to establish exactly what the concentration was before the solutions were incubated in 37 °C for fibrillation. This was done by UV-vis spectroscopy at 275 nm and the results are presented in Figure 4.6, which includes absorption of the samples (the aliquots were arbitrarily chosen from one batch of sample preparation) after the centrifugation, in the solution after fibrillation, as well as the fiber network after assembly. A calibration curve was established with solutions of known collagen concentration, prepared from the collagen stock solution. The fibers were centrifuged by 10,000 g into a small pellet and dissolved in 25 mM HCl before analysis. The results indicate an approximate collagen concentration of 0.54 mg/mL at the start of fibrillation, which had a high yield (~92 %).

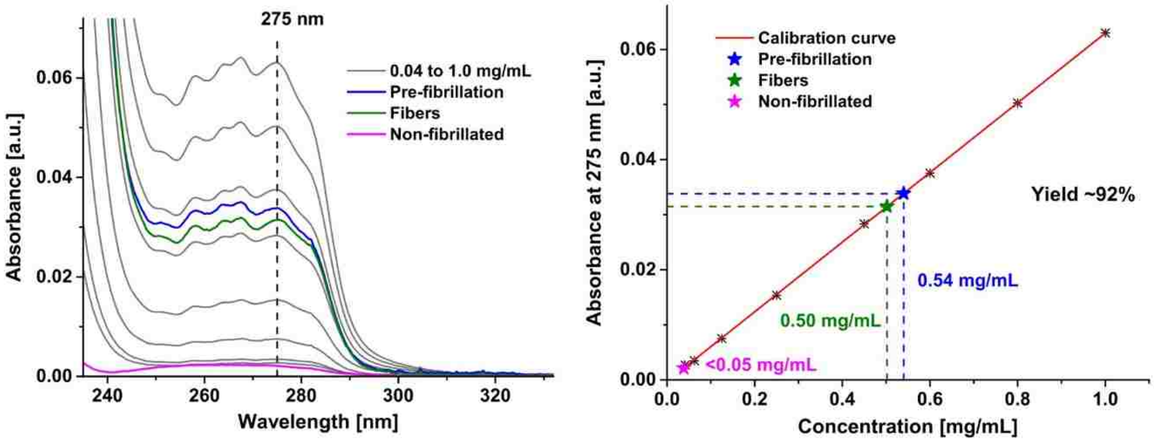

Figure 4.6. The concentration of collagen in the supernatant after the centrifugation (blue), just before the fibrillation was initiated, as well as of the fiber network after fiber assembly (green) and the remaining non-fibrillated collagen in the aqueous phase (magenta). Random aliquots were selected in each step.

Also, in order to compare signal strengths between experiments and different polarization combinations, which could use different excitation powers, it was necessary to demonstrate that the signals scale linearly with the excitation beam powers, as described by Eq. 4.1

$$I_{SFS} = \left|\Gamma^{(2)} \cdot E_{\omega_{Vis}} \cdot E_{\omega_{IR}}\right|^2 \tag{4.1}$$

where $E_{\omega_{Vis}}$ and $E_{\omega_{IR}}$ are the electric fields of the Vis and IR beams, respectively, and $\Gamma^{(2)}$ is the effective susceptibility for the material under study. The graphs are presented in Figure 4.7 below and the dependencies are almost perfectly linear over a wide range.

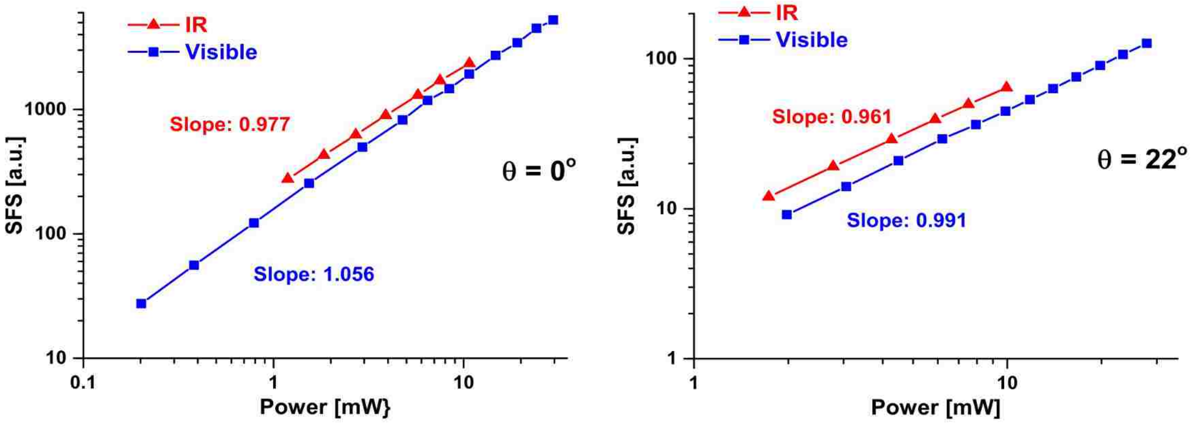

Figure 4.7. Dependence on the power of the visible/nIR and the IR beams (blue squares and red triangles) excitation beams over a wide range, the SFS response scales linearly, as would be expected based on Eq. 4.1 describing the SFS response. This is the case both in the phase-matched direction (0°, left) and higher scattering angles (22°, right).

In Figure 4.8, it is demonstrated that the signals are stable over long time periods, which means that the changing intensities at different scattering angles and during the treatment of d_{25}-SDS are not due to photodegradation.

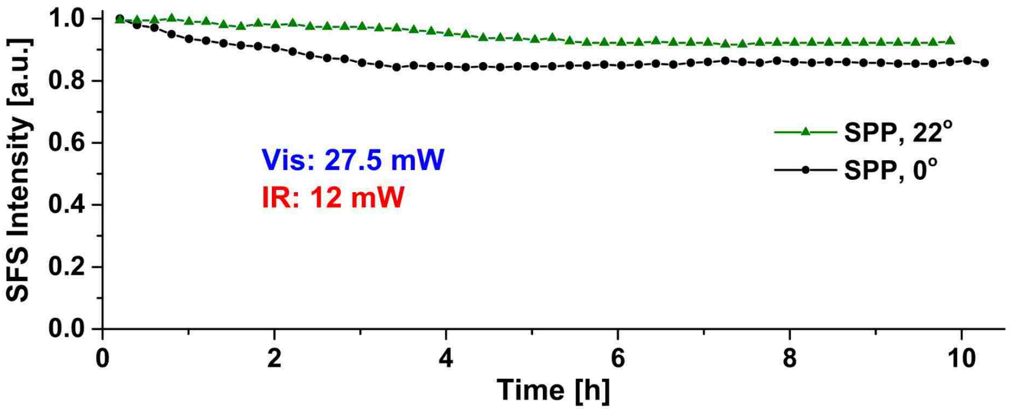

Figure 4.8. Signal stability after onset of the laser beams (0h) onto the sample, the signal intensity stays stable over long time periods for the scattering angles away from the phase-matched direction (22°, green triangles). In the phase-matched direction (0°, black circles), the signal eventually stabilizes, but may either decrease or increase slightly in the beginning (a decrease in the case shown).

To confirm that the fibers are randomly oriented in the samples, the polarization directions of the excitation beams were rotated between 0° and 180° in steps of 10°, while the SFG signal in phase-matched direction was probed (polarized parallel and perpendicular to the incidence beams, as well as the total signal). The results are presented in Figure 4.9 and show that the signal strength is dependent on the capacity to probe chiral features, rather than any preferred fiber orientations. This is consistent with randomly oriented fibers in a sample, for which chiral features should dominate. A more thorough discussion regarding this is provided in section 4.5 of this chapter.

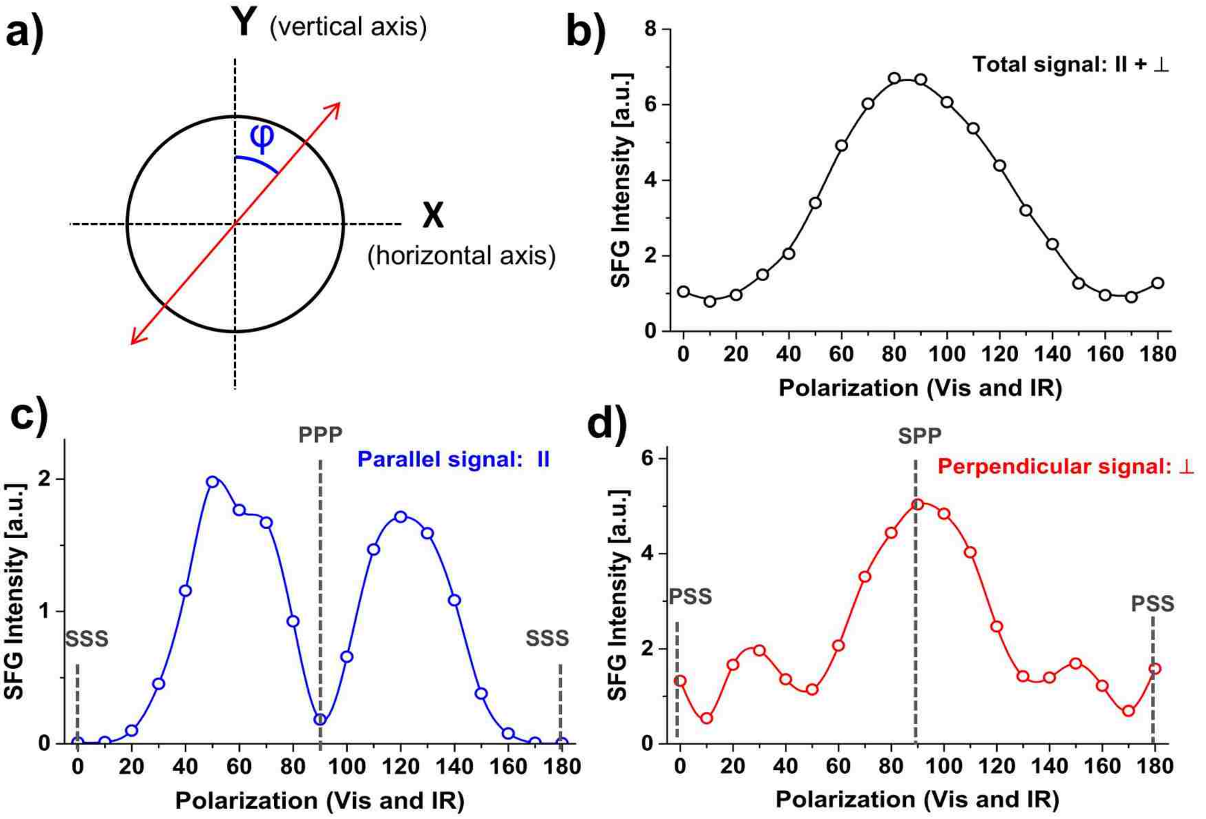

Figure 4.9. The effects from turning the polarization direction (a) of the visible/nIR and IR beams on the total signal in the phase-matched direction (b) as well as the signal split up into the components polarized in the same direction (c) and the perpendicular direction (d) as the incidence beams. From these graphs, it becomes clear that the signal strength is heavily dependent on the ability to probe chiral features in the sample, as the pure achiral polarization combinations (*sss, ppp,* and *pss* in these graphs) have low signal strengths.

Finally, the spectra that show the full line shapes of the amide I vibrations in Figure 4.3 were captured in two steps with the IR peak at two different positions, as the FWHM of the IR is not sufficient for capturing spectra of high quality in the complete amide I region. The two IR profiles are shown in Figure 4.10 and the regions that each profile contribute with towards the spectra are highlighted with shaded regions.

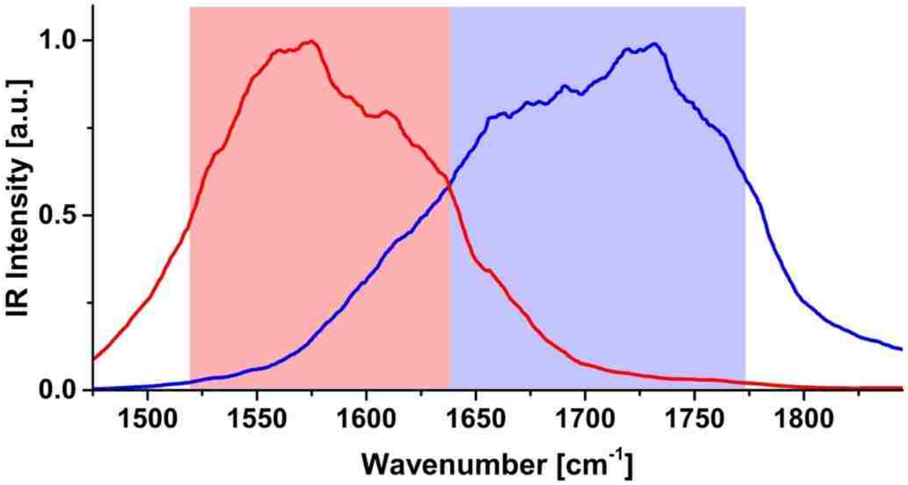

Figure 4.10. The profiles of the IR beams used to probe and normalize the complete amide I spectra presented in Figure 4.3. The respective contribution of the two profiles to the probed spectra are highlighted with blue and red.

Chapter 5. LABEL-FREE IMAGING OF AMYLOIDS USING THEIR INTRINSIC LINEAR AND NONLINEAR OPTICAL PROPERTIES

This chapter is reprinted with permission from a previously published research article (P.K. Johansson and P. Koelsch, *Biomed. Opt. Express.*, Vol 8, Issue 2, pp 743-756, **2017**, DOI: 10.1364/BOE.8.000743). Copyright (2017) Optical Society of America.

5.1 SUMMARY

The optical properties of amyloid fibers are often distinct from those of the source protein in its non-fibrillar form. These differences can be utilized for label-free imaging or characterization of such structures, which is particularly important for understanding amyloid fiber related diseases such as Alzheimer's and Parkinson's disease. We demonstrate that two amyloid forming proteins, insulin and β-lactoglobulin (β-LG), show intrinsic fluorescence with emission spectra that are dependent on the excitation wavelength. Additionally, a new fluorescence peak at about 430 nm emerges for β-LG in its amyloid state. The shift in emission wavelength is related to the red edge excitation shift (REES), whereas the additional fluorescence peak is likely associated with charge delocalization along the fiber backbone. Furthermore, the spherulitic amyloid plaque-like superstructures formed from the respective proteins were imaged label-free with confocal fluorescence, two-photon excitation fluorescence (TPEF), and second-harmonic generation (SHG) microscopy. The latter two techniques in particular yield images with a high contrast between the amyloid fiber regions and the core of amorphously structured protein. Strong multiphoton absorption (MPA) for the amyloid fibers is a likely contributor to the observed contrast in the TPEF images. The crystalline fibrillar region provides even higher contrast in the SHG images, due to the inherently ordered non-centrosymmetric structure of the fibers together with their non-isotropic arrangement. Finally, we show that TPEF from the insulin spherulites exhibits a spectral

dependence on the excitation wavelength. This behavior is consistent with the REES phenomenon, which we hypothesize is the origin of this observation. The presented results suggest that amyloid deposits can be identified and structurally characterized based on their intrinsic optical properties, which is important for probe-less and label-free identification and characterization of amyloid fibers *in vitro* and in complex biological samples.

5.2 INTRODUCTION

There are many proteins that misfold and aggregate into amyloid-like fibrillar structures upon mild denaturation.[153, 226] Such fibers vary in size, but are typically 5 to 15 nm in diameter, have typical persistence lengths in the μm regime and are chemically and mechanically stable.[227-229] This family of fibers has backbones of intermolecular β-sheets that run along the fiber axis.[230] Amyloid fibers are found in a wide range of severe conditions, many of which are becoming increasingly prevalent. Some examples include: Alzheimer's disease, diabetes mellitus type II, and Parkinson's disease - for which the associated proteins are Aβ, islet amyloid polypeptide, and α-synuclein, respectively.[231-235] Other examples of amyloid-forming proteins are insulin and β-lactoglobulin (β-LG),[236-238] which to date have not been shown to induce degenerative conditions. As a result, these amyloids are well-suited to be used in basic research that aims to develop strategies for identification and characterization of amyloid structures. Additionally, the unique chemical, mechanical, and optical properties of amyloids make them interesting for practical use in engineering applications, such as organic light-emitting diodes, conducting nanowires, drug-delivery systems, among others.[162, 164-167, 239, 240]

It has been shown that lysozyme and Aβ, as well as a few engineered protein sequences, develop intrinsic fluorescence in the visible regime upon aggregation into amyloid fibers.[160, 161, 241, 242] In a few cases, electrical conduction through the amyloid fibers has been reported as well.[161, 243] The origin and specific characteristics of the fluorescence and charge transport of these structures may be complex and multifaceted;[169, 244] however, as these properties can arise even without any ring-structures in the peptide sequence, one mechanism that has been hypothesized for their emergence is charge delocalization along the fiber backbone due to long-range hydrogen bonding of the peptide units.[161, 241, 245, 246] The double-bond form of the resonance structures in a peptide bond resembles a unit that one would expect to be conjugated in a long β-sheet sequence, which grants credibility to this hypothesis.[247] The fact that this resonance form would be highly discouraged in hydrophobic environments further corroborates this theory, since it has been shown that low humidity and vacuum conditions diminish both the fluorescence and charge transport of amyloid fibers.[161, 241] A recent study demonstrated that the intrinsic fluorescence from amyloid fibers is also highly dependent on the pH.[159] This observation was attributed to proton transfer in the fibers, which may modulate the charge delocalization through them and affect the absorption and emission characteristics.

The amyloid deposits in brain tissue from patients with Alzheimer's disease consist of various types of amyloid fiber aggregates, including a spherical superstructure called amyloid spherulites.[179, 180, 248-254] In these structures, amyloid fibers grow radially from the center, where one may find an amorphous core. The existence, size, and, morphology of the amorphous core is dependent on the source protein and the conditions under which they are formed.[175] It was previously demonstrated that the Aβ protein associated with Alzheimer's disease can form spherulites *in vitro*,[180] but until recently the procedure has not been time-efficient and the yield has been moderate.[171] However, insulin and β-LG form both amyloid fibers and amyloid spherulites within hours and with high yields - therefore these proteins were used in this study. The assembly process depends on several factors, such as the protein concentration, temperature, pH and ion concentrations, and has been described elsewhere.[172-178, 255, 256] The microscopy efforts in this work focused on spherulites prepared from these proteins and the intrinsic optical properties of these amyloid structures were utilized in label-free imaging applications.

Most studies of amyloid structures by two-photon (or multi-photon) excitation fluorescence (TPEF or MPEF) and second- harmonic generation (SHG) imaging have relied on external probes,[257-262] while only a few have been label-free.[32, 34, 36] In this work, we show that these techniques produce images with high contrast for the amyloids. This can be attributed to the previously demonstrated multiphoton absorption (MPA),[168] being as effective for insulin fibers as for typical two-photon dyes. Furthermore, the nonisotropic organisation and inherent noncentrosymmetry of the fibers in the crystalline fibrillar regions enhance their SHG susceptibility. In the following sections, we first briefly describe the preparation procedures that lead to either individual fibers or spherulites. The fibers were visualized by atomic force microscopy (AFM), while the spherulites were identified with cross-polarized microscopy. We then present the ultraviolet-visible (UV-Vis) absorption, as well as the fluorescence spectra and fluorescence lifetimes of the native proteins and the amyloid structures. Finally, we show images of the spherulites produced by confocal fluorescence, TPEF, and SHG microscopy without using any probes or labels.

5.3 MATERIALS AND METHODS

5.3.1 *Preparation of the Fibers and Spherulites*

Insulin fibers were prepared by dissolving 10 mg insulin (I5500, Sigma Aldrich) in 4 mL 25 mM HCl, followed by 18h incubation at 70 °C while stirring with a magnetic stir bar at 300 rpm. β-LG fibers were prepared by dissolving 20 mg β-LG (L0130, Sigma Aldrich) in 4 mL 25 mM HCl, followed by 42h incubation at 85 °C while stirring with a magnetic stir bar at 300 rpm. Insulin spherulites were prepared by dissolving 5 mg insulin in 1 mL 25 mM HCl and 5 mM NaCl, followed by 6h incubation at 70 °C without stirring. β-LG spherulites were prepared by dissolving

20 mg β-LG in 1 mL 25 mM HCl and 5 mM NaCl, followed by 18h incubation at 85 °C without stirring. MilliQ water (18.2 MΩ) was used in all solutions and the prepared fibers and spherulites were stored in 4 °C. Before use, each sample was centrifuged (5000g x 5 min for the fibers and 200g x 2 min for the spherulites) and resuspended twice in 25 mM HCl post-assembly, to reduce the amount of non-assembled protein.

5.3.2 *Atomic Force Microscopy*

The amyloid fiber solutions were diluted with 25 mM HCl to a final concentration of about 1 mg/mL followed by adsorption on clean Si substrates during 3 min. The surfaces were then rinsed by submersion into MilliQ water for 5 min. After drying with N_2 gas, the surfaces were imaged with PeakForce AFM (Bruker-ICON).

5.3.3 *Cross-Polarized Microscopy*

Droplets containing spherulites (undiluted) were put on microscope slides with coverslips on top. An in-house microscopy setup was used, with the sample between orthogonal linear polarizers. The images of the spherulites were captured with a charge-coupled device camera.

5.3.4 *UV-Vis Absorption, Fluorescence Spectroscopy and Decay*

Solutions with about 5 mg/mL protein in 25 mM HCl were prepared for all the amyloid samples and the native proteins. Absorption spectra from 240-500 nm were measured with a UV-Vis spectrometer (Varian Cary 5000) with a 25 mM HCl solution as the blank. Baseline correction was made with a model according to Eq. 5.1,

$$Abs = -\log\left[\frac{I_{obs}}{I_0}\right] + \log[1-A] + \log\left[\frac{1-B}{\lambda^4}\right] \qquad (5.1)$$

where I_{obs} is the measured intensity for the sample, I_0 is the intensity for the blank, $1 - A$ is the transmittance due to reflection/blocking at large structures, and $(1 - B)/\lambda^4$ is the transmittance due to wavelength dependent scattering. The A and B factors were optimized to accomodate a flat baseline at zero at $\lambda > 430$ nm, for which little absorption was expected. All absorption spectra were normalized at 278 nm. The fluorescence spectra were acquired with a spectrofluorometer (Tecan, Infinite M1000), with λ_{exc} ranging from 310 nm to 450 nm. The relative signal intensities for the various λ_{exc} were noted for each sample and the spectra were normalized to their maximum values. The fluorescence decays were measured with a time-correlated single photon counting spectrometer (Picoquant, FluoTime 100) and the instrument response function was captured with 250 nm poly-L-lactic acid particles at low concentration. For all decay measurements, the integration time was adjusted so that the maximum count for each sample reached 10,000 and all results were fitted with double-exponential functions.

5.3.5 *Confocal Fluorescence, Two-Photon Excitation Fluorescence, and Second-Harmonic Generation Microscopy*

Droplets of the spherulites (undiluted) were placed on microscopy slides with cover slips on top, and then imaged. The fluorescence images were captured with a 40X/1.30 Plan-Neofluor oil immersion objective on a confocal microscope (Zeiss LSM 510 Meta) operating with λ_{exc} at 405 nm from a diode-pumped solid-state laser. The detection channel had a photon multiplier tube (PMT) and a longpass filter with a cut-on wavelength at 420 nm. The TPEF and SHG images were acquired with a multiphoton microscope (Olympus, FV1000 MPE BX61) pumped with a tunable nIR laser (Spectra-Physics Mai Tai HP) with 80 MHz repetition rate and 100 fs pulse width. Unless otherwise noted, λ_{exc} was 910 nm and the excitation laser power was 680 mW at the sample. No photodegradation was observed during acquisition for excitation powers below 1.2 W. Both detection arms had PMT detectors and included bandpass filters at 420-460 nm for the SHG channel and 495-540 nm for the TPEF channel. A 25X/1.05 XL Plan water immersion objective was used and the images were scanned at 100 µs/pixel, with pixel sizes <200 nm. For all the TPEF and SHG images in this work, the expected pump laser polarization orientation is 45° clockwise. When λ_{exc} was moved to 930 nm with the same pump power and detector settings, the intensity in the SHG channel decreased to about 5 % while over 90 % of the signal in the TPEF channel remained. This procedure was used as a confirmation that a majority of the signal detected in the SHG channel originates from SHG processes, while TPEF is detected in the TPEF channel. We also meassured TPEF in both channels with a range of λ_{exc} to observe how the relative intensities are dependent on the wavelength. For these studies we made additional measurements with another filter setup, allowing 460-500 nm in one detector arm and 520-560 nm in the other.

5.4 RESULTS AND DISCUSSION

5.4.1 *Preparation and identification of fibers and spherulites*

When proteins are brought to mild denaturation, they reach a flexible state that allows misfolding, reorganization and subsequent aggregation that may result in amyloid-like fibers. Insulin and β-LG are two proteins that form these fiber structures when heated close to their melting temperatures in acidic conditions.[186, 263] Thus, we dissolved bovine insulin and β-LG from bovine milk in 25 mM HCl water solutions and heated them to 70 °C and 85 °C, respectively. To promote fiber formation, lower concentrations (2.5 mg/mL for insulin and 5 mg/mL for β-LG) were used and 300 rpm stirring was applied to the solution. Higher concentrations (5 mg/mL for insulin and 20 mg/mL for β-LG) with 5 mM NaCl (not stirred) were used to favor spherulite formation.[172, 174] The amyloid fibers were adsorbed onto Si surfaces and imaged with AFM (Figure 5.1).

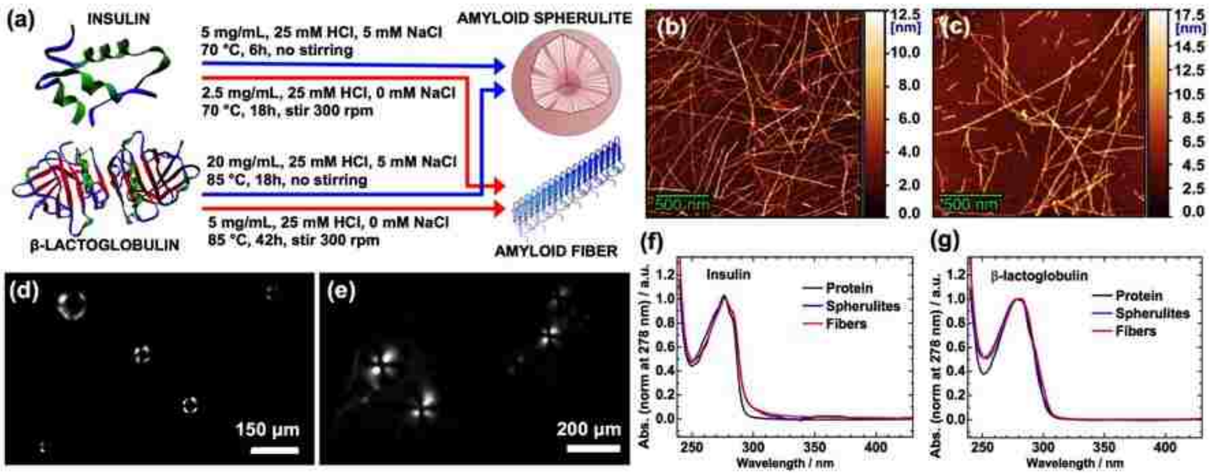

Figure 5.1. Preparation and characterization of amyloid fibers and spherulites. (a) Insulin and β-LG form fibers or spherulites, depending on the experimental conditions. AFM images of amyloid fibers from bovine insulin (b) and β-LG from bovine milk (c); bars are 500 nm for both images. Cross-polarized microscopy of the spherulites from insulin (d) and β-LG from bovine milk (e); bars are 150 μm for (d) and 200 μm for (e). Normalized absorption spectra of the native proteins (black), amyloid fibers (red), and amyloid spherulites (blue) from the bovine insulin (f) and the β-LG from bovine milk (g), in 25 mM HCl solutions at ~5 mg/mL protein concentration.

When spherulites are imaged with cross-polarized microscopy, a characteristic Maltese-cross pattern appears due to the birefringent nature of amyloids, for which the optical axis is along the fiber. Therefore, the spherulites were imaged with a home-built cross-polarized microscopy setup to confirm their formation (Figure 5.1). At the center of the insulin spherulites, a dark region is observed in the structures, for which an associated large amorphous core has been suggested.[174, 175, 177, 178] For β-LG spherulites, the corresponding dark region at the center is small, which implies a small or non-existent amorphous core. Finally, UV-Vis absorption spectra were captured and the expected absorption of the ring-structures in the proteins at about 278 nm was detected for all samples (Figure 5.1). A slight peak broadening for the fibers and spherulites was observed for both proteins, which may be related to either residual scattering that could not be compensated for, or a small change in the local environment for the amino-acids with ring-structures. At about 360 nm, a weak peak was observed for the insulin spherulites. This may be an effect from phonons being formed due to the rigid nature of the long amyloid fibers in the spherulites; however, further investigation of the details in this observation is needed and is beyond the scope if this work.

5.4.2 *Characterization of the intrinsic fluorescence*

Before proceeding to imaging the spherulite structures, we thoroughly investigated the intrinsic fluorescence of the fibers, spherulites and native proteins of the insulin and β-LG. For all these samples, intrinsic fluorescence was observed and the emission spectra were dependent on the excitation wavelength (Figure 5.2), which is in conflict with Kasha's rule. Raman scattering moves with the excitation wavelength, but cannot account for all the observed features and Raman microscopy of the spherulites could conclusively exclude this as a viable explanation. However, this effect is based on another well-documented phenomenon - the red edge excitation shift (REES).[264, 265] Solvent interactions result in a statistical distribution of the ground state (E_g) and the first excited state (E_e) energies for the fluorophores. Of this distribution, only the fluorophores having E_g above the mean (E_g) and E_e below the mean (E_e) will be probed when they are excited with light at the red edge of the absorption spectra. If the solvent relaxation (reorientation) is slower than the fluorescence decay, this will lead to a red-shifted emission spectrum, compared to the scenario when the excitation wavelength is sufficient for transitions beyond the gap between E_g and E_e. Usually, REES is not observed for fluorophores in liquid solvents at room temperature, since the solvent relaxation in such cases is sufficiently rapid to consistently yield a transition to the same E_e distribution before radiative decay occurs. However, the dynamics of water and other molecules surrounding the intrinsic fluorophores within proteins are slow enough to allow a substantial wavelength-dependent REES. The absorption peaks for the amino-acids with ring-structured side-chains (typically responsible for the intrinsic fluorescence in proteins) are at about 280 nm. The λ_{exc} used in Figure 5.2 (310 - 450 nm) is therefore far out on the red edge.

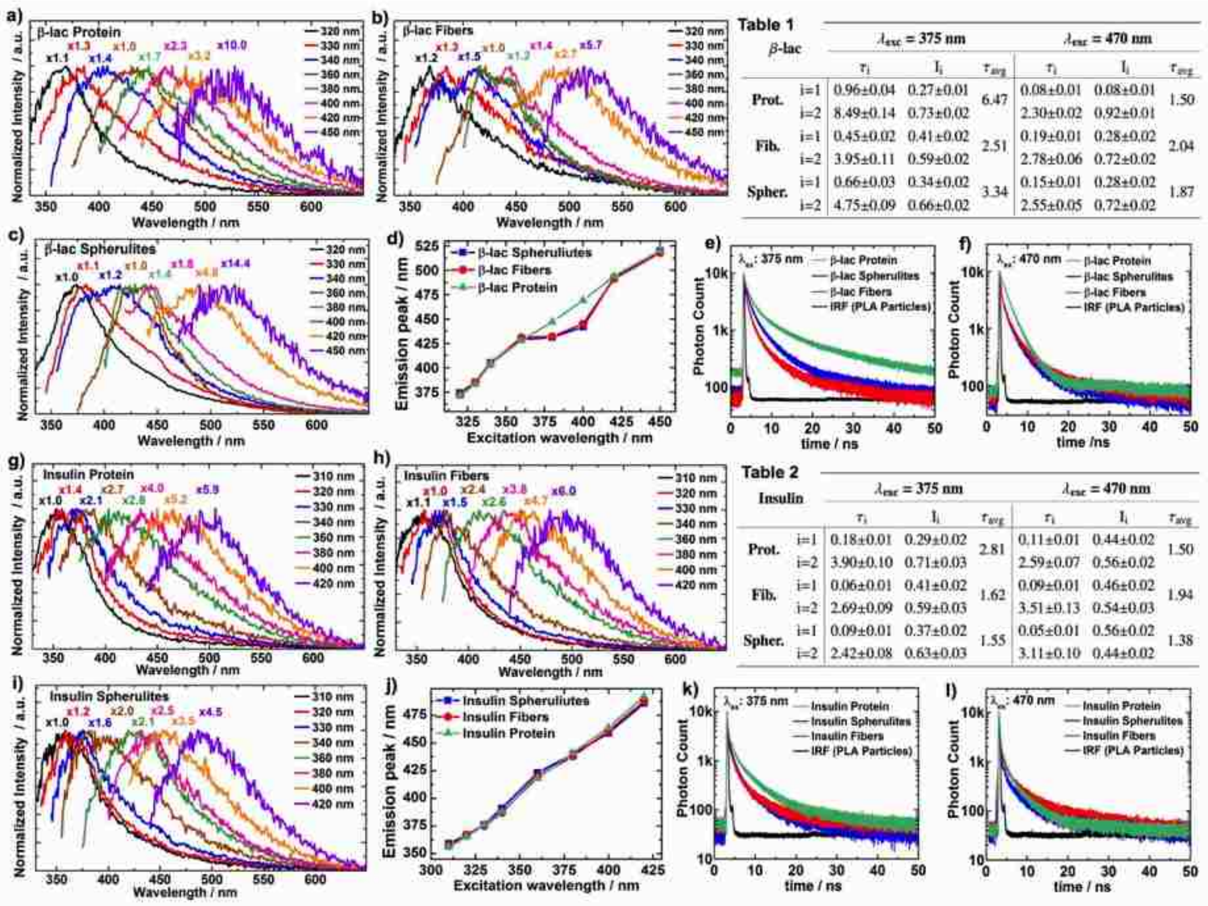

Table 1

β-lac		λ_{exc} = 375 nm			λ_{exc} = 470 nm		
		τ_i	I_i	τ_{avg}	τ_i	I_i	τ_{avg}
Prot.	i=1	0.96±0.04	0.27±0.01	6.47	0.08±0.01	0.08±0.01	1.50
	i=2	8.49±0.14	0.73±0.02		2.30±0.02	0.92±0.01	
Fib.	i=1	0.45±0.02	0.41±0.02	2.51	0.19±0.01	0.28±0.02	2.04
	i=2	3.95±0.11	0.59±0.02		2.78±0.06	0.72±0.02	
Spher.	i=1	0.66±0.03	0.34±0.02	3.34	0.15±0.01	0.28±0.02	1.87
	i=2	4.75±0.09	0.66±0.02		2.55±0.05	0.72±0.02	

Table 2

Insulin		λ_{exc} = 375 nm			λ_{exc} = 470 nm		
		τ_i	I_i	τ_{avg}	τ_i	I_i	τ_{avg}
Prot.	i=1	0.18±0.01	0.29±0.02	2.81	0.11±0.01	0.44±0.02	1.50
	i=2	3.90±0.10	0.71±0.03		2.59±0.07	0.56±0.02	
Fib.	i=1	0.06±0.01	0.41±0.02	1.62	0.09±0.01	0.46±0.02	1.94
	i=2	2.69±0.09	0.59±0.03		3.51±0.13	0.54±0.03	
Spher.	i=1	0.09±0.01	0.37±0.02	1.55	0.05±0.01	0.56±0.02	1.38
	i=2	2.42±0.08	0.63±0.03		3.11±0.10	0.44±0.02	

Figure 5.2. Amyloid intrinsic fluorescence. The data show the intrinsic fluorescence from the β-LG from bovine milk (a-f) and bovine insulin (g-l), at ~5 mg/mL in 25 mM HCl water solutions. Fluorescence emission spectra are shown for the native proteins (a, g), the amyloid fibers (b, h), and the amyloid spherulites (c, i), when λ_{exc} ranges from 310 to 450 nm. The emission peaks are plotted versus the λ_{exc} for both β-LG (d) and insulin (j) for the respective types of samples: native proteins (green, △), amyloid fibers (red, o), and amyloid spherulites (blue, □). The fluorescence decays for λ_{exc} at 375 nm (e, k) and 470 nm (f, l) are presented for the native proteins (green), the amyloid spherulites (blue), and the amyloid fibers (red) – the instrument response function (black) was measured with 250 nm poly-L-lactic acid particles. The double-exponential fitting parameters for the decays are included in Tables 1 (β-LG) and 2 (insulin) for λ_{exc} at 375 nm and 470 nm with 95 % confidence intervals.

Conforming with the REES discussed above, an excitation wavelength dependence of the emission was observed for the native proteins for both the β- LG and insulin. However, when λ_{exc} is decreased to 300 nm and below, the emission obeys Kasha's rule. When we made similar measurements for free tyrosine amino acids in 25 mM HCl solutions, the emission peaks were at no point dependent on λ_{exc} (data not shown). This further corroborates that the mechanism for the observed results is REES, since the solvent relaxation for the free tyrosines is expected to be fast. REES is also largely observed for the fiber and spherulite structures; however, in the case of the amyloids from β-LG, a static weak emission peak appeared at about 430 nm with λ_{exc} at 360 - 400 nm (Figure 5.2). This observation is most likely associated with additional fluorescence arising from charge delocalization along the backbone of the fibers in the amyloid structures, as discussed in the introduction.

To confirm that this is indeed a new fluorescence not present for the native protein, the fluorescence decays were measured for the native protein and the amyloid structures for β-LG (Figure 5.2). When λ_{exc} was 470 nm, similar decays for the native proteins and the amyloid analogs were observed, while faster decays were measured for the amyloids when λ_{exc} was 375 nm. This shows that the faster decay is not an omnipresent feature for the fibers and spherulites throughout the excitation spectra, but is rather indicative of a specific and additional fluorescence pathway when λ_{exc} is 375 nm. Interestingly, a corresponding fluorescence was not readily observed for insulin amyloids, for which the emission spectra exhibited features similar as for the native protein throughout the range of excitation wavelengths used in this work. However, the fluorescence decays show a slightly faster decay for the insulin amyloids compared to the native protein when excited at 375 nm. This may indicate that insulin also develops intrinsic fluorescence in the amyloid state, but with a very low absorption cross-section and/or quantum yield. It is not easy to conclusively determine the origin of the distinctions in the intrinsic optical properties for the amyloid states of β-LG and insulin. However, it is likely that the detailed organizations in these superstructures affect the prospects of charge delocalization in them, for instance via their proton transfer capability.[159] It is therefore not surprising that amyloids from insulin do not exhibit the exact same optical properties as those from β-LG, even though the specific details for the origin of this observation are currently unknown. It has been shown that the intrinsic fluorescence decays from the ring-structures in proteins often require at least double-exponential functions to produce sensible fits. The origin of this feature is non-trival and depends on the specific positioning of the fluorescent amino acids, possible energy transfers between them, as well as transitions to more than one excited electronic state.[265-267] Accordingly, double-exponential fits were used for all samples, which yielded short (τ_1) and long (τ_2) decays (Tables 1 and 2 in Figure 5.2). With λ_{exc} at 470 nm, both τ_1 and τ_2 were quite similar across the samples for each protein and no clear and interpretable trend is observed. For insulin, the fluorescence lifetimes for the amyloid structures were slightly shorter compared to the native protein when λ_{exc} was 375 nm. It seems like τ_2, with the range 2–4 ns, is the main reason for this. A larger distinction in the decay times between the amyloids and the native protein for the same λ_{exc} was observed for β-LG. Both τ_1 and τ_2 were longer for the native protein, however the main difference was again measured for τ_2, which was 4.75 ns and 3.95 ns for the amyloid spherulites and fibers, while it was 8.5 ns for the native protein. The fluorescence lifetimes measured for the β-LG amyloid structures conform with the corresponding values measured for amyloid-specific intrinsic fluorescence of other proteins.[160] The fluorescence with longer lifetime for the native protein is likely from tryptophan, which has been shown to exhibit a wide range of decay times that depend on the environment. For insulin, the main origin of the observed fluorescence for all samples is likely from the tyrosine residues in the protein, which lacks tryptophans.

5.4.3 *Label-free imaging of amyloid spherulites*

The intrinsic fluorescence investigated in the previous section can be utilized for label-free imaging of the amyloid spherulites in solution (Figure 5.3). Scanning confocal fluorescence microscopy with λ_{exc} at 405 nm was used to image the insulin and β-LG spherulites. TPEF and SHG microscopy with λ_{exc} at 910 nm also produced clear images of the spherulites. Power dependence plots for the average pixel intensity of the spherulite structures revealed a quadratic relationship (1.95 for insulin and 2.05 for β-LG) for the SHG images, as expected. A nearly quadratic relationship (1.78 for insulin and 1.86 for β-LG) for the TPEF images was measured.

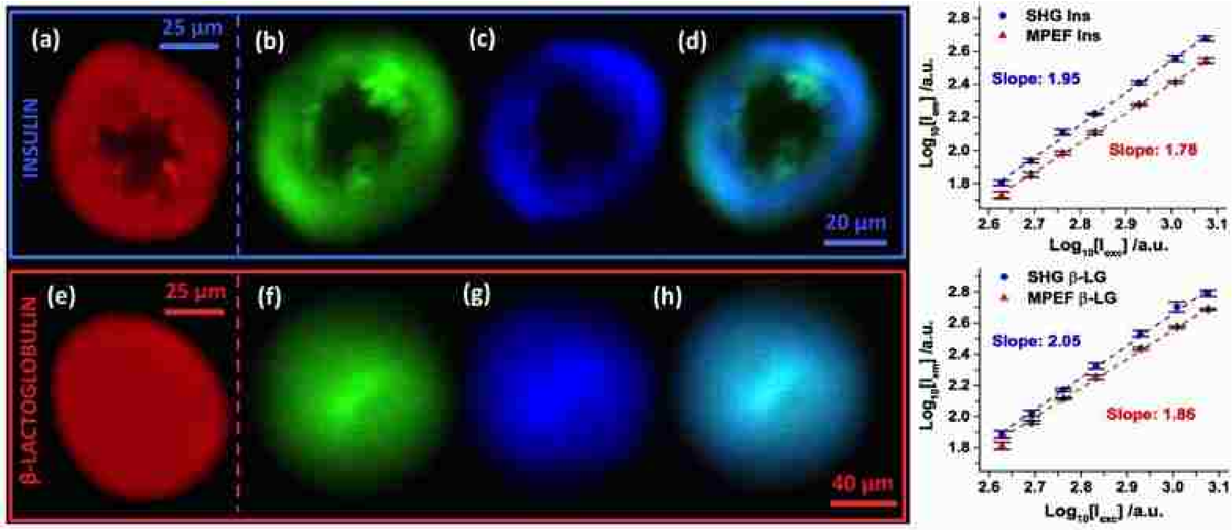

Figure 5.3. Label-free imaging of amyloid spherulites. Spherulites from bovine insulin (a-d) and β-LG from bovine milk (e-h) imaged with confocal fluorescence (a,e - *red*), TPEF (b,f - *green*), and SHG (c,g - *blue*). TPEF and SHG were imaged simultaneously in different channels (420-460 nm and 495-540 nm, respectively) and overlays of the two are shown (d,h). Scale bars: 25 µm (a,e), 20 µm (b-c), and 40 µm (f-h). λ_{exc} were 405 nm (a,e) and 910 nm (b-d,f-h). The SHG and TPEF power dependencies were measured for four replicates of each type of structure with powers ranging from 425 - 1190 mW. The error bars represent standard deviations and the slopes were obtained with least square fits.

The slightly lower power dependence for the TPEF images indicates that a larger relative contribution of linear processes (e.g. linear fluorescence or scattering) is present in this channel. The amorphous cores for the insulin spherulites were large and had quite irregular shapes, while they were non-existent for the β-LG spherulites. Another distinction was that many heterogenous features can be discerned in detail for the insulin spherulites, whereas a homogenous morphology was observed for the β-LG spherulites. A clear contrast between the amorphous core and the surrounding crystalline fiber region in the insulin spherulites was observed for all three techniques. The line-intensities for representative regions of interests are plotted for comparable insulin spherulites to quantify these contrasts (Figure 5.4).

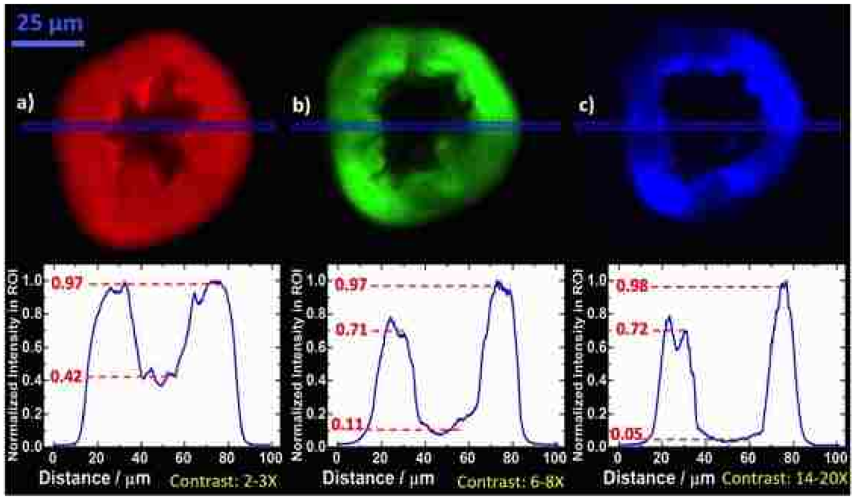

Figure 5.4. Contrast between the amorphous core and fibrillar region. For the bovine insulin spherulites the relative intensities for the core and the fibrillar regions were evaluated by taking regions of interest (dashed blue boxes) linescans for the confocal fluorescence (a - red), TPEF (b - green) and SHG (c - blue). The scale bar is 25 µm for all spherulites and the λ_{exc} were 405 nm (a) and 910 nm (b, c), respectively.

The fiber regions had a 2 - 3x higher intensity for the confocal fluorescence. Based on the analysis in the previous section, the origin of this contrast is likely not due to new fluorescence pathways for the fibers. One contributing factor could be a distinction in protein density, however, it is unlikely that this alone would yield a 2 - 3 times higher intensity. However, it is possible that the packing and rigidity of the fiber regions discourage non-radiative decay pathways in favor of radiative pathways. This would lead to a higher quantum yield for the fiber region without affecting the overall fluorescence decay. Additional contrast was obtained for the TPEF, which had a 6 - 8x intensity difference. After excluding the possibility of hyper-Raman contributions, it was concluded that this is likely due to a strong MPA for insulin amyloids. It has been shown that insulin amyloid fibers exhibit a MPA cross-section comparable to those for good two-photon dyes.[168] In that study, the MPA order exhibited a strong wavelength dependence and was >3 for insulin fibers when $\lambda_{exc} = 910$ nm, which deviates from the order we have measured for TPEF at this wavelength. This indicates that the features that give rise to the wavelength dependence in

MPA are not coupled to emissive decay pathways. However, despite this distinction between the previous study and our findings, a strong nonlinear absorption cross-section exclusively for the fibrillar structures is a likely explanation for the higher contrast in TPEF compared to the confocal fluorescence. As a 40 nm window is relatively large for SHG imaging, there is a risk that some TPEF could emerge in the channel for SHG detection (with a bandpass filter at 420 - 460 nm). Therefore, λ_{exc} was shifted from 910 nm to 930 nm as a control, which would have a limited effect on the observed TPEF, while the SHG signal would vanish completely as it shifts out from the bandpass region for the filter setup. Indeed, the vast majority of the signal disappeared (results not shown), demonstrating the contribution of SHG processes to the SHG images. For the core in the insulin spherulites, one would likely find proteins that are isotropically arranged with a random coil conformation, and the SHG susceptibility would thus be low there. Therefore, the 14 - 20x intensity difference in the SHG image is a clear indication that the cores of the insulin spherulites are indeed amorphous, as has been previously hypothesized. A final comment to make is that the confocal fluorescence response seems uniform for the fiber region in the insulin spherulites, while the responses for the TPEF and SHG are more heterogeneous. This is because the excitation light is polarized in the latter two techniques, which favors fluorescence from fibers with the optical axis aligned with the polarization of the light. Such artifacts can be alleviated by the use of circularly polarized light. However, the polarization dependence can also be utilized to make conclusions about the detailed structure of the sample under study. In our case, the results indicate that the fibers grow radially outward from the spherulite cores, which agrees with previous studies.

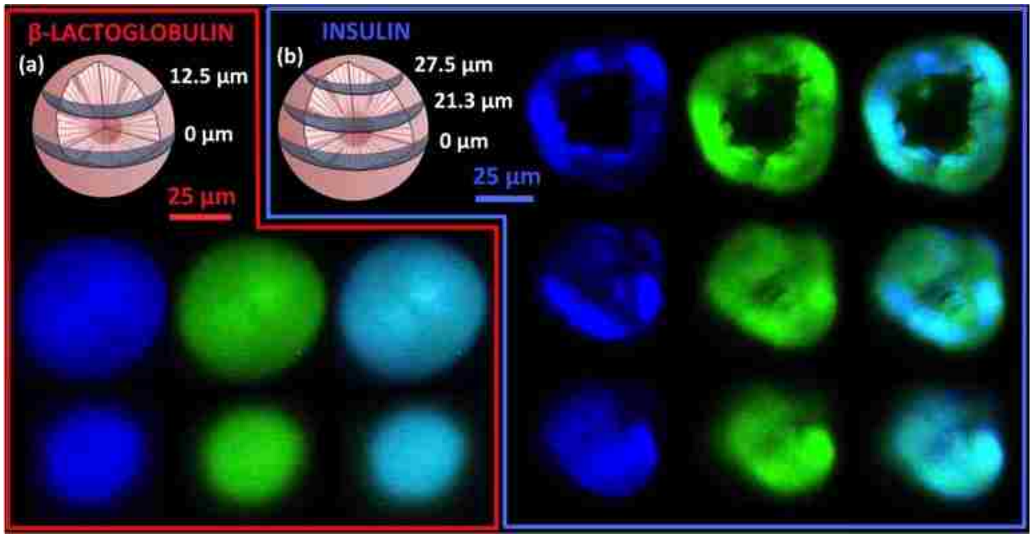

Figure 5.5. Various cross-sections for the spherulites. Cross-sections of a spherulite from β-LG from bovine milk (a) at 0 µm (top row) and 12.5 µm (bottom row) from the center with SHG (blue/left), TPEF (green/middle), and overlays (right); the scale bar is 25 µm. Cross- sections of a spherulite from bovine insulin (b) at 0 µm (top row), 21.3 µm (middle row), and 27.5 µm (bottom row) from the center with SHG (blue/left), TPEF (green/middle), and overlays (right); the scale bar is 25 µm. λ_{exc} was 910 nm in all cases.

These imaging techniques can also be used to sample various cross-sections of the spherulites, which provides information on their 3D-structure (Figure 5.5). A z-stack of cross-sections from an insulin spherulite was collected, from which four 3D animations were made. The results can be found in the supplementary material:[35] Visualization 1 and Visualization 2 (see publication online) show half of a 37 µm spherulite imaged with SHG and TPEF respectively, while Visualization 3 and Visualization 4 (see publication online) show the corresponding SHG and TPEF images of the entire spherulite. The amorphous core can easily be identified as a "cavity" in the structure. Finally, to further demonstrate the ability of these techniques to detect detailed features in the spherulite structures, some pressure was gently applied on the spherulites to induce cracks in them. The samples were then placed in the microscope and imaged with TPEF and SHG (Figure 5.6), with λ_{exc} at 910 nm. The SHG approach in particular was able to display the cracked features with high contrast. This is due to the high contrast for SHG demonstrated above, in combination with the fact that the microscope was used in back-scattering mode. The SHG signals are mainly produced in the forward direction (due to the conservation of momentum), which means that the signals need to be back-scattered to reach the detector. Consequently, enhanced scattering at cracks and defects make these features more pronounced. However, also the TPEF image exhibit enhanced signals close to some of the defects. This is also reasonable, as when the the excitation light is close to defect sites, on would expect to get the regular TPEF signal and potentially additional signals from light that travels in the direction of the defects that subsequently scatter it to the detector.

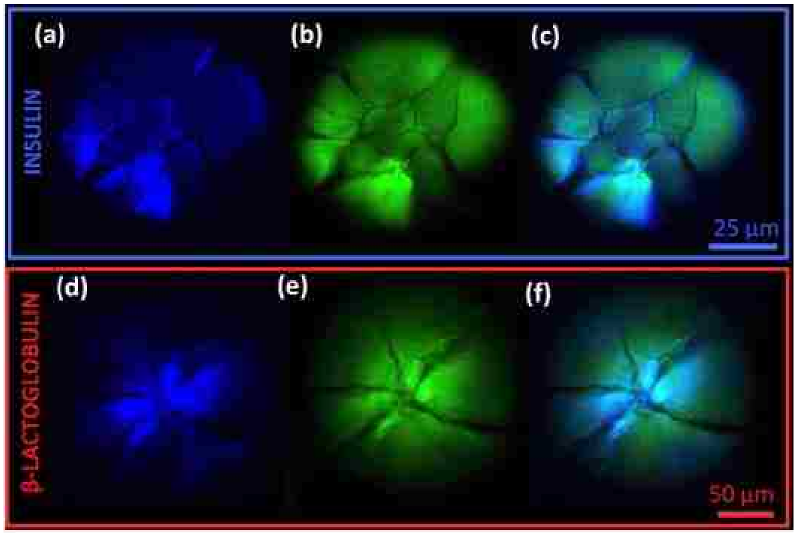

Figure 5.6. Imaging of cracked spherulites. SHG images (a, d - blue), TPEF images (b, e - green), and overlays (c,f) of cracked spherulites from bovine insulin (a-c) and β-LG from bovine milk (d-f); the scale bars are 25 µm (a-c) and 50 µm (d-f), and λ_{exc} was 910 nm. Note that the images of the insulin spherulite were not recorded at its center and, therefore, lack the amorphous core.

Lastly, REES in linear fluorescence has been readily demonstrated for these structures above. As far as we know, there are no conceptual reasons why REESs would not be possible to observe for TPEF as well. However, little research has been devoted to this and we are not aware of any studies of this kind. In order to investigate if REES may be found in the TPEF from our insulin spherulite structures, a range of different excitation wavelengths that would yield only TPEF and no SHG in both the detection arms were used. Thereafter, ratios of the average intensities of the images in the respective channels were formed. The results show that up to about 790 nm, the excitation wavelength has limited effect on the relative intensities in the two channels. Thereafter, the signal in the channel for the lower wavelength starts to decrease relative the one for longer wavelengths (Figure 5.7a). This is consistent with the REES phenomenon. However, since 790 nm is relatively close to the lower window boundary, the experiment was repeated with a second filter setup, with 460–500 nm and 520–560 nm windows (Figure 5.7b).

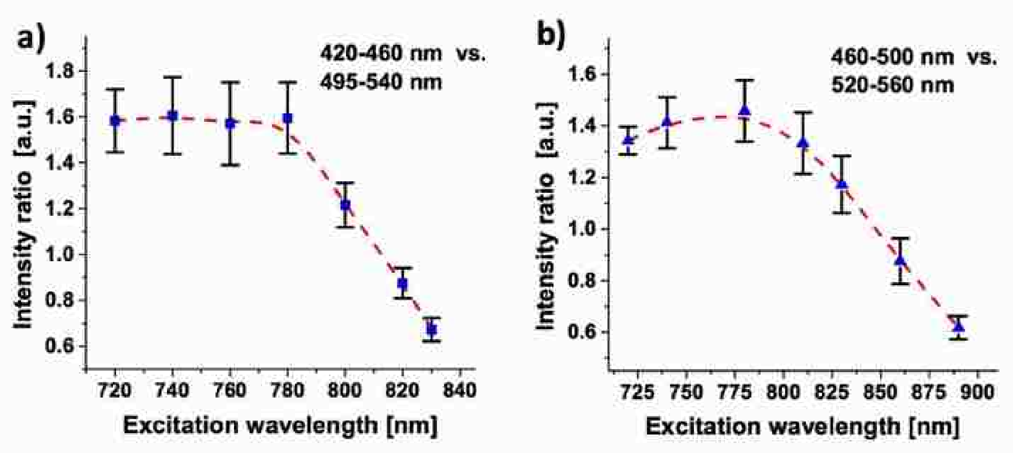

Figure 5.7. Excitation wavelength dependence in TPEF images. Ratio of average intensities for the insulin spherulites in the two detector channels. The bandpass filters windows compared are (a) 420–460 nm vs. 495–540 nm and (b) 460-500 nm vs. 520-560 nm. The error bars are St. Dev. from measurements on four spherulites and the excitation laser power was 80–400 mW, depending on the wavelength. The dashed red lines are splines intended as visual guides.

Again, the decline started at about 790 nm, which shows that it cannot be an effect from hyper Raman scattering. To conclusively determine that the observed behavior really is REES, it would be necessary to measure the MPA spectra as well as complete TPEF spectra for several excitation wavelengths. That is beyond the scope of this work, but we hypothesize that the obtained results are due to REES in TPEF. In such a case, a wavelength of 910 nm (the typical λ_{exc} in this work) is far out on the red-edge of the MPA. This would explain why this wavelength allowed very high excitation powers without photodegradation, while the higher MPA cross-sections for shorter wavelengths required lower excitation powers (e.g. <100 mW for $\lambda_{exc} \leq 800$ nm).

5.5 CONCLUSION

In this chapter, the intrinsic fluorescence of amyloid structures from insulin and β-LG was investigated in detail. Fibers and spherulites from both proteins exhibit enhanced fluorescence. However, only the β-LG structures develop an additional fluorescence decay pathway in the visible regime that could be readily detected with fluorescence spectroscopy. The origin of the new intrinsic fluorescence for β-LG is likely due to charge delocalization, while the origin of the enhanced signal for the insulin amyloid structures in confocal fluorescence microscopy is likely due to a transition from non-radiative to radiative pathways for the tyrosines in the peptide sequence. The ability to image amyloid spherulites with confocal fluorescence, TPEF, and SHG microscopy without the use of any probes or labels was also demonstrated. In particular, the nonlinear techniques provide images with excellent contrast for the fibrillar regions within the spherulites. This work provides a first demonstration of the virtue of multiphoton absorption in TPEF microscopy of amyloid structures. Additional contrast was obtained in the SHG images, thanks to a high SHG susceptibility exclusively for the ordered fibrillar regions. Also, it was demonstrated that these techniques can be used to obtain 3D-images of amyloid spherulites and display detailed information about their structure, including cracks and defects. Finally, we showed that the TPEF exhibits a spectral dependence on the excitation wavelength. We hypothesize that the REES phenomenon is responsible for this effect, since the observed behavior is consistent with this mechanism. As far as we know, REES in TPEF has not previously been reported, but additional investigations are needed at this time to confirm the existence and use of REES in nonlinear optical spectroscopy and imaging. Enhanced intrinsic fluorescence, strong MPA and intrinsic molecular ordering are a combination of features that likely distinguishes amyloids from most other structures in normal tissue.[32, 34, 36] A visualization strategy including all these features would be a helpful tool to selectively find and characterize amyloid deposits in, for example, brain tissue from patients with Alzheimer's disease, without the use of any labels or probes. As a result, non-destructive identification of amyloids in such tissues becomes possible without introduction of any contaminating agents. This subsequently allows chemical analyses of the identified amyloid structures by vibrational sum-frequency scattering spectroscopy,[35] coherent anti-stokes Raman scattering microscopy,[36, 57] and time-of-flight secondary ion mass spectrometry,[268] among other techniques. The fundamental optical properties of amyloids discussed and presented in this work are essential for continuing efforts with the goal of providing innovative strategies for the study of amyloid fiber structures. An improved pathway for making amyloid spherulites from $A\beta_{1-40}$ was recently developed.[171] As the presence of such structures has been demonstrated in the brain tissue of patients with Alzheimer's disease, they have a potential to become important in vitro models for Alzheimer research. This emphasizes the need in biomedical research for noninvasive techniques that can provide detailed information on amyloid spherulites.

Chapter 6. CONCLUSIONS AND OUTLOOK

6.1 CONCLUSIONS

Detailed studies of the molecular structure of protein fibers are challenging and most techniques need extensive sample preparation, require the use of external probes, lack chemical specificity, or do not provide the sensitivity necessary to detect subtle changes in the surface region of the fibers. Additional techniques are thus desired and it was the primary goal of this work to explore nonlinear optical properties of protein fiber structures and investigate how they can be used for structural characterization.

It was demonstrated that vibrational SFS spectroscopy can be applied to collagen fibers and that the spectra are dependent on the scattering angle. There are three potential explanations for this, all related to the detailed structure of the collagen fibers: (i) chiral groups, or groups organized in chiral arrangements, contribute more to the signal in the phase-matched direction and less at higher angles; (ii) the phase-shifts across the fiber diameter emphasizes different regions of the fiber at various angles, depending on how the groups add constructively or destructively to each other in the far field; and (iii) the orientation of the various groups relative to the symmetry axis of the fiber affects how strongly they contribute to the signal at various scattering angles (perfect alignment with the symmetry axis should yield large signals in the phase-matched direction, while other arrangements may require scattering angles away from this direction for effective signal production). One virtue of SFS is that signals at angles above 6° are highly reproducible for samples with a random organization of the collagen fibers, which is not the case for the signals in the phase-matched direction. This means that SFS can be used to study a broader range of samples, compared to e.g. SFG in reflection or transmission mode. One of the promising applications of SFS is monitoring the effect of surfactants on the fiber surface structure. Such investigations are very important, as treatments with surfactants are common steps in decellularization protocols and there are today no alternative approaches for real-time studies of the subtle changes such treatments may induce to the surface region of the collagen fibers. In this work, it was shown that monitoring the SFS signal at 22° provided specificity for the surface region, as changes to the ratios of various polarization combinations could be tracked during the initial phase of exposure to sodium dodecyl sulfate solutions. The main contributor to the changing ratios observed, was a signal decrease in the *sss* polarization combination. While achiral tensor elements of the hyperpolarizability, β_{eff}, can readily cross over and appear in susceptibility tensor elements probed by chiral polarization combinations, and vice versa, this is not the case for the *sss* polarization, which only probe achiral components of β_{eff}. This appears to be the case exclusively for this polarization combination, and the fact that *sss* only probes a small number of independent achiral tensor elements of β_{eff} ($\beta_{z'z'z'}$, $\beta_{x'x'z'}$, $\beta_{x'z'x'}$ and $\beta_{z'x'x'}$) may be the reason for why it is extra sensitive towards the fiber structure. The ability of SFS to detect the early changes to the structure of the surface region complements the capacity of other established techniques, such as SHG imaging or IR spectroscopy, which can be used to study the overall structure of the fibers. With further developments, some of which are discussed in the next chapter section, SFS may become a key technique for detailed investigations of protein fibers, which can help optimize strategies within biomaterials science, such as decellularization in tissue engineering.

The intrinsic linear and nonlinear optical properties of amyloid structures were also investigated in this work. It was demonstrated through REES that β-LG amyloid state, both as individual fibers and spherulites, develop a weak fluorescence at about 430 nm. Such luminescence was not readily observed for the insulin amyloids. Nevertheless, both β-LG and insulin spherulites could still be imaged with confocal fluorescence microscopy. However, imaging with nonlinear optical microscopy based on electronic transitions (SHG and TPEF) provided superior contrast for the crystalline fiber region in the structures, which may partly be due to enhanced multiphoton absorption that has previously been reported for insulin amyloid fibers. The REES phenomenon has been readily described in the scientific literature, but no previous observations of this kind has been reported for TPEF from biomolecules. In this work, the changing ratios of the TPEF signals in two distinct detection channels are a strong indication of REES, in particular as the ratios start changing approximately at the same excitation wavelength for two different filter settings. Detailed investigations of the REES phenomenon may inform on, for instance, the molecular packing and hydration state of the detected structures. Combined with the symmetry selection rules for SHG and the potential for polarization analyses, much information may be gained from these techniques when applied systematically to protein fiber structures with intrinsic luminescence.

6.2 FUTURE WORK

6.2.1 *Sum-Frequency Scattering in the C-H_x Stretching Region*

In this work, the scattering patterns of the amide I region has been the focus, primarily because it is more specific for proteins, as the line shape depends in the secondary structure. However, the collagen fibers also exhibit strong signals in the C-H_x stretching region. Additional efforts in this region are underway, but preliminary results are available and presented in Figure 6.1 and corresponding data for the amide I region is provided for comparison. First, as methylene groups are inherently achiral, they would need a preferred twist angle in order to produce chiral signals in the phase-matched direction. Depending on to what extent the groups have such a preferred twist angle, this might explain why the chiral *spp* polarization is less dominant in the phase-matched direction for the C-H_x stretches, compared to the amide I region.

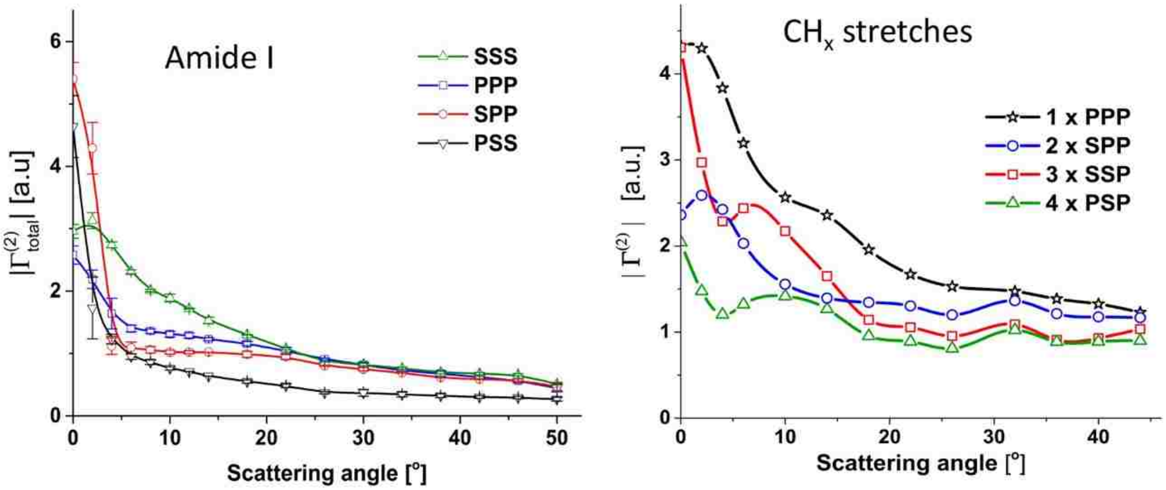

Figure 6.1. Scattering patterns for C-H$_x$ stretches. When compared with the amide I signals, the C-Hx stretches exhibit strong signals also at higher angles and clear maxima. The chiral signals are also less dominant in the phase-matched direction.

Second, as can be seen, the signal strengths remain much stronger at higher scattering angles for the C-H$_x$ stretches. The main reason for this is the organization of the C-Hx groups, especially the methylene groups, in the fibers. Based on previous SHG and XRD investigations, the average pitch angle (tilt relative the fiber axis) for the methylene groups is about 95° -100°. This is close to perpendicular relative the fiber axis, which means that opposite sides of the fiber will effectively cancel each other, yielding low β_{eff} in the phase-matched direction, especially for the achiral signals but also to some extent for the chiral signals (it depends on the geometry of the mixing beams). As the scattering angle is increased, a phase-shift across the fibers modulates the destructive and constructive interferences between the groups, which affects the magnitude of β_{eff} and explains the scattering patterns with clear maxima at various angles. This effect is weaker for the amide I groups, which have a pitch angle of ~46° and therefore have stronger components along the fiber axis. Schematics of the approximate differences in organization and symmetry for the amide I and C-H$_x$ groups are shown in Figure 6.2. Despite a lower specificity for proteins, it is possible that the stronger dependence on the specific detection angle for the signal strengths for the C-H_x could make this region even more sensitive towards changes in the fiber structure when subjected to various conditions. This needs to be established in future studies that confirm the patterns presented above and how they are affected during, for example, treatment with surfactants.

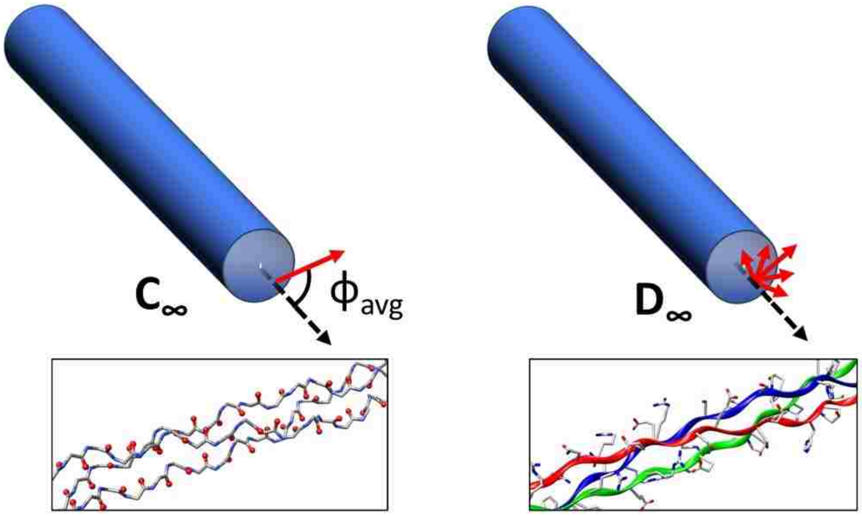

Figure 6.2. Organization of amide I and C-Hx groups in the fibers.

6.2.2 *Scattering Patterns for Aligned Collagen Fibers*

As mentioned in Chapter 4, the relative intensities of the various polarization combinations at scattering angles above 6° are highly reproducible, but not for samples with strong achiral signals in the phase-matched direction. This indicates that macroscopic orientations of the fibers affect the scattering patterns and/or the relative SFS signal strengths in various polarization combinations. As collagen fibers in tissue samples often are aligned, it will be important to sort out in detail how the direction and distribution of the fiber orientation affect the scattering patterns. Systematic studies of collagen in, for example, rat tail tendons are needed, where the samples are rotated at various angles while the signal strengths for different polarization combinations are monitored at various angles. This will require a slight modification of the sample cell used in this work: instead of hemi-cylindrical prisms, hemi-spherical prisms would be needed, which can be placed in a sample holder that can rotate around the center axis of the prism (for example, mounts that are commonly used for half-wave plates or wire-grid polarizers would be appropriate).

6.2.3 *Monitoring of Tissue Collagen During Decellularization*

When the effect of macroscopic fiber orientations on the scattering patterns have been established, the next step would be to monitor the signals from collagen fibers in real tissue samples during treatment with surfactants and other chemicals often used in decellularization protocols. A good starting point for this would be rat tail tendon samples, which were also suggested as target samples in the previous section. Another reason why this is a good starting sample is that rat tail tendon primarily consists of type I collagen, which has been the focus throughout this work, and the material source is often readily available in biomaterial research settings. However, other collagen types are also of interest. A natural next step would be to study rat trachea cartilage, which include more type II collagen. It would be interesting to compare the SFS responses and scattering patterns for these different types of collagen fibers, and investigate if any correlations can be made with their resilience towards various decellularization protocols. This could potentially provide new insights into how successful biological scaffolds for tissue engineering may be achieved.

6.2.4 *Detection of Surfactants in Sum-Frequency Scattering*

In this work, only signals from the collagen fibers have been detected and investigated. However, surfactants that interact with the fibers may also adopt preferred orientations at the fiber surface. While surfactants free in solution would be impossible to detect, the induced ordering from the collagen fiber interaction could induce them to produce SFS signatures at certain scattering angles. This would be exciting, as detection of such signals would be a direct observation of the fiber/molecule interactions. Polarization analyses, detection of the scattering patterns, and the development of theoretical models for the expected signals could provide much detailed information about the interaction, such as the relative orientation of the molecular groups at the fiber surface and potential reorganization of the peptides and side-chains at the surface of the collagen fibers. The effect of other additives could then be studied that may allow development of strategies for selective preservation of the collagen fiber structures in the ECM of tissues during decellularization, while cellular material is removed. Efforts to detect deuterated SDS in the SFS experiments have been made in this work, but so far without success. There are several challenges with such studies: (i) the optimal detection angle is not known (which may be different from the surface specific angle in the amide I region, due to the difference in IR wavenumber); (ii) the signals may be relatively weak, if the distribution width for the preferred orientation of the surfactants at the fiber surface is broad; (iii) the optimal surfactant concentration is not known; and (iv) it is non-trivial to optimize the alignment of the mixing beams and direct the signal to the detector if the signals are weak, and appropriate samples with strong resonant or nonresonant signals in the C-D_x stretching region that could be used for alignment are not currently available. However, if these issues can be resolved, the outlook to directly detect of fiber/molecule interactions is good. Such capabilities would not only be useful for the optimization of decellularization protocols, but could also be important for fundamental research that concerns any type of interaction between collagen fibers and other biomolecules, such as lipids or proteins.

6.2.5 *Elliptical Visible/nIR Beams Yield Destructive Interference*

Finally, an unexpected phenomenon of unknown origin will be discussed. While initially probing the signal strengths presented in Figure 4.9d, it was noted that the signal at 0° and 180° polarization directions for the visible/nIR and the IR were different (the signal at 180° vanished). Of course, this is not expected, as the two polarizations should yield the same signal. The reason for the observation was determined to be a small ellipticity of the visible/nIR at 180°, due to a half-wave plate optimized for 780 nm, rather than the 791 nm wavelength of the visible/nIR used in the experiments. The results in Figure 4.9 were repeated with a setup that gave clean polarization states without any ellipticity, and the anomaly disappeared. However, it is surprising that the elliptical state of the visible/nIR gave destructive interference, since the semi-minor and semi-major axes of elliptical light are phase-shifted by 90°, which cannot yield destructive interference on its own – other phenomena must thus contribute to this observation. Figure 6.3 shows an example of the effective the signal cancellation when a certain polarization combination that utilizes elliptical light of the visible/nIR, compared to the signal strengths using visible/nIR light polarized in the directions of the semi-minor and semi-major axes with corresponding intensities.

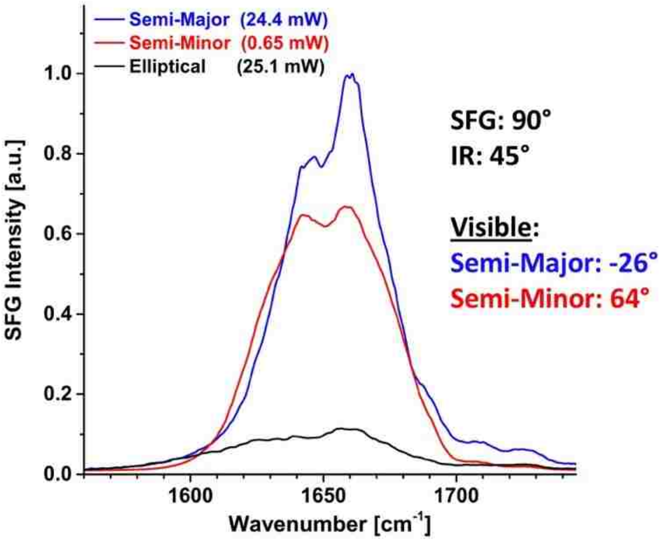

Figure 6.3. Signal cancellation with elliptical visible/nIR. In this example, the SFG was polarized at 90°, and the IR at 45° (relative the vertical direction). The elliptical visible/nIR that most effectively gave a cancelled response (black line) had 24.4 mW and 0.68 mW in the directions of the semi-major and semi-minor axes, which were polarized in the directions -26° and -64°. The signals with comparable power for the visible/nIR plane-polarized in these directions (blue and red lines) are shown.

At present, the details of the phenomena contributing to this observation are unknown. It is tempting to propose that the pitch angles of the molecular groups in the fiber structure are involved in some way. However, such explanations would require contributions of additional phenomena, as the orientation of molecules do not tune the phase of the signal response, but rather flip the sign of the nonlinear susceptibility. As the semi-minor and semi-major axes have perpendicular polarization directions, it is possible that the two components probe different subsets of the molecular groups in the structure. Slightly different positions of those groups throughout the structure, together with a slightly different peak position, could lead to a phase difference between the signal contributions from these subsets. Normally, this phase difference is probably too small to yield efficient signal cancelation, but with the additional 90° phase shift of the elliptical light, the effect could become substantial. If this hypothesis is correct, it implies that information about the detailed molecular structure of the collagen fibers, beyond traditional polarization analysis with pure *s* and *p* polarization states, may be accessible by systematically investigating the interferences at various directions and magnitudes for the semi-minor and semi-major axes of the elliptical light. Such investigations are beyond the work presented in this dissertation, but the potential is intriguing, given the high resolution provided by interferometric techniques. For example, spectroscopic ellipsometry can provide information about the layered structure of thin films down to less than one Å. In the case of elliptical SFG, the big challenge would be how to translate the data into useful structural information, but at least semi-quantitative statements about the relative position and direction of various groups in the structure should be possible.

BIBLIOGRAPHY

1. Muiznieks, L. D.; Keeley, F. W., Molecular assembly and mechanical properties of the extracellular matrix: A fibrous protein perspective. *Biochimica Et Biophysica Acta-Molecular Basis of Disease* **2013,** *1832* (7), 866-875.

2. Cooper, G. M.; Hausman, R. E., *The cell: A molecular approach*. 7 ed.; Sinauer Associates: Sunderland, 2015.

3. Burridge, K.; Fath, K.; Kelly, T.; Nuckolls, G.; Turner, C., Focal adhesions - transmembrane junctions between the extracellular-matrix and the cytoskeleton. *Annual Review of Cell Biology* **1988,** *4*, 487-525.

4. Murugan, R.; Ramakrishna, S., Design strategies of tissue engineering scaffolds with controlled fiber orientation. *Tissue Engineering* **2007,** *13* (8), 1845-1866.

5. Discher, D. E.; Janmey, P.; Wang, Y. L., Tissue cells feel and respond to the stiffness of their substrate. *Science* **2005,** *310* (5751), 1139-1143.

6. Hardy, J.; Selkoe, D. J., Medicine - The amyloid hypothesis of Alzheimer's disease: Progress and problems on the road to therapeutics. *Science* **2002,** *297* (5580), 353-356.

7. Eisenberg, D.; Jucker, M., The Amyloid State of Proteins in Human Diseases. *Cell* **2012,** *148* (6), 1188-1203.

8. Selkoe, D. J.; Schenk, D., Alzheimer's disease: Molecular understanding predicts amyloid-based therapeutics. *Annual Review of Pharmacology and Toxicology* **2003,** *43*, 545-584.

9. Apte, J. S.; Collier, G.; Latour, R. A.; Gamble, L. J.; Castner, D. G., XPS and ToF-SIMS Investigation of alpha-Helical and beta-Strand Peptide Adsorption onto SAMs. *Langmuir* **2010,** *26* (5), 3423-3432.

10. Castner, D. G., Biomedical surface analysis: Evolution and future directions. *Biointerphases* **2017,** *12* (2), 11.

11. Belu, A. M.; Graham, D. J.; Castner, D. G., Time-of-flight secondary ion mass spectrometry: techniques and applications for the characterization of biomaterial surfaces. *Biomaterials* **2003,** *24* (21), 3635-3653.

12. White, L. J.; Taylor, A. J.; Faulk, D. M.; Keane, T. J.; Saldin, L. T.; Reing, J. E.; Swinehart, I. T.; Turner, N. J.; Ratner, B. D.; Badylak, S. F., The impact of detergents on the tissue decellularization process: A ToF-SIMS study. *Acta Biomaterialia* **2017,** *50*, 207-219.

13. Rodahl, M.; Hook, F.; Fredriksson, C.; Keller, C. A.; Krozer, A.; Brzezinski, P.; Voinova, M.; Kasemo, B., Simultaneous frequency and dissipation factor QCM measurements of biomolecular adsorption and cell adhesion. *Faraday Discussions* **1997,** *107*, 229-246.

14. Reimhult, E.; Hook, F.; Kasemo, B., Intact vesicle adsorption and supported biomembrane formation from vesicles in solution: Influence of surface chemistry, vesicle size, temperature, and osmotic pressure. *Langmuir* **2003,** *19* (5), 1681-1691.

15. Keller, C. A.; Kasemo, B., Surface specific kinetics of lipid vesicle adsorption measured with a quartz crystal microbalance. *Biophysical Journal* **1998,** *75* (3), 1397-1402.

16. Liedberg, B.; Nylander, C.; Lundstrom, I., Surface-plasmon resonance for gas-detection and biosensing. *Sensors and Actuators* **1983,** *4* (2), 299-304.

17. Besenicar, M.; Macek, P.; Lakey, J. H.; Anderluh, G., Surface plasmon resonance in protein-membrane interactions. *Chemistry and Physics of Lipids* **2006,** *141* (1-2), 169-178.

18. Barth, A.; Zscherp, C., What vibrations tell us about proteins. *Quarterly Reviews of Biophysics* **2002,** *35* (4), 369-430.

19. Shen, Y. R., *The principles of nonlinear optics*. John Wiley and Sons Ltd: New York, 2002.

20. Boyd, R. W., *Nonlinear Optics*. 3 ed.; Academic Press: Oxford, 2008.

21. Shen, Y. R., Surfaces probed by nonlinear optics. *Surface Science* **1994,** *299* (1-3), 551-562.

22. Yakovlev, V. V., *Biochemical Applications of Nonlinear Optical Spectroscopy*. CRC Press: Boca Raton, 2009.

23. Simpson, G. J., *Nonlinear optical polarization analysis in chemistry and biology*. Cambridge University Press: Cambridge, 2017.

24. Risselada, H. J.; Marrink, S. J., Curvature effects on lipid packing and dynamics in liposomes revealed by coarse grained molecular dynamics simulations. *Physical Chemistry Chemical Physics* **2009,** *11* (12), 2056-2067.

25. Vertegel, A. A.; Siegel, R. W.; Dordick, J. S., Silica nanoparticle size influences the structure and enzymatic activity of adsorbed lysozyme. *Langmuir* **2004,** *20* (16), 6800-6807.

26. Grainger, D. W.; Castner, D. G., Nanobiomaterials and nanoanalysis: Opportunities for improving the science to benefit biomedical technologies. *Advanced Materials* **2008,** *20* (5), 867-877.

27. Eisenthal, K. B., Second harmonic spectroscopy of aqueous nano- and microparticle interfaces. *Chemical Reviews* **2006,** *106* (4), 1462-1477.

28. Roke, S.; Gonella, G., Nonlinear Light Scattering and Spectroscopy of Particles and Droplets in Liquids. In *Annual Review of Physical Chemistry, Vol 63*, Johnson, M. A.; Martinez, T. J., Eds. 2012; Vol. 63, pp 353-378.

29. Wang, H.; Yan, E. C. Y.; Borguet, E.; Eisenthal, K. B., Second harmonic generation from the surface of centrosymmetric particles in bulk solution. *Chemical Physics Letters* **1996,** *259* (1-2), 15-20.

30. Roke, S.; Roeterdink, W. G.; Wijnhoven, J.; Petukhov, A. V.; Kleyn, A. W.; Bonn, M., Vibrational sum frequency scattering from a submicron suspension. *Physical Review Letters* **2003,** *91* (25).

31. Zipfel, W. R.; Williams, R. M.; Webb, W. W., Nonlinear magic: multiphoton microscopy in the biosciences. *Nature Biotechnology* **2003,** *21* (11), 1368-1376.

32. Zipfel, W. R.; Williams, R. M.; Christie, R.; Nikitin, A. Y.; Hyman, B. T.; Webb, W. W., Live tissue intrinsic emission microscopy using multiphoton-excited native fluorescence and second harmonic generation. *Proceedings of the National Academy of Sciences of the United States of America* **2003,** *100* (12), 7075-7080.

33. Liu, H. W.; Liu, Y. C.; Wang, P.; Zhang, X. B., Molecular engineering of two-photon fluorescent probes for bioimaging applications. *Methods and Applications in Fluorescence* **2017,** *5* (1), 24.

34. Kwan, A. C.; Duff, K.; Gouras, G. K.; Webb, W. W., Optical visualization of Alzheimer's pathology via multiphoton-excited intrinsic fluorescence and second harmonic generation. *Optics Express* **2009,** *17* (5), 3679-3689.

35. Johansson, P. K.; Koelsch, P., Label-free imaging of amyloids using their intrinsic linear and nonlinear optical properties. *Biomedical Optics Express* **2017,** *8* (2), 743-756.

36. Lee, J. H.; Kim, D. H.; Song, W. K.; Oh, M. K.; Ko, D. K., Label-free imaging and quantitative chemical analysis of Alzheimer's disease brain samples with multimodal multiphoton nonlinear optical microspectroscopy. *Journal of Biomedical Optics* **2015,** *20* (5), 7.

37. Zoumi, A.; Yeh, A.; Tromberg, B. J., Imaging cells and extracellular matrix in vivo by using second-harmonic generation and two-photon excited fluorescence. *Proceedings of the National Academy of Sciences of the United States of America* **2002,** *99* (17), 11014-11019.

38. Ustione, A.; Piston, D. W., A simple introduction to multiphoton microscopy. *Journal of Microscopy* **2011,** *243* (3), 221-226.

39. Gauderon, R.; Lukins, P. B.; Sheppard, C. J. R., Optimization of second-harmonic generation microscopy. *Micron* **2001,** *32* (7), 691-700.

40. Moad, A. J.; Simpson, G. J., A unified treatment of selection rules and symmetry relations for sum-frequency and second harmonic spectroscopies. *Journal of Physical Chemistry B* **2004,** *108* (11), 3548-3562.

41. Chen, W. L.; Li, T. H.; Su, P. J.; Chou, C. K.; Fwu, P. T.; Lin, S. J.; Kim, D.; So, P. T. C.; Dong, C. Y., Second harmonic generation chi tensor microscopy for tissue imaging. *Applied Physics Letters* **2009,** *94* (18), 3.

42. Chen, X. Y.; Nadiarynkh, O.; Plotnikov, S.; Campagnola, P. J., Second harmonic generation microscopy for quantitative analysis of collagen fibrillar structure. *Nature Protocols* **2012,** *7* (4), 654-669.

43. Pavone, F. S.; Campagnola, P. J., *Second Harmonic Generation Imaging*. CRC Press: Boca Raton, 2014.

44. Williams, R. M.; Zipfel, W. R.; Webb, W. W., Interpreting second-harmonic generation images of collagen I fibrils. *Biophysical Journal* **2005,** *88* (2), 1377-1386.

45. Stoller, P.; Kim, B. M.; Rubenchik, A. M.; Reiser, K. M.; Da Silva, L. B., Polarization-dependent optical second-harmonic imaging of a rat-tail tendon. *Journal of Biomedical Optics* **2002,** *7* (2), 205-214.

46. Tuer, A. E.; Krouglov, S.; Prent, N.; Cisek, R.; Sandkuijl, D.; Yasufuku, K.; Wilson, B. C.; Barzda, V., Nonlinear Optical Properties of Type I Collagen Fibers Studied by Polarization Dependent Second Harmonic Generation Microscopy. *Journal of Physical Chemistry B* **2011,** *115* (44), 12759-12769.

47. Jiang, X. S.; Zhong, J. Z.; Liu, Y. C.; Yu, H. B.; Zhuo, S. M.; Chen, J. X., Two-Photon Fluorescence and Second-Harmonic Generation Imaging of Collagen in Human Tissue Based on Multiphoton Microscopy. *Scanning* **2011,** *33* (1), 53-56.

48. Kumar, R.; Gronhaug, K. M.; Romijn, E. I.; Finnoy, A.; Davies, C. L.; Drogset, J. O.; Lilledahl, M. B., Polarization second harmonic generation microscopy provides quantitative enhanced molecular specificity for tissue diagnostics. *Journal of Biophotonics* **2015,** *8* (9), 730-739.

49. Su, P. J.; Chen, W. L.; Chen, Y. F.; Dong, C. Y., Determination of Collagen Nanostructure from Second-Order Susceptibility Tensor Analysis. *Biophysical Journal* **2011,** *100* (8), 2053-2062.

50. Cheng, J. X.; Xie, X. S., Coherent anti-Stokes Raman scattering microscopy: Instrumentation, theory, and applications. *Journal of Physical Chemistry B* **2004,** *108* (3), 827-840.

51. Rodriguez, L. G.; Lockett, S. J.; Holtom, G. R., Coherent anti-stokes Raman scattering microscopy: A biological review. *Cytometry Part A* **2006,** *69A* (8), 779-791.

52. Evans, C. L.; Xie, X. S., Coherent Anti-Stokes Raman Scattering Microscopy: Chemical Imaging for Biology and Medicine. In *Annual Review of Analytical Chemistry*, 2008; Vol. 1, pp 883-909.

53. Volkmer, A., Vibrational imaging and microspectroscopies based on coherent anti-Stokes Raman scattering microscopy. *Journal of Physics D-Applied Physics* **2005,** *38* (5), R59-R81.

54. Liu, Y. X.; Lee, Y. J.; Cicerone, M. T., Broadband CARS spectral phase retrieval using a time-domain Kramers-Kronig transform. *Optics Letters* **2009,** *34* (9), 1363-1365.

55. Camp, C. H.; Lee, Y. J.; Heddleston, J. M.; Hartshorn, C. M.; Walker, A. R. H.; Rich, J. N.; Lathia, J. D.; Cicerone, M. T., High-speed coherent Raman fingerprint imaging of biological tissues. *Nature Photonics* **2014,** *8* (8), 627-634.

56. Fu, Y.; Huff, T. B.; Wang, H. W.; Wang, H. F.; Cheng, J. X., Ex vivo and in vivo imaging of myelin fibers in mouse brain by coherent anti-Stokes Raman scattering microscopy. *Optics Express* **2008,** *16* (24), 19396-19409.

57. Kiskis, J.; Fink, H.; Nyberg, L.; Thyr, J.; Li, J. Y.; Enejder, A., Plaque-associated lipids in Alzheimer's diseased brain tissue visualized by nonlinear microscopy. *Scientific Reports* **2015,** *5*.

58. Freudiger, C. W.; Min, W.; Saar, B. G.; Lu, S.; Holtom, G. R.; He, C. W.; Tsai, J. C.; Kang, J. X.; Xie, X. S., Label-Free Biomedical Imaging with High Sensitivity by Stimulated Raman Scattering Microscopy. *Science* **2008,** *322* (5909), 1857-1861.

59. Tipping, W. J.; Lee, M.; Serrels, A.; Brunton, V. G.; Hulme, A. N., Stimulated Raman scattering microscopy: an emerging tool for drug discovery. *Chemical Society Reviews* **2016,** *45* (8), 2075-2089.

60. Min, W.; Freudiger, C. W.; Lu, S. J.; Xie, X. S., Coherent Nonlinear Optical Imaging: Beyond Fluorescence Microscopy. In *Annual Review of Physical Chemistry, Vol 62*, Leone, S. R.; Cremer, P. S.; Groves, J. T.; Johnson, M. A., Eds. 2011; Vol. 62, pp 507-530.

61. Duboisset, J.; Berto, P.; Gasecka, P.; Bioud, F. Z.; Ferrand, P.; Rigneault, H.; Brasselet, S., Molecular Orientational Order Probed by Coherent Anti-Stokes Raman Scattering (CARS) and Stimulated Raman Scattering (SRS) Microscopy: A Spectral Comparative Study. *Journal of Physical Chemistry B* **2015,** *119* (7), 3242-3249.

62. Hofer, M.; Balla, N. K.; Brasselet, S., High-speed polarization-resolved coherent Raman scattering imaging. *Optica* **2017,** *4* (7), 795-801.

63. Bioud, F. Z.; Gasecka, P.; Ferrand, P.; Rigneault, H.; Duboisset, J.; Brasselet, S., Structure of molecular packing probed by polarization-resolved nonlinear four-wave mixing and coherent anti-Stokes Raman-scattering microscopy. *Physical Review A* **2014,** *89* (1), 10.

64. Fu, D.; Holtom, G.; Freudiger, C.; Zhang, X.; Xie, X. S., Hyperspectral Imaging with Stimulated Raman Scattering by Chirped Femtosecond Lasers. *Journal of Physical Chemistry B* **2013,** *117* (16), 4634-4640.

65. Hunt, J. H.; Guyotsionnest, P.; Shen, Y. R., Observation of C-H stretch vibrations of monolayers of molecules optical sum-frequency generation. *Chemical Physics Letters* **1987,** *133* (3), 189-192.

66. Guyotsionnest, P.; Hunt, J. H.; Shen, Y. R., Sum-frequency vibrational spectroscopy of a Langmuir film - study of molecular-orientation of a two-dimensional system. *Physical Review Letters* **1987,** *59* (14), 1597-1600.

67. Zhu, X. D.; Suhr, H.; Shen, Y. R., Surface vibrational spectroscopy by infrared-visible sum frequency generation. *Physical Review B* **1987,** *35* (6), 3047-3050.

68. Vidal, F.; Tadjeddine, A., Sum-frequency generation spectroscopy of interfaces. *Reports on Progress in Physics* **2005,** *68* (5), 1095-1127.

69. Wang, H. F.; Velarde, L.; Gan, W.; Fu, L., Quantitative Sum-Frequency Generation Vibrational Spectroscopy of Molecular Surfaces and Interfaces: Lineshape, Polarization, and Orientation. In *Annual Review of Physical Chemistry, Vol 66*, Johnson, M. A.; Martinez, T. J., Eds. 2015; Vol. 66, pp 189-216.

70. Haupert, L. M.; Simpson, G. J., Chirality in Nonlinear Optics. In *Annual Review of Physical Chemistry*, 2009; Vol. 60, pp 345-365.

71. Fu, L.; Liu, J.; Yan, E. C. Y., Chiral Sum Frequency Generation Spectroscopy for Characterizing Protein Secondary Structures at Interfaces. *Journal of the American Chemical Society* **2011,** *133* (21), 8094-8097.

72. Fu, L.; Wang, Z. G.; Yan, E. C. Y., Chiral Vibrational Structures of Proteins at Interfaces Probed by Sum Frequency Generation Spectroscopy. *International Journal of Molecular Sciences* **2011,** *12* (12), 9404-9425.

73. Yan, E. C. Y.; Wang, Z. G.; Fu, L., Proteins at Interfaces Probed by Chiral Vibrational Sum Frequency Generation Spectroscopy. *Journal of Physical Chemistry B* **2015,** *119* (7), 2769-2785.

74. Wang, J.; Chen, X. Y.; Clarke, M. L.; Chen, Z., Detection of chiral sum frequency generation vibrational spectra of proteins and peptides at interfaces in situ. *Proceedings of the National Academy of Sciences of the United States of America* **2005,** *102* (14), 4978-4983.

75. Roeters, S. J.; van Dijk, C. N.; Torres-Knoop, A.; Backus, E. H. G.; Campen, R. K.; Bonn, M.; Woutersen, S., Determining In Situ Protein Conformation and Orientation from the Amide-I Sum-Frequency Generation Spectrum: Theory and Experiment. *Journal of Physical Chemistry A* **2013,** *117* (29), 6311-6322.

76. Nguyen, K. T.; King, J. T.; Chen, Z., Orientation Determination of Interfacial beta-Sheet Structures in Situ. *Journal of Physical Chemistry B* **2010,** *114* (25), 8291-8300.

77. Nguyen, K. T.; Le Clair, S. V.; Ye, S. J.; Chen, Z., Orientation Determination of Protein Helical Secondary Structures Using Linear and Nonlinear Vibrational Spectroscopy. *Journal of Physical Chemistry B* **2009,** *113* (36), 12169-12180.

78. Harrison, E. T.; Weidner, T.; Castner, D. G.; Interlandi, G., Predicting the orientation of protein G B1 on hydrophobic surfaces using Monte Carlo simulations. *Biointerphases* **2017,** *12* (2).

79. Schmuser, L.; Roeters, S.; Lutz, H.; Woutersen, S.; Bonn, M.; Weidner, T., Determination of Absolute Orientation of Protein alpha-Helices at Interfaces Using Phase-Resolved Sum Frequency Generation Spectroscopy. *Journal of Physical Chemistry Letters* **2017,** *8* (13), 3101-3105.

80. Kim, J.; Chou, K. C.; Somorjai, G. A., Structure and dynamics of acetonitrile at the air/liquid interface of binary solutions studied by infrared-visible sum frequency generation. *Journal of Physical Chemistry B* **2003,** *107* (7), 1592-1596.

81. Kim, J.; Somorjai, G. A., Molecular packing of lysozyme, fibrinogen, and bovine serum albumin on hydrophilic and hydrophobic surfaces studied by infrared-visible sum frequency generation and fluorescence microscopy. *Journal of the American Chemical Society* **2003,** *125* (10), 3150-3158.

82. Wang, J.; Paszti, Z.; Even, M. A.; Chen, Z., Measuring polymer surface ordering differences in air and water by sum frequency generation vibrational spectroscopy. *Journal of the American Chemical Society* **2002,** *124* (24), 7016-7023.

83. Wang, J.; Chen, C. Y.; Buck, S. M.; Chen, Z., Molecular chemical structure on poly(methyl methacrylate) (PMMA) surface studied by sum frequency generation (SFG) vibrational spectroscopy. *Journal of Physical Chemistry B* **2001,** *105* (48), 12118-12125.

84. Weidner, T.; Breen, N. F.; Li, K.; Drobny, G. P.; Castner, D. G., Sum frequency generation and solid-state NMR study of the structure, orientation, and dynamics of polystyrene-adsorbed peptides. *Proceedings of the National Academy of Sciences of the United States of America* **2010,** *107* (30), 13288-13293.

85. Liu, Y. W.; Ogorzalek, T. L.; Yang, P.; Schroeder, M. M.; Marsh, E. N. G.; Chen, Z., Molecular Orientation of Enzymes Attached to Surfaces through Defined Chemical Linkages at the Solid-Liquid Interface. *Journal of the American Chemical Society* **2013,** *135* (34), 12660-12669.

86. Badieyan, S.; Wang, Q. M.; Zou, X. Q.; Li, Y. X.; Herron, M.; Abbott, N. L.; Chen, Z.; Marsh, E. N. G., Engineered Surface-Immobilized Enzyme that Retains High Levels of Catalytic Activity in Air. *Journal of the American Chemical Society* **2017,** *139* (8), 2872-2875.

87. Shen, L.; Cheng, K. C. K.; Schroeder, M.; Yang, P.; Marsh, E. N. G.; Lahann, J.; Chen, Z., Immobilization of enzyme on a polymer surface. *Surface Science* **2016,** *648*, 53-59.

88. Shen, L.; Ulrich, N. W.; Mello, C. M.; Chen, Z., Determination of conformation and orientation of immobilized peptides and proteins at buried interfaces. *Chemical Physics Letters* **2015,** *619*, 247-255.

89. Weidner, T.; Castner, D. G., SFG analysis of surface bound proteins: a route towards structure determination. *Physical Chemistry Chemical Physics* **2013,** *15* (30), 12516-12524.

90. Nihonyanagi, S.; Yamaguchi, S.; Tahara, T., Direct evidence for orientational flip-flop of water molecules at charged interfaces: A heterodyne-detected vibrational sum frequency generation study. *Journal of Chemical Physics* **2009,** *130* (20), 5.

91. Mondal, J. A.; Nihonyanagi, S.; Yamaguchi, S.; Tahara, T., Structure and Orientation of Water at Charged Lipid Monolayer/Water Interfaces Probed by Heterodyne-Detected Vibrational Sum Frequency Generation Spectroscopy. *Journal of the American Chemical Society* **2010,** *132* (31), 10656-10657.

92. Stiopkin, I. V.; Jayathilake, H. D.; Bordenyuk, A. N.; Benderskii, A. V., Heterodyne-detected vibrational sum frequency generation spectroscopy. *Journal of the American Chemical Society* **2008,** *130* (7), 2271-2275.

93. Wang, J.; Buck, S. M.; Chen, Z., Sum frequency generation vibrational spectroscopy studies on protein adsorption. *Journal of Physical Chemistry B* **2002,** *106* (44), 11666-11672.

94. Wang, J.; Even, M. A.; Chen, X. Y.; Schmaier, A. H.; Waite, J. H.; Chen, Z., Detection of amide I signals of interfacial proteins in situ using SFG. *Journal of the American Chemical Society* **2003,** *125* (33), 9914-9915.

95. Chen, X. Y.; Wang, J.; Sniadecki, J. J.; Even, M. A.; Chen, Z., Probing alpha-helical and beta-sheet structures of peptides at solid/liquid interfaces with SFG. *Langmuir* **2005,** *21* (7), 2662-2664.

96. Wang, J.; Clarke, M. L.; Chen, X. Y.; Even, M. A.; Johnson, W. C.; Chen, Z., Molecular studies on protein conformations at polymer/liquid interfaces using sum frequency generation vibrational spectroscopy. *Surface Science* **2005,** *587* (1-2), 1-11.

97. Chen, X. Y.; Wang, J.; Boughton, A. P.; Kristalyn, C. B.; Chen, Z., Multiple orientation of melittin inside a single lipid bilayer determined by combined vibrational spectroscopic studies. *Journal of the American Chemical Society* **2007,** *129* (5), 1420-1427.

98. Le Clair, S. V.; Nguyen, K.; Chen, Z., Sum Frequency Generation Studies on Bioadhesion: Elucidating the Molecular Structure of Proteins at Interfaces. *Journal of Adhesion* **2009,** *85* (8), 484-511.

99. Nguyen, K. T.; Soong, R.; Im, S. C.; Waskell, L.; Ramamoorthy, A.; Chen, Z., Probing the Spontaneous Membrane Insertion of a Tail-Anchored Membrane Protein by Sum Frequency Generation Spectroscopy. *Journal of the American Chemical Society* **2010,** *132* (43), 15112-15115.

100. Ye, S. J.; Nguyen, K. T.; Boughton, A. P.; Mello, C. M.; Chen, Z., Orientation Difference of Chemically Immobilized and Physically Adsorbed Biological Molecules on Polymers Detected at the Solid/Liquid Interfaces in Situ. *Langmuir* **2010,** *26* (9), 6471-6477.

101. Liu, Y. W.; Jasensky, J.; Chen, Z., Molecular Interactions of Proteins and Peptides at Interfaces Studied by Sum Frequency Generation Vibrational Spectroscopy. *Langmuir* **2012,** *28* (4), 2113-2121.

102. Weidner, T.; Dubey, M.; Breen, N. F.; Ash, J.; Baio, J. E.; Jaye, C.; Fischer, D. A.; Drobny, G. P.; Castner, D. G., Direct Observation of Phenylalanine Orientations in Statherin Bound to Hydroxyapatite Surfaces. *Journal of the American Chemical Society* **2012,** *134* (21), 8750-8753.

103. Fu, L.; Wang, Z. G.; Psciuk, B. T.; Xiao, D. Q.; Batista, V. S.; Yan, E. C. Y., Characterization of Parallel beta-Sheets at Interfaces by Chiral Sum Frequency Generation Spectroscopy. *Journal of Physical Chemistry Letters* **2015,** *6* (8), 1310-1315.

104. Liu, W.; Li, S. H.; Wang, Z. G.; Yan, E. C. Y.; Leblanc, R. M., Characterization of Surface-Active Biofilm Protein BslA in Self-Assembling Langmuir Monolayer at the Air-Water Interface. *Langmuir* **2017,** *33* (30), 7548-7555.

105. VandenAkker, C. C.; Schleeger, M.; Bruinen, A. L.; Deckert-Gaudig, T.; Velikov, K. P.; Heeren, R. M. A.; Deckert, V.; Bonn, M.; Koenderink, G. H., Multimodal Spectroscopic Study of Amyloid Fibril Polymorphism. *Journal of Physical Chemistry B* **2016,** *120* (34), 8809-8817.

106. vandenAkker, C. C.; Engel, M. F. M.; Velikov, K. P.; Bonn, M.; Koenderink, G. H., Morphology and Persistence Length of Amyloid Fibrils Are Correlated to Peptide Molecular Structure. *Journal of the American Chemical Society* **2011,** *133* (45), 18030-18033.

107. Liu, J.; Conboy, J. C., Phase transition of a single lipid bilayer measured by sum-frequency vibrational spectroscopy. *Journal of the American Chemical Society* **2004,** *126* (29), 8894-8895.

108. Liu, J.; Conboy, J. C., 1,2-diacyl-phosphatidylcholine flip-flop measured directly by sum-frequency vibrational spectroscopy. *Biophysical Journal* **2005,** *89* (4), 2522-2532.

109. Brown, K. L.; Conboy, J. C., Lipid Flip-Flop in Binary Membranes Composed of Phosphatidylserine and Phosphatidylcholine. *Journal of Physical Chemistry B* **2013,** *117* (48), 15041-15050.

110. Weeraman, C.; Yatawara, A. K.; Bordenyuk, A. N.; Benderskii, A. V., Effect of nanoscale geometry on molecular conformation: Vibrational sum-frequency generation of alkanethiols on gold nanoparticles. *Journal of the American Chemical Society* **2006,** *128* (44), 14244-14245.

111. Zorn, G.; Dave, S. R.; Weidner, T.; Gao, X. H.; Castner, D. G., Direct characterization of polymer encapsulated CdSe/CdS/ZnS quantum dots. *Surface Science* **2016,** *648*, 339-344.

112. Howell, C.; Schmidt, R.; Kurz, V.; Koelsch, P., Sum-frequency-generation spectroscopy of DNA films in air and aqueous environments. *Biointerphases* **2008,** *3* (3), FC47-FC51.

113. Howell, C.; Hamoudi, H.; Heissler, S.; Koelsch, P.; Zharnikov, M., Orientation changes in surface-bound hybridized DNA undergoing preparation for ex situ spectroscopic measurements. *Chemical Physics Letters* **2011,** *513* (4-6), 267-270.

114. Howell, C.; Zhao, J. L.; Koelsch, P.; Zharnikov, M., Hybridization in ssDNA films-a multi-technique spectroscopy study. *Physical Chemistry Chemical Physics* **2011,** *13* (34), 15512-15522.

115. Asanuma, H.; Noguchi, H.; Uosalki, K.; Yu, H. Z., Metal cation-induced deformation of DNA self-assembled monolayers on silicon: Vibrational sum frequency generation spectroscopy. *Journal of the American Chemical Society* **2008,** *130* (25), 8016-8022.

116. Howell, C.; Diesner, M. O.; Grunze, M.; Koelsch, P., Probing the Extracellular Matrix with Sum-Frequency-Generation Spectroscopy. *Langmuir* **2008,** *24* (24), 13819-13821.

117. Diesner, M. O.; Howell, C.; Kurz, V.; Verreault, D.; Koelsch, P., In Vitro Characterization of Surface Properties Through Living Cells. *Journal of Physical Chemistry Letters* **2010,** *1* (15), 2339-2342.

118. Diesner, M. O.; Welle, A.; Kazanci, M.; Kaiser, P.; Spatz, J.; Koelsch, P., In vitro observation of dynamic ordering processes in the extracellular matrix of living, adherent cells. *Biointerphases* **2011,** *6* (4), 171-179.

119. Roy, S.; Covert, P. A.; FitzGerald, W. R.; Hore, D. K., Biomolecular Structure at Solid-Liquid Interfaces As Revealed by Nonlinear Optical Spectroscopy. *Chemical Reviews* **2014,** *114* (17), 8388-8415.

120. Yan, E. C. Y.; Fu, L.; Wang, Z. G.; Liu, W., Biological Macromolecules at Interfaces Probed by Chiral Vibrational Sum Frequency Generation Spectroscopy. *Chemical Reviews* **2014,** *114* (17), 8471-8498.

121. Cimatu, K.; Moore, H. J.; Barriet, D.; Chinwangso, P.; Lee, T. R.; Baldelli, S., Sum frequency generation imaging microscopy of patterned self-assembled monolayers with terminal -CH3, -OCH3, -CF2CF3, -C = C, -phenyl, and -cyclopropyl groups. *Journal of Physical Chemistry C* **2008,** *112* (37), 14529-14537.

122. Cimatu, K. A.; Baldelli, S., Chemical Microscopy of Surfaces by Sum Frequency Generation Imaging. *Journal of Physical Chemistry C* **2009,** *113* (38), 16575-16588.

123. Wang, H. Y.; Gao, T.; Xiong, W., Self-Phase-Stabilized Heterodyne Vibrational Sum Frequency Generation Microscopy. *Acs Photonics* **2017,** *4* (7), 1839-1845.

124. Haber, L. H.; Kwok, S. J. J.; Semeraro, M.; Eisenthal, K. B., Probing the colloidal gold nanoparticle/aqueous interface with second harmonic generation. *Chemical Physics Letters* **2011,** *507* (1-3), 11-14.

125. Liu, J.; Subir, M.; Nguyen, K.; Eisenthal, K. B., Second Harmonic Studies of Ions Crossing Liposome Membranes in Real Time. *Journal of Physical Chemistry B* **2008,** *112* (48), 15263-15266.

126. Liu, Y.; Yan, E. C. Y.; Eisenthal, K. B., Effects of bilayer surface charge density on molecular adsorption and transport across liposome bilayers. *Biophysical Journal* **2001,** *80* (2), 1004-1012.

127. Yan, E. C. Y.; Eisenthal, K. B., Effect of cholesterol on molecular transport of organic cations across liposome bilayers probed by second harmonic generation. *Biophysical Journal* **2000,** *79* (2), 898-903.

128. Dadap, J. I.; Shan, J.; Eisenthal, K. B.; Heinz, T. F., Second-harmonic Rayleigh scattering from a sphere of centrosymmetric material. *Physical Review Letters* **1999,** *83* (20), 4045-4048.

129. Yan, E. C. Y.; Eisenthal, K. B., Probing the interface of microscopic clay particles in aqueous solution by second harmonic generation. *Journal of Physical Chemistry B* **1999,** *103* (29), 6056-6060.

130. Wang, H. F.; Yan, E. C. Y.; Liu, Y.; Eisenthal, K. B., Energetics and population of molecules at microscopic liquid and solid surfaces. *Journal of Physical Chemistry B* **1998,** *102* (23), 4446-4450.

131. Yan, E. C. Y.; Liu, Y.; Eisenthal, K. B., New method for determination of surface potential of microscopic particles by second harmonic generation. *Journal of Physical Chemistry B* **1998,** *102* (33), 6331-6336.

132. Dadap, J. I.; Shan, J.; Heinz, T. F., Theory of optical second-harmonic generation from a sphere of centrosymmetric material: small-particle limit. *Journal of the Optical Society of America B-Optical Physics* **2004,** *21* (7), 1328-1347.

133. Jen, S. H.; Dai, H. L., Probing molecules adsorbed at the surface of nanometer colloidal particles by optical second-harmonic generation. *Journal of Physical Chemistry B* **2006,** *110* (46), 23000-23003.

134. Schneider, L.; Schmid, H. J.; Peukert, W., Influence of particle size and concentration on the second-harmonic signal generated at colloidal surfaces. *Applied Physics B-Lasers and Optics* **2007,** *87* (2), 333-339.

135. Das, A.; Chakrabarti, A.; Das, P. K., Probing protein adsorption on a nanoparticle surface using second harmonic light scattering. *Physical Chemistry Chemical Physics* **2016,** *18* (35), 24325-24331.

136. Smolentsev, N.; Smit, W. J.; Bakker, H. J.; Roke, S., The interfacial structure of water droplets in a hydrophobic liquid. *Nature Communications* **2017,** *8*.

137. Okur, H. I.; Chen, Y. X.; Smolentsev, N.; Zdrali, E.; Roke, S., Interfacial Structure and Hydration of 3D Lipid Monolayers in Aqueous Solution. *Journal of Physical Chemistry B* **2017,** *121* (13), 2808-2813.

138. Smolentsev, N.; Lutgebaucks, C.; Okur, H. I.; de Beer, A. G. F.; Roke, S., Intermolecular Headgroup Interaction and Hydration as Driving Forces for Lipid Transmembrane Asymmetry. *Journal of the American Chemical Society* **2016,** *138* (12), 4053-4060.

139. de Aguiar, H. B.; Scheu, R.; Jena, K. C.; de Beer, A. G. F.; Roke, S., Comparison of scattering and reflection SFG: a question of phase-matching. *Physical Chemistry Chemical Physics* **2012,** *14* (19), 6826-6832.

140. Strader, M. L.; de Aguiar, H. B.; de Beer, A. G. F.; Roke, S., Label-free spectroscopic detection of vesicles in water using vibrational sum frequency scattering. *Soft Matter* **2011,** *7* (10), 4959-4963.

141. Vacha, R.; Rick, S. W.; Jungwirth, P.; de Beer, A. G. F.; de Aguiar, H. B.; Samson, J. S.; Roke, S., The Orientation and Charge of Water at the Hydrophobic Oil Droplet-Water Interface. *Journal of the American Chemical Society* **2011,** *133* (26), 10204-10210.

142. de Beer, A. G. F.; Roke, S., Obtaining molecular orientation from second harmonic and sum frequency scattering experiments in water: Angular distribution and polarization dependence. *Journal of Chemical Physics* **2010,** *132* (23).

143. de Beer, A. G. F.; Roke, S., Nonlinear Mie theory for second-harmonic and sum-frequency scattering. *Physical Review B* **2009,** *79* (15).

144. de Beer, A. G. F.; Roke, S., Sum frequency generation scattering from the interface of an isotropic particle: Geometrical and chiral effects. *Physical Review B* **2007,** *75* (24).

145. Roke, S.; Bonn, M.; Petukhov, A. V., Nonlinear optical scattering: The concept of effective susceptibility. *Physical Review B* **2004,** *70* (11).

146. de Beer, A. G. F.; Campen, R. K.; Roke, S., Separating surface structure and surface charge with second-harmonic and sum-frequency scattering. *Physical Review B* **2010,** *82* (23).

147. Lutgebaucks, C.; Macias-Romero, C.; Roke, S., Characterization of the interface of binary mixed DOPC:DOPS liposomes in water: The impact of charge condensation. *Journal of Chemical Physics* **2017,** *146* (4), 7.

148. de Aguiar, H. B.; Samson, J. S.; Roke, S., Probing nanoscopic droplet interfaces in aqueous solution with vibrational sum-frequency scattering: A study of the effects of path length, droplet density and pulse energy (vol 512, pg 7680, 2011). *Chemical Physics Letters* **2012,** *531*, 275-275.

149. Johansson, P. K.; Koelsch, P., Vibrational Sum-Frequency Scattering for Detailed Studies of Collagen Fibers in Aqueous Environments. *Journal of the American Chemical Society* **2014,** *136* (39), 13598-13601.

150. de Beer, A. G. F.; Roke, S.; Dadap, J. I., Theory of optical second-harmonic and sum-frequency scattering from arbitrarily shaped particles. *Journal of the Optical Society of America B-Optical Physics* **2011,** *28* (6), 1374-1384.

151. Selkoe, D. J.; Hardy, J., The amyloid hypothesis of Alzheimer's disease at 25years. *Embo Molecular Medicine* **2016,** *8* (6), 595-608.

152. Knowles, T. P. J.; Vendruscolo, M.; Dobson, C. M., The amyloid state and its association with protein misfolding diseases. *Nature Reviews Molecular Cell Biology* **2014,** *15* (6), 384-396.

153. Chiti, F.; Dobson, C. M., Protein misfolding, functional amyloid, and human disease. In *Annual Review of Biochemistry*, 2006; Vol. 75, pp 333-366.

154. Exposito, J. Y.; Valcourt, U.; Cluzel, C.; Lethias, C., The Fibrillar Collagen Family. *International Journal of Molecular Sciences* **2010,** *11* (2), 407-426.

155. Shayegan, M.; Altindal, T.; Kiefl, E.; Forde, N. R., Intact Telopeptides Enhance Interactions between Collagens. *Biophysical Journal* **2016,** *111* (11), 2404-2416.

156. Jiang, F. Z.; Horber, H.; Howard, J.; Muller, D. J., Assembly of collagen into microribbons: effects of pH and electrolytes. *Journal of Structural Biology* **2004,** *148* (3), 268-278.

157. Harris, J. R.; Reiber, A., Influence of saline and pH on collagen type I fibrillogenesis in vitro: Fibrit polymorphism and colloidal gold labelling. *Micron* **2007,** *38* (5), 513-521.

158. Williams, B. R.; Gelman, R. A.; Poppke, D. C.; Piez, K. A., Collagen fibril formation - optimal invitro conditions and preliminary kinetic results. *Journal of Biological Chemistry* **1978,** *253* (18), 6578-6585.

159. Pinotsi, D.; Grisanti, L.; Mahou, P.; Gebauer, R.; Kaminski, C. F.; Hassanali, A.; Schierle, G. S. K., Proton Transfer and Structure-Specific Fluorescence in Hydrogen Bond-Rich Protein Structures. *Journal of the American Chemical Society* **2016,** *138* (9), 3046-3057.

160. Chan, F. T. S.; Schierle, G. S. K.; Kumita, J. R.; Bertoncini, C. W.; Dobson, C. M.; Kaminski, C. F., Protein amyloids develop an intrinsic fluorescence signature during aggregation. *Analyst* **2013,** *138* (7), 2156-2162.

161. del Mercato, L. L.; Pompa, P. P.; Maruccio, G.; Della Torre, A.; Sabella, S.; Tamburro, A. M.; Cingolani, R.; Rinaldi, R., Charge transport and intrinsic fluorescence in amyloid-like fibrils. *Proceedings of the National Academy of Sciences of the United States of America* **2007,** *104* (46), 18019-18024.

162. Mains, J.; Lamprou, D. A.; McIntosh, L.; Oswald, I. D. H.; Urquhart, A. J., Beta-adrenoceptor antagonists affect amyloid nanostructure; amyloid hydrogels as drug delivery vehicles. *Chemical Communications* **2013,** *49* (44), 5082-5084.

163. Schleeger, M.; vandenAkker, C. C.; Deckert-Gaudig, T.; Deckert, V.; Velikov, K. P.; Koenderink, G.; Bonn, M., Amyloids: From molecular structure to mechanical properties. *Polymer* **2013,** *54* (10), 2473-2488.

164. Elfwing, A.; Backlund, F. G.; Musumeci, C.; Inganas, O.; Solin, N., Protein nanowires with conductive properties. *Journal of Materials Chemistry C* **2015,** *3* (25), 6499-6504.

165. Hamedi, M.; Herland, A.; Karlsson, R. H.; Inganas, O., Electrochemical devices made from conducting nanowire networks self-assembled from amyloid fibrils and alkoxysulfonate PEDOT. *Nano Letters* **2008,** *8* (6), 1736-1740.

166. Rizzo, A.; Solin, N.; Lindgren, L. J.; Andersson, M. R.; Inganas, O., White Light with Phosphorescent Protein Fibrils in OLEDs. *Nano Letters* **2010,** *10* (6), 2225-2230.

167. Tanaka, H.; Herland, A.; Lindgren, L. J.; Tsutsui, T.; Andersson, M. R.; Inganas, O., Enhanced current efficiency from bio-organic light-emitting diodes using decorated amyloid fibrils with conjugated polymer. *Nano Letters* **2008,** *8* (9), 2858-2861.

168. Hanczyc, P.; Samoc, M.; Norden, B., Multiphoton absorption in amyloid protein fibres. *Nature Photonics* **2013,** *7* (12), 969-972.

169. Amit, M.; Appel, S.; Cohen, R.; Cheng, G.; Hamley, I. W.; Ashkenasy, N., Hybrid Proton and Electron Transport in Peptide Fibrils. *Advanced Functional Materials* **2014,** *24* (37), 5873-5880.

170. Tao, K.; Fan, Z.; Sun, L. M.; Makam, P.; Tian, Z.; Ruegsegger, M.; Shaham-Niv, S.; Hansford, D.; Aizen, R.; Pan, Z.; Galster, S.; Ma, J. J.; Yuan, F.; Si, M. S.; Qu, S. N.; Zhang, M. J.; Gazit, E.; Li, J. B., Quantum confined peptide assemblies with tunable visible to near-infrared spectral range. *Nature Communications* **2018,** *9*, 11.

171. Cannon, D.; Eichhorn, S. J.; Donald, A. M., Structure of Spherulites in Insulin, beta-Lactoglobulin, and Amyloid beta. *Acs Omega* **2016,** *1* (5), 915-922.

172. Smith, M. I.; Fodera, V.; Sharp, J. S.; Roberts, C. J.; Donald, A. M., Factors affecting the formation of insulin amyloid spherulites. *Colloids and Surfaces B-Biointerfaces* **2012,** *89*, 216-222.

173. Domike, K. R.; Hardin, E.; Armstead, D. N.; Donald, A. M., Investigating the inner structure of irregular beta-lactoglobulin spherulites. *European Physical Journal E* **2009,** *29* (2), 173-182.

174. Domike, K. R.; Donald, A. M., Kinetics of spherulite formation and growth: Salt and protein concentration dependence on proteins beta-lactoglobulin and insulin. *International Journal of Biological Macromolecules* **2009,** *44* (4), 301-310.

175. Domike, K. R.; Donald, A. M., Thermal dependence of thermally induced protein spherulite formation and growth: Kinetics of beta-lactoglobulin and insulin. *Biomacromolecules* **2007,** *8* (12), 3930-3937.

176. Rogers, S. S.; Krebs, M. R. H.; Bromley, E. H. C.; van der Linden, E.; Donald, A. M., Optical microscopy of growing insulin amyloid spherulites on surfaces in vitro. *Biophysical Journal* **2006,** *90* (3), 1043-1054.

177. Krebs, M. R. H.; Bromley, E. H. C.; Rogers, S. S.; Donald, A. M., The mechanism of amyloid spherulite formation by bovine insulin. *Biophysical Journal* **2005,** *88* (3), 2013-2021.

178. Krebs, M. R. H.; MacPhee, C. E.; Miller, A. F.; Dunlop, I. E.; Dobson, C. M.; Donald, A. M., The formation of spherulites by amyloid fibrils of bovine insulin. *Proceedings of the National Academy of Sciences of the United States of America* **2004,** *101* (40), 14420-14424.

179. House, E.; Jones, K.; Exley, C., Spherulites in Human Brain Tissue are Composed of Beta Sheets of Amyloid and Resemble Senile Plaques. *Journal of Alzheimers Disease* **2011,** *25* (1), 43-46.

180. Exley, C.; House, E.; Collingwood, J. F.; Davidson, M. R.; Cannon, D.; Donald, A. M., Spherulites of Amyloid-beta(42) In Vitro and in Alzheimer's Disease. *Journal of Alzheimers Disease* **2010,** *20* (4), 1159-1165.

181. Fu, L.; Ma, G.; Yan, E. C. Y., In Situ Misfolding of Human Islet Amyloid Polypeptide at Interfaces Probed by Vibrational Sum Frequency Generation. *Journal of the American Chemical Society* **2010,** *132* (15), 5405-5412.

182. Leikin, S.; Rau, D. C.; Parsegian, V. A., Temperature-favored assembly of collagen is driven by hydrophilic not hydrophobic interactions. *Nature Structural Biology* **1995,** *2* (3), 205-210.

183. Conwayjacobs, A.; Lewin, L. M., Isoelectric focusing in acrylamide gels - use of amphoteric dyes as internal markers for determination of isoelectric points. *Analytical Biochemistry* **1971,** *43* (2), 394-+.

184. Wintersteiner, O.; Abramson, H. A., The isoelectric point of insulin - Electrical properties of adsorbed and crystalline insulin. *Journal of Biological Chemistry* **1933,** *99* (3), 741-753.

185. Yan, Y. F.; Seeman, D.; Zheng, B. Q.; Kizilay, E.; Xu, Y. S.; Dubin, P. L., pH-Dependent Aggregation and Disaggregation of Native beta-Lactoglobulin in Low Salt. *Langmuir* **2013,** *29* (14), 4584-4593.

186. Whittingham, J. L.; Scott, D. J.; Chance, K.; Wilson, A.; Finch, J.; Brange, J.; Dodson, G. G., Insulin at pH 2: Structural analysis of the conditions promoting insulin fibre formation. *Journal of Molecular Biology* **2002,** *318* (2), 479-490.

187. Kahn, S. E.; Andrikopoulos, S.; Verchere, C. B., Islet amyloid: A long-recognized but underappreciated pathological feature of type 2 diabetes. *Diabetes* **1999,** *48* (2), 241-253.

188. Provenzano, P. P.; Vanderby, R., Collagen fibril morphology and organization: Implications for force transmission in ligament and tendon. *Matrix Biology* **2006,** *25* (2), 71-84.

189. Chernoff, E. A. G.; Chernoff, D. A., Atomic force microscope images of collagen-fibers. *Journal of Vacuum Science & Technology a-Vacuum Surfaces and Films* **1992,** *10* (4), 596-599.

190. Bozec, L.; Horton, M., Topography and mechanical properties of single molecules of type I collagen using atomic force microscopy. *Biophysical Journal* **2005,** *88* (6), 4223-4231.

191. Orgel, J. P. R. O.; Irving, T. C.; Miller, A.; Wess, T. J., Microfibrillar structure of type I collagen in situ. *Proceedings of the National Academy of Sciences of the United States of America* **2006,** *103* (24), 9001-9005.

192. Bella, J.; Eaton, M.; Brodsky, B.; Berman, H. M., Crystal-structure and molecular-structure of a collagen-like peptide at 1.9-angstrom resolution. *Science* **1994,** *266* (5182), 75-81.

193. Li, M. H.; Fan, P.; Brodsky, B.; Baum, J., 2-Dimensional nmr assignments and conformation of (pro-hyp-gly)(10) and a designed collagen triple-helical peptide. *Biochemistry* **1993,** *32* (29), 7377-7387.

194. Reiser, K. M.; McCourt, A. B.; Yankelevich, D. R.; Knoesen, A., Structural Origins of Chiral Second-Order Optical Nonlinearity in Collagen: Amide I Band. *Biophysical Journal* **2012,** *103* (10), 2177-2186.

195. Rocha-Mendoza, I.; Yankelevich, D. R.; Wang, M.; Reiser, K. M.; Frank, C. W.; Knoesen, A., Sum frequency vibrational spectroscopy: The molecular origins of the optical second-order nonlinearity of collagen. *Biophysical Journal* **2007,** *93* (12), 4433-4444.

196. de Beer, A. G. F.; de Aguiar, H. B.; Nijsen, J. F. W.; Roke, S., Detection of Buried Microstructures by Nonlinear Light Scattering Spectroscopy. *Physical Review Letters* **2009,** *102* (9).

197. Piez, K. A.; Miller, A., The structure of collagen fibrils. *Journal of Supramolecular Structure* **1974,** *2* (2-4), 121-137.

198. Kadler, K. E.; Holmes, D. F.; Trotter, J. A.; Chapman, J. A., Collagen fibril formation. *Biochemical Journal* **1996,** *316*, 1-11.

199. Lazarev, Y. A.; Grishkovsky, B. A.; Khromova, T. B., Amide-i band of ir-spectrum and structure of collagen and related polypeptides. *Biopolymers* **1985,** *24* (8), 1449-1478.

200. Bryan, M. A.; Brauner, J. W.; Anderle, G.; Flach, C. R.; Brodsky, B.; Mendelsohn, R., FTIR studies of collagen model peptides: Complementary experimental and simulation

approaches to conformation and unfolding. *Journal of the American Chemical Society* **2007,** *129* (25), 7877-7884.

201. de Beer, A. G. F.; Samson, J. S.; Hua, W.; Huang, Z. S.; Chen, X. K.; Allen, H. C.; Roke, S., Direct comparison of phase-sensitive vibrational sum frequency generation with maximum entropy method: Case study of water. *Journal of Chemical Physics* **2011,** *135* (22).

202. Miller, C. A.; Fildes, J. E.; Ray, S. G.; Doran, H.; Yonan, N.; Williams, S. G.; Schmitt, M., Non-invasive approaches for the diagnosis of acute cardiac allograft rejection. *Heart* **2013,** *99* (7), 445-453.

203. Wilhelm, M. J., Long-term outcome following heart transplantation: current perspective. *Journal of Thoracic Disease* **2015,** *7* (3), 549-551.

204. Ott, H. C.; Matthiesen, T. S.; Goh, S. K.; Black, L. D.; Kren, S. M.; Netoff, T. I.; Taylor, D. A., Perfusion-decellularized matrix: using nature's platform to engineer a bioartificial heart. *Nature Medicine* **2008,** *14* (2), 213-221.

205. Uygun, B. E.; Soto-Gutierrez, A.; Yagi, H.; Izamis, M. L.; Guzzardi, M. A.; Shulman, C.; Milwid, J.; Kobayashi, N.; Tilles, A.; Berthiaume, F.; Hertl, M.; Nahmias, Y.; Yarmush, M. L.; Uygun, K., Organ reengineering through development of a transplantable recellularized liver graft using decellularized liver matrix. *Nature Medicine* **2010,** *16* (7), 814-U120.

206. Song, J. J.; Guyette, J. P.; Gilpin, S. E.; Gonzalez, G.; Vacanti, J. P.; Ott, H. C., Regeneration and experimental orthotopic transplantation of a bioengineered kidney. *Nature Medicine* **2013,** *19* (5), 646-651.

207. Petersen, T. H.; Calle, E. A.; Zhao, L. P.; Lee, E. J.; Gui, L. Q.; Raredon, M. B.; Gavrilov, K.; Yi, T.; Zhuang, Z. W.; Breuer, C.; Herzog, E.; Niklason, L. E., Tissue-Engineered Lungs for in Vivo Implantation. *Science* **2010,** *329* (5991), 538-541.

208. Stabler, C. T.; Lecht, S.; Mondrinos, M. J.; Goulart, E.; Lazarovici, P.; Lelkes, P. I., Revascularization of decellularized lung scaffolds: principles and progress. *American Journal of Physiology-Lung Cellular and Molecular Physiology* **2015,** *309* (11), L1273-L1285.

209. Goh, S. K.; Bertera, S.; Olsen, P.; Candiello, J. E.; Halfter, W.; Uechi, G.; Balasubramani, M.; Johnson, S. A.; Sicari, B. M.; Kollar, E.; Badylak, S. F.; Banerjee, I., Perfusion-decellularized pancreas as a natural 3D scaffold for pancreatic tissue and whole organ engineering. *Biomaterials* **2013,** *34* (28), 6760-6772.

210. Crapo, P. M.; Gilbert, T. W.; Badylak, S. F., An overview of tissue and whole organ decellularization processes. *Biomaterials* **2011,** *32* (12), 3233-3243.

211. Keane, T. J.; Swinehart, I. T.; Badylak, S. F., Methods of tissue decellularization used for preparation of biologic scaffolds and in vivo relevance. *Methods* **2015,** *84*, 25-34.

212. Starborg, T.; Lu, Y.; Kadler, K. E.; Holmes, D. F., Electron microscopy of collagen fibril structure in vitro and in vivo including three-dimensional reconstruction. In *Introduction to Electron Microscopy for Biologists*, Allen, T. D., Ed. Elsevier Academic Press Inc: San Diego, 2008; Vol. 88, pp 319-+.

213. Faulk, D. M.; Carruthers, C. A.; Warner, H. J.; Kramer, C. R.; Reing, J. E.; Zhang, L.; D'Amore, A.; Badylak, S. F., The effect of detergents on the basement membrane complex of a biologic scaffold material. *Acta Biomaterialia* **2014,** *10* (1), 183-193.

214. Vidal, B. D.; Mello, M. L. S., Collagen type I amide I band infrared spectroscopy. *Micron* **2011,** *42* (3), 283-289.

215. Li, Y.; Foss, C. A.; Summerfield, D. D.; Doyle, J. J.; Torok, C. M.; Dietz, H. C.; Pomper, M. G.; Yu, S. M., Targeting collagen strands by photo-triggered triple-helix hybridization. *Proceedings of the National Academy of Sciences of the United States of America* **2012,** *109* (37), 14767-14772.

216. Li, Y.; Ho, D.; Meng, H.; Chan, T. R.; An, B.; Yu, H.; Brodsky, B.; Jun, A. S.; Yu, S. M., Direct Detection of Collagenous Proteins by Fluorescently Labeled Collagen Mimetic Peptides. *Bioconjugate Chemistry* **2013,** *24* (1), 9-16.

217. Hwang, J. M.; San, B. H.; Turner, N. J.; White, L. J.; Faulk, D. M.; Badylak, S. F.; Li, Y.; Yu, S. M., Molecular assessment of collagen denaturation in decellularized tissues using a collagen hybridizing peptide. *Acta Biomaterialia* **2017,** *53*, 268-278.

218. Deniset-Besseau, A.; Duboisset, J.; Benichou, E.; Hache, F.; Brevet, P. F.; Schanne-Klein, M. C., Measurement of the Second-Order Hyperpolarizability of the Collagen Triple Helix and Determination of Its Physical Origin. *Journal of Physical Chemistry B* **2009,** *113* (40), 13437-13445.

219. Su, P. J.; Chen, W. L.; Li, T. H.; Chou, C. K.; Chen, T. H.; Ho, Y. Y.; Huang, C. H.; Chang, S. J.; Huang, Y. Y.; Lee, H. S.; Dong, C. Y., The discrimination of type I and type II collagen and the label-free imaging of engineered cartilage tissue. *Biomaterials* **2010,** *31* (36), 9415-9421.

220. Hanninen, A.; Shu, M. W.; Potma, E. O., Hyperspectral imaging with laser-scanning sum-frequency generation microscopy. *Biomedical Optics Express* **2017,** *8* (9), 4230-4242.

221. Han, Y.; Hsu, J. L.; Ge, N. H.; Potma, E. O., Polarization-Sensitive Sum-Frequency Generation Microscopy of Collagen Fibers. *Journal of Physical Chemistry B* **2015,** *119* (8), 3356-3365.

222. Han, Y.; Raghunathan, V.; Feng, R. R.; Maekawa, H.; Chung, C. Y.; Feng, Y.; Potma, E. O.; Ge, N. H., Mapping Molecular Orientation with Phase Sensitive Vibrationally Resonant Sum-Frequency Generation Microscopy. *Journal of Physical Chemistry B* **2013,** *117* (20), 6149-6156.

223. Olenick, L. L.; Troiano, J. M.; Smolentsev, N.; Ohno, P. E.; Roke, S.; Geiger, F. M., Polycation Interactions with Zwitterionic Phospholipid Monolayers on Oil Nanodroplet

Suspensions in Water (D2O) Probed by Sum Frequency Scattering. *Journal of Physical Chemistry B* **2018,** *122* (19), 5049-5056.

224. Yang, P. K.; Huang, J. Y., Sum-frequency generation from an isotropic chiral medium. *Journal of the Optical Society of America B-Optical Physics* **1998,** *15* (6), 1698-1706.

225. Fischer, P.; Hache, F., Nonlinear optical spectroscopy of chiral molecules. *Chirality* **2005,** *17* (8), 421-437.

226. Kroes-Nijboer, A.; Venema, P.; van der Linden, E., Fibrillar structures in food. *Food & Function* **2012,** *3* (3), 221-227.

227. Shirahama, T.; Cohen, A. S., High-resolution electron microscopic analysis of amyloid fibril. *Journal of Cell Biology* **1967,** *33* (3), 679-+.

228. Makin, O. S.; Atkins, E.; Sikorski, P.; Johansson, J.; Serpell, L. C., Molecular basis for amyloid fibril formation and stability. *Proceedings of the National Academy of Sciences of the United States of America* **2005,** *102* (2), 315-320.

229. Smith, J. F.; Knowles, T. P. J.; Dobson, C. M.; MacPhee, C. E.; Welland, M. E., Characterization of the nanoscale properties of individual amyloid fibrils. *Proceedings of the National Academy of Sciences of the United States of America* **2006,** *103* (43), 15806-15811.

230. Sunde, M.; Serpell, L. C.; Bartlam, M.; Fraser, P. E.; Pepys, M. B.; Blake, C. C. F., Common core structure of amyloid fibrils by synchrotron X-ray diffraction. *Journal of Molecular Biology* **1997,** *273* (3), 729-739.

231. Masters, C. L.; Simms, G.; Weinman, N. A.; Multhaup, G.; McDonald, B. L.; Beyreuther, K., Amyloid plaque core protein in alzheimer-disease and down syndrome. *Proceedings of the National Academy of Sciences of the United States of America* **1985,** *82* (12), 4245-4249.

232. Serpell, L. C., Alzheimer's amyloid fibrils: structure and assembly. *Biochimica Et Biophysica Acta-Molecular Basis of Disease* **2000,** *1502* (1), 16-30.

233. Westermark, P.; Wernstedt, C.; Wilander, E.; Hayden, D. W.; Obrien, T. D.; Johnson, K. H., Amyloid fibrils in human insulinoma and islets of langerhans of the diabetic cat are derived from a neuropeptide-like protein also present in normal islet cells. *Proceedings of the National Academy of Sciences of the United States of America* **1987,** *84* (11), 3881-3885.

234. Westermark, P.; Engstrom, U.; Johnson, K. H.; Westermark, G. T.; Betsholtz, C., Islet amyloid polypeptide - pinpointing amino-acid-residues linked to amyloid fibril formation. *Proceedings of the National Academy of Sciences of the United States of America* **1990,** *87* (13), 5036-5040.

235. Spillantini, M. G.; Schmidt, M. L.; Lee, V. M. Y.; Trojanowski, J. Q.; Jakes, R.; Goedert, M., alpha-synuclein in Lewy bodies. *Nature* **1997,** *388* (6645), 839-840.

236. Jimenez, J. L.; Nettleton, E. J.; Bouchard, M.; Robinson, C. V.; Dobson, C. M.; Saibil, H. R., The protofilament structure of insulin amyloid fibrils. *Proceedings of the National Academy of Sciences of the United States of America* **2002,** *99* (14), 9196-9201.

237. Bromley, E. H. C.; Krebs, M. R. H.; Donald, A. M., Aggregation across the length-scales in beta-lactoglobulin. *Faraday Discussions* **2005,** *128*, 13-27.

238. Hamada, D.; Dobson, C. M., A kinetic study of beta-lactoglobulin amyloid fibril formation promoted by urea. *Protein Science* **2002,** *11* (10), 2417-2426.

239. Mankar, S.; Anoop, A.; Sen, S.; Maji, S. K., Nanomaterials: amyloids reflect their brighter side. *Nano Reviews & Experiments* **2011,** *2* (1).

240. Scheibel, T.; Parthasarathy, R.; Sawicki, G.; Lin, X. M.; Jaeger, H.; Lindquist, S. L., Conducting nanowires built by controlled self-assembly of amyloid fibers and selective metal deposition. *Proceedings of the National Academy of Sciences of the United States of America* **2003,** *100* (8), 4527-4532.

241. Sharpe, S.; Simonetti, K.; Yau, J.; Walsh, P., Solid-State NMR Characterization of Autofluorescent Fibrils Formed by the Elastin-Derived Peptide GVGVAGVG. *Biomacromolecules* **2011,** *12* (5), 1546-1555.

242. Pinotsi, D.; Buell, A. K.; Dobson, C. M.; Schierle, G. S. K.; Kaminski, C. F., A Label-Free, Quantitative Assay of Amyloid Fibril Growth Based on Intrinsic Fluorescence. *Chembiochem* **2013,** *14* (7), 846-850.

243. Amit, M.; Cheng, G.; Hamley, I. W.; Ashkenasy, N., Conductance of amyloid beta based peptide filaments: structure-function relations. *Soft Matter* **2012,** *8* (33), 8690-8696.

244. Rosenberg, B., ELECTRICAL CONDUCTIVITY OF PROTEINS. *Nature* **1962,** *193* (4813), 364-&.

245. Perutz, M. F.; Finch, J. T.; Berriman, J.; Lesk, A., Amyloid fibers are water-filled nanotubes. *Proceedings of the National Academy of Sciences of the United States of America* **2002,** *99* (8), 5591-5595.

246. Shukla, A.; Mukherjee, S.; Sharma, S.; Agrawal, V.; Kishan, K. V. R.; Guptasarma, P., A novel UV laser-induced visible blue radiation from protein crystals and aggregates: scattering artifacts or fluorescence transitions of peptide electrons delocalized through hydrogen bonding? *Archives of Biochemistry and Biophysics* **2004,** *428* (2), 144-153.

247. Novakovskaya, Y. V., Conjugation in hydrogen-bonded systems. *Structural Chemistry* **2012,** *23* (4), 1253-1266.

248. Jin, L. W.; Claborn, K. A.; Kurimoto, M.; Geday, M. A.; Maezawa, I.; Sohraby, F.; Estrada, M.; Kaminsky, W.; Kahr, B., Imaging linear birefringence and dichroism in cerebral amyloid pathologies. *Proceedings of the National Academy of Sciences of the United States of America* **2003,** *100* (26), 15294-15298.

249. Luhrs, T.; Ritter, C.; Adrian, M.; Riek-Loher, D.; Bohrmann, B.; Doeli, H.; Schubert, D.; Riek, R., 3D structure of Alzheimer's amyloid-beta(1-42) fibrils. *Proceedings of the National Academy of Sciences of the United States of America* **2005,** *102* (48), 17342-17347.

250. Ban, T.; Morigaki, K.; Yagi, H.; Kawasaki, T.; Kobayashi, A.; Yuba, S.; Naiki, H.; Goto, Y., Real-time and single fibril observation of the formation of amyloid beta spherulitic structures. *Journal of Biological Chemistry* **2006,** *281* (44), 33677-33683.

251. Yagi, H.; Ban, T.; Morigaki, K.; Naiki, H.; Goto, Y., Visualization and classification of amyloid beta supramolecular assemblies. *Biochemistry* **2007,** *46* (51), 15009-15017.

252. Gellermann, G. P.; Byrnes, H.; Striebinger, A.; Ullrich, K.; Mueller, R.; Hillen, H.; Barghorn, S., A beta-globulomers are formed independently of the fibril pathway. *Neurobiology of Disease* **2008,** *30* (2), 212-220.

253. Faendrich, M.; Schmidt, M.; Grigorieff, N., Recent progress in understanding Alzheimer's beta-amyloid structures. *Trends in Biochemical Sciences* **2011,** *36* (6), 338-345.

254. Shimanouchi, T.; Shimauchi, N.; Ohnishi, R.; Kitaura, N.; Yagi, H.; Goto, Y.; Umakoshi, H.; Kuboi, R., Formation of spherulitic amyloid beta aggregate by anionic liposomes. *Biochemical and Biophysical Research Communications* **2012,** *426* (2), 165-171.

255. Cannon, D.; Donald, A. M., Control of liquid crystallinity of amyloid-forming systems. *Soft Matter* **2013,** *9* (10), 2852-2857.

256. Backlund, F. G.; Pallbo, J.; Solin, N., Controlling Amyloid Fibril Formation by Partial Stirring. *Biopolymers* **2016,** *105* (5), 249-259.

257. Backskai, B. J.; Kajdasz, S. T.; Christie, R. H.; Carter, C.; Games, D.; Seubert, P.; Schenk, D.; Hyman, B. T., Imaging of amyloid-beta deposits in brains of living mice permits direct observation of clearance of plaques with immunotherapy. *Nature Medicine* **2001,** *7* (3), 369-372.

258. Bacskai, B. J.; Klunk, W. E.; Mathis, C. A.; Hyman, B. T., Imaging amyloid-beta deposits in vivo. *Journal of Cerebral Blood Flow and Metabolism* **2002,** *22* (9), 1035-1041.

259. Christie, R. H.; Bacskai, B. J.; Zipfel, W. R.; Williams, R. M.; Kajdasz, S. T.; Webb, W. W.; Hyman, B. T., Growth arrest of individual senile plaques in a model of Alzheimer's disease observed by in vivo multiphoton microscopy. *Journal of Neuroscience* **2001,** *21* (3), 858-864.

260. Heo, C. H.; Kim, K. H.; Kim, H. J.; Baik, S. H.; Song, H.; Kim, Y. S.; Lee, J.; Mook-Jung, I.; Kim, H. M., A two-photon fluorescent probe for amyloid-beta plaques in living mice. *Chemical Communications* **2013,** *49* (13), 1303-1305.

261. Murugan, N. A.; Zalesny, R.; Kongsted, J.; Nordberg, A.; Agren, H., Promising two-photon probes for in vivo detection of beta amyloid deposits. *Chemical Communications* **2014,** *50* (79), 11694-11697.

262. Kim, D.; Moon, H.; Baik, S. H.; Singha, S.; Jun, Y. W.; Wang, T.; Kim, K. H.; Park, B. S.; Jung, J.; Mook-Jung, I.; Ahn, K. H., Two-Photon Absorbing Dyes with Minimal Autofluorescence in Tissue Imaging: Application to in Vivo Imaging of Amyloid-beta Plaques with a Negligible Background Signal. *Journal of the American Chemical Society* **2015,** *137* (21), 6781-6789.

263. Gosal, W. S.; Clark, A. H.; Pudney, P. D. A.; Ross-Murphy, S. B., Novel amyloid fibrillar networks derived from a globular protein: beta-lactoglobulin. *Langmuir* **2002,** *18* (19), 7174-7181.

264. Demchenko, A. P., The red-edge effects: 30 years of exploration. *Luminescence* **2002,** *17* (1), 19-42.

265. Chattopadhyay, A.; Haldar, S., Dynamic Insight into Protein Structure Utilizing Red Edge Excitation Shift. *Accounts of Chemical Research* **2014,** *47* (1), 12-19.

266. Lakowicz, J. R., On spectral relaxation in proteins. *Photochemistry and Photobiology* **2000,** *72* (4), 421-437.

267. Wlodarczyk, J.; Kierdaszuk, B., Interpretation of fluorescence decays using a power-like model. *Biophysical Journal* **2003,** *85* (1), 589-598.

268. Lazar, A. N.; Bich, C.; Panchal, M.; Desbenoit, N.; Petit, V. W.; Touboul, D.; Dauphinot, L.; Marquer, C.; Laprevote, O.; Brunelle, A.; Duyckaerts, C., Time-of-flight secondary ion mass spectrometry (TOF-SIMS) imaging reveals cholesterol overload in the cerebral cortex of Alzheimer disease patients. *Acta Neuropathologica* **2013,** *125* (1), 133-144.

APPENDIX A: OPERANDO SUM-FREQUENCY GENERATION DETECTION OF ELECTROLYTE REDOX PRODUCTS AT ACTIVE SI NANOPARTICLE LI-ION BATTERY INTERFACES

This appendix is adapted with permission from a previously published research article (J. Olson, et al, *Chem. Mater.*, Vol 30, Issue 4, pp 1239-1248, **2018**, DOI: 10.1021/acs.chemmater.7b04087). Copyright (2018) American Chemical Society.

A.1. SUMMARY

For the first time on nanoparticle-based Si electrodes, we monitor electrochemical reduction products of ethylene carbonate (EC) and fluoroethylene carbonate (FEC) using interface-sensitive operando spectroelectrochemical sum-frequency generation (SFG). We observe SFG signatures that suggest carbon monoxide (CO) evolution on nano-Si proceeds at distinct lithiation potentials for different electrolyte solvents. EC reduction to yield CO-associated species occurs at potentials associated with silicon’s most highly lithiated state (10 mV), whereas FEC is reduced to CO-associated species at 10 mV and 500 mV (vs Li/ Li^+). These results suggest that EC reduction is more sensitive than FEC to the lithiation state, validating previous computational predictions describing the reduction of both solvents. Our results suggest that low molecular weight oligomers that readily diffuse from the interface are formed during cycling, leading to SEI instability and an absence of SFG signal. Only upon prolonged EC reduction at 10 mV do we observe SFG signatures for poly(EC), which we hypothesize are due to the formation of higher molecular weight chains that remain on the electrode surface during SFG acquisition. Potential-dependent FEC reduction to Li_2CO_3, LiF, and CF-containing moieties evidently induces the predominant stabilizing effects to the interface, irrespective of the lithiation time scale. These results provide new, precise insight on the stability of high-capacity anodes.

A.2. SFG of Solid Electrolyte Interfaces

Spectroelectrochemical SFG studies commonly require dilute electrolyte solutions due to complications associated with experimental geometry. Specifically, the setup for acquiring SFG spectra commonly comprises IR and visible laser beams that traverse the bulk of the electrolyte solution before reaching the electrode surface to enable SFG. This can result in spectral artifacts for undiluted electrolyte solutions due to significant absorption of certain IR frequencies. In this case, the co-solvents used to dilute the analyte molecule of interest are not typically used in lithium ion batteries, and can actually adversely influence the electrode material.[1] In our spectral analyses of the SFG results, we used the relation below to fit the data,

$$\chi^{(2)}_{SFG} = \chi^{(2)}_{NR} + \sum_q \frac{A_q}{\omega_q - \omega_{IR} - i\Gamma_q} \tag{A.1}$$

where $\chi^{(2)}_{NR}$ is a nonresonant contribution, and ω_{IR} is the IR wavenumber. A_k is the amplitude for the k_{th} resonant mode, for which the peak wavenumber and half width are given by ω_k and Γ_k.

In Figure A.1, we monitor the evolution of chemical species comprising the SEI, by scanning and holding the potential at 1.2V, 0.5V and 0.01V. For EC, a peak at about 1750 cm^{-1} emerges at 0.01V, which is consistent with poly(EC). For both EC and FEC, spectral features are formed at about 1900 cm^{-1}, which is indicative of carbon monoxide. It has previously been hypothesized that the carbon monoxide is the reason for poor performance of EC on Si surfaces. However, these results indicate tha it is more likely poly(EC), as the onset of carbon monoxide is earlier for the superior FEC additive, while essentially no poly(EC) or poly(FEC) is detected.

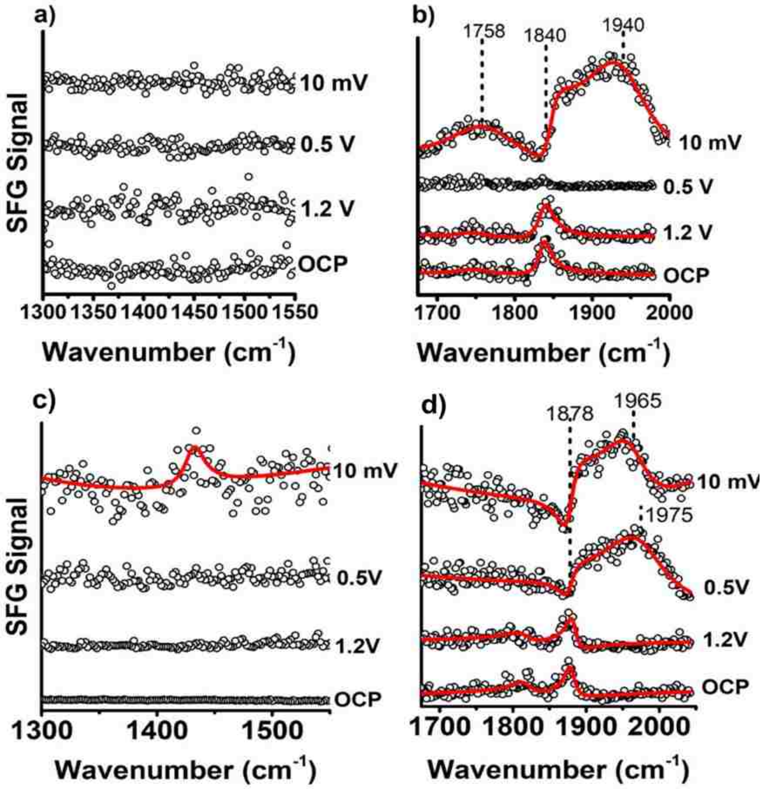

Figure A.1. SFG analysis of first cycle of the (a,c) alkyl dicarbonate and (b,d) carbonyl region using EC (a,b) and FEC (c,d) as an electrolyte solvent. Spectra were captured at OCP after the scan/hold experiments. At 0.5 V, it is clear the electrolysis of FEC at the Si electrode interface has begun, resulting in CO species detectable at ~1975 cm^{-1}. For EC, the highest lithiation state (10 mV) is needed for such species to emerge at 1940 cm^{-1}. For FEC, this lithiation state resulted in a peak at 1431 cm^{-1}, indicative of Li_2CO_3, but no such features appeared for EC.

The composition of the SEI generated on an Si anode is confirmed to include lithium alkyl carbonates and poly(EC) with the use of EC as an electrolyte solvent. While lithium alkyl carbonates are also demonstrated to form with FEC as the electrolyte solvent, the combination of concurrent LiF generation, C-F bond formation within the alkyl carbonate molecule and poly(EC) suppression demonstrate a multifaceted organic/inorganic stabilizing effect to the device. Irrespective of the electrolyte solvent used, it also appears that carbon monoxide forms as a byproduct of electrolytic reduction of the solvent. Future work with SFG-based detection of SEI structures will include the analysis of other electrolyte additives, as well as novel lithium salts.

APPENDIX B: STARK TUNING RATES OF CARBONATE-BASED ELECTROLYTE SOLVENTS APPLIED TO ELECTROCHEMICAL ENERGY STORAGE MATERIALS

This appendix is under preparation as part of a manuscript to be submitted and may appear as a scientific publication in a journal for physical chemistry and/or electrochemistry.

B.1. SUMMARY

Lithium ion batteries frequently employ carbonate-based electrolyte solvents as ion-conducting media, enabling the reversible intercalation of lithium ions through the application of strong electric fields localized at the electrode/electrolyte junction. While these fields are important for electrochemistry, their values have not yet been quantified and are crucial for the fundamental understanding and development of high voltage electrochemical energy storage devices. In this study, we utilize complementary experimental techniques of vibrational Stark spectroscopy and solvatochromism in conjunction with molecular dynamics simulations to determine the vibrational sensitivity to an electric field (expressed as the Stark tuning rate, $\Delta\vec{\mu}$) of the carbonyl group (C=O) for diethyl carbonate (DEC), ethylene carbonate (EC), and fluoroethylene carbonate (FEC). We first determine that the C=O group in each molecule exhibits a linear response to an applied electric field. Subsequently, the magnitude of this response was found to be unique among all carbonate solvents investigated in this work; $\Delta\vec{\mu}_{DEC}$ = 0.37 cm^{-1}/(MV/cm), $\Delta\vec{\mu}_{EC}$ = 0.31 cm^{-1}/(MV/cm), and $\Delta\vec{\mu}_{FEC}$ = 0.57 cm^{-1}/(MV/cm). Applying our findings to vibrational peak shifts observed in literature for DEC at a $LiCoO_2$ interface, we estimate that a local field in the range of about 37 - 52 MV/cm exists at the interface before electrochemical cycling begins, which are values that converge with theoretical models when the molecular tilt is 31° to 52° relative the surface normal.

These findings serve as a major step toward quantitatively benchmarking the local electric fields at interfaces relevant to electrochemical energy storage.

B.2. SOLVATOCHROMIC STARK SHIFT AND INTERFACIAL MODELS

For solvatochromic analysis, 1 M solutions of the carbonates (except D_4-EC) were prepared in chloroform ($CHCl_3$, sigma), dichloromethane (DCM, Fischer Scientific), dimethylsulfoxide (DMSO, EMD), tetrahydrofuran (THF, Sigma), 1,3-dioxolane, (DOL, Sigma), toluene (Tol, Alfa Aesar) and acetonitrile (ACN, Sigma). The samples were subsequently analyzed using ATR-FTIR spectroscopy. All spectra were collected on a Nicolet 8700 FTIR spectrometer using a liquid nitrogen-cooled MCT detector, averaged over 32 scans with 1 cm^{-1} resolution. All C=O vibrations were determined using the peak value obtained with a Voigt fit. Parameterization of electrolyte solvents molecules, MD equilibration and production, and determination of solvent electric fields from MD simulations were performed. Optical constants and the bulk absorption were obtained using an infrared variable angle ellipsometer housed in the Center for Integrated Nanotechnologies at Sandia National Laboratories. Spectra were collected at the CaF_2 prism/liquid interface under anhydrous conditions at room temperature with 4 cm^{-1} resolution in reflection mode at a fixed angle of 60°. Spectra were averaged over 100 scans. The Stark tuning rate ($\Delta\vec{\mu}$) can then be determined by combining vibrational solvatochromism measurements with the molecular dynamics (MD) simulations to calculate the electric field exerted by the solvent onto the C=O bond dipole. The resulting electric field-frequency calibration curves do not propagate the local field correction factor, f, since there is no externally applied field and we obtain precise values of the Stark tuning rates of DEC, EC, and FEC, which are shown in Figure B.1.

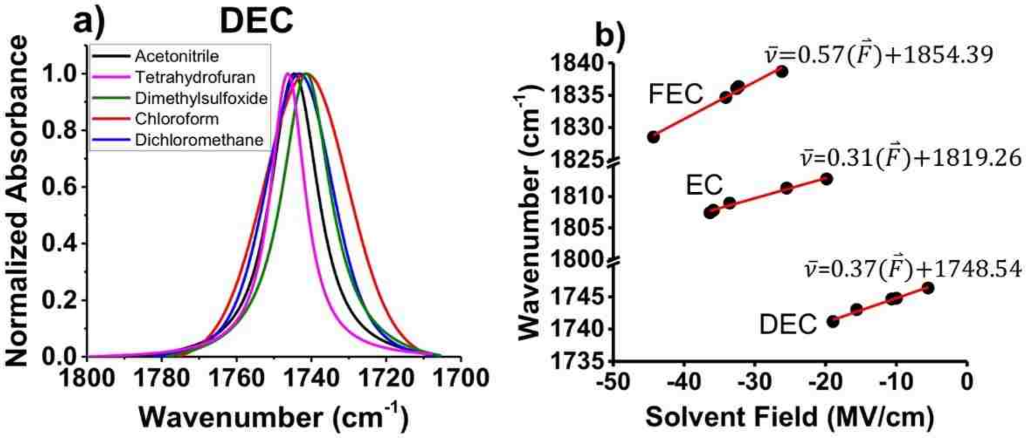

Figure B.1. Stark tuning rates from solvatochromic data. a) Example for the C=O group in DEC. b) Electric field-frequency calibration curves for FEC, EC, and DEC. A linear relationship between solvent field and peak position is observed, consistent with the linear Stark effect, and the slope corresponds to $|\Delta\vec{\mu}|$, in units of cm^{-1}/(MV/cm).

It has been previously determined that the C=O group in DEC at the interface of $LiCoO_2$ is red shifted by to approximately 1737 cm^{-1} under equilibrium (open circuit) conditions. The absorption of neat DEC solvent occurs at 1746.4 cm^{-1}, while the gas phase peak is 1756 cm^{-1}. Because equilibrium at the interface of lithiated interfaces and carbonate solvents has been described to include electrostatic processes and the redshift of the C=O has been observed at the electrode/electrolyte junction at a resting potential, we apply the above values of $\Delta\vec{\mu}_{DEC}$ to calculate the magnitude of the electrostatic field at the $LiCoO_2$/DEC junction using Eq. B.1 below. Since we have observed the linear Stark effect manifests among all carbonate solvents above, the peak shift at the electrode interface can be taken to be:

$$\Delta\bar{\nu} = -f_{int}\Delta\vec{\mu}\cdot\vec{F}_{int} = -f_{int}|\Delta\vec{\mu}||\vec{F}_{int}|\cos\beta \tag{B.1}$$

where $\Delta\bar{\nu}$ is the observed shift in peak position of the C=O group between the gas phase and at the electrode interface (-19 cm^{-1}), $\Delta\vec{\mu}$ is the tuning rate, f_{int} is the interfacial field correction factor, β is the dipole tilt angle relative the surface normal, and $\vec{F}_{int}$ represents the absolute electrostatic field at the $LiCoO_2$/DEC interface. Assuming the C=O group is oriented perpendicular to the $LiCoO_2$ surface (and $f_{int} = 1; \beta = 0°$), a local field ($\vec{F}_{int}$) of approximately 51.4 MV/cm is calculated using $|\Delta\vec{\mu}_{DEC}|$ = 0.37 $cm^{-1/}$ (MV/cm).

An estimate of $\vec{F}_{int}$ may be alternatively calculated using a theoretical model, which more formally accounts for electrostatic fields imposed upon DEC within the electrochemical double layer at the $LiCoO_2$/DEC junction. The value of $\vec{F}_{int}$ is calculated for dipoles perpendicular to the surface by:

$$\vec{F}_{int}(\varepsilon) = \frac{2\vec{\mu}}{\pi\epsilon_0 L^3}\left[\frac{(n^2+2)(1+\zeta(\varepsilon))}{3n^2+9-(n^2-1)\zeta(\varepsilon)}\right] \tag{B.2}$$

where $\vec{\mu}$ represents the dipole moment of DEC (1.07D), n the refractive index of DEC at the electrode interface (1.68, based on a static dielectric constant of 2.835), $\zeta(\varepsilon)$ an infinite sum representing the potential profile induced by the static dielectric, and L is the cavity thickness. This gives an interface field, $\vec{F}_{int}$, of 86.2 MV/cm.

Carbonate solvents have previously been shown to adopt a preferential orientation on electrode surfaces, which is likely one reason for why the two methods do not converge. Another reason could be that the cavity length is longer than expected (2.434 Å was used, twice the C=O bond length) or that the $f_{int} > 1$. To account for these factors, a more general version of Eq. B.2 has been derived for arbitrary dipole orientations:

$$\vec{F}_{int}(\varepsilon) = \frac{2\vec{\mu}}{\pi\epsilon_0 L^3}\left[\frac{(n^2+2)(1+0.577\zeta(\varepsilon)+(1+1.4226\zeta(\varepsilon))\cos^2\beta))}{7n^2+17-(n^2-1)(0.577\zeta(\varepsilon)+(1+1.4226\zeta(\varepsilon))\cos^2\beta)}\right] \tag{B.3}$$

where all parameters are defined as in Eq. B.2, with the addition of β representing the dipole tilt angle relative the surface normal. Limiting f_{int} in Eq. B.1 to $1 \leq f_{int} \leq 2.86$, and estimating the bulk value with $f_{bulk} = (\varepsilon + 2)/3 = 1.61$, a convergence between the solutions to the field-frequency calibration (Eq. B.1) and the orientation dependent interfacial Onsager model (Eq. B.3) can be achieved, which is shown in Figure B.2.

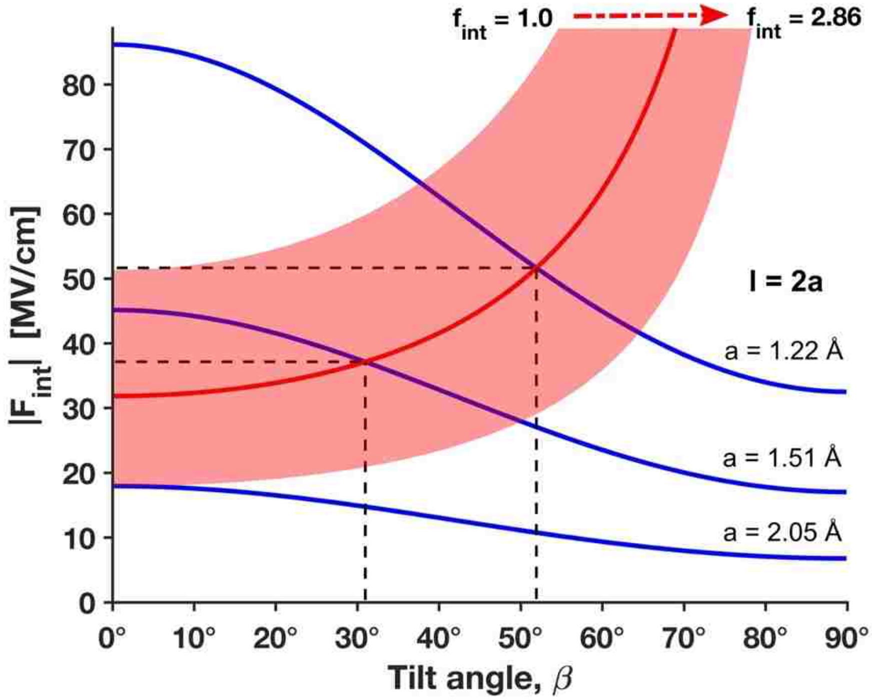

Figure B.2. Convergence of interfacial field models. a) The red region shows the field from Eq. B.1, with a range of f_{int} (1 to 2.86) and the red line highlights f_{int} = 1.61, which is the estimated value for the bulk. The blue lines represent Eq. B.3 with different cavity lengths (top: 2.434 Å, middle: 3.019 Å, and bottom: 4.105 Å). The dashed lines highlight two examples of converging values for β and $\vec{F}_{int}$ (52° and 52 MV/cm for L = 2.434 Å; 31° and 37 MV/cm for L = 3.019 Å) when $f_{int} = f_{bulk}$ is assumed.

APPENDIX C: ELECTRONIC POLYMERS IN LIPID MEMBRANES

This appendix is adapted with permission under a Creative Commons License from a previously published research article (P. K. Johansson, et al, *Sci. Rep.*, Vol 5, Issue 11242, pp 1-11, **2015**, DOI: 10.1038/srep11242).

C.1. SUMMARY

Electrical interfaces between biological cells and man-made electrical devices exist in many forms, but it remains a challenge to bridge the different mechanical and chemical environments of electronic conductors (metals, semiconductors) and biosystems. Here we demonstrate soft electrical interfaces, by integrating the metallic polymer PEDOT-S into lipid membranes. By preparing complexes between alkyl-ammonium salts and PEDOT-S we were able to integrate PEDOT-S into both liposomes and in lipid bilayers on solid surfaces. This is a step towards efficient electronic conduction within lipid membranes. We also demonstrate that the PEDOT-S@alkyl-ammonium:lipid hybrid structures created in this work affect ion channels in the membrane of Xenopus oocytes, which shows the possibility to access and control cell membrane structures with conductive polyelectrolytes.

C.2. UV-VIS, CONDUCTIVITY, AND ELECTROPHYSIOLOGY

We have hydrophobized PEDOT-S by creating electrostatic complexes of PEDOT-S and alkyl-ammonium salts, which can be dissolved in organic solvents with preserved doping and electronic conductivity. This was done by adding PEDOT-S dissolved in MilliQ (1 mg/mL) to 2.5 mM alkyl-ammonium salt solutions. The mixture was then heated briefly to ~60°C resulting in a precipitate that was centrifuged (10,000 g, 5 min) into a pellet. The supernatant was removed and excess alkyl-ammonium salt was removed by resuspension of the pellet in MilliQ (pH-adjusted with HCl) followed by repeated centrifugation steps. The final pellet was dried with N_2 gas and dissolved in chloroform:methanol (2:1), so that a final PEDOT-S concentration of 1 mg/mL was reached. Absorbance of the PEDOT-S@alkyl-ammonium complexes was measured with a UV-Vis spectrophotometer in the range 400 - 800 nm (Figure C.1).

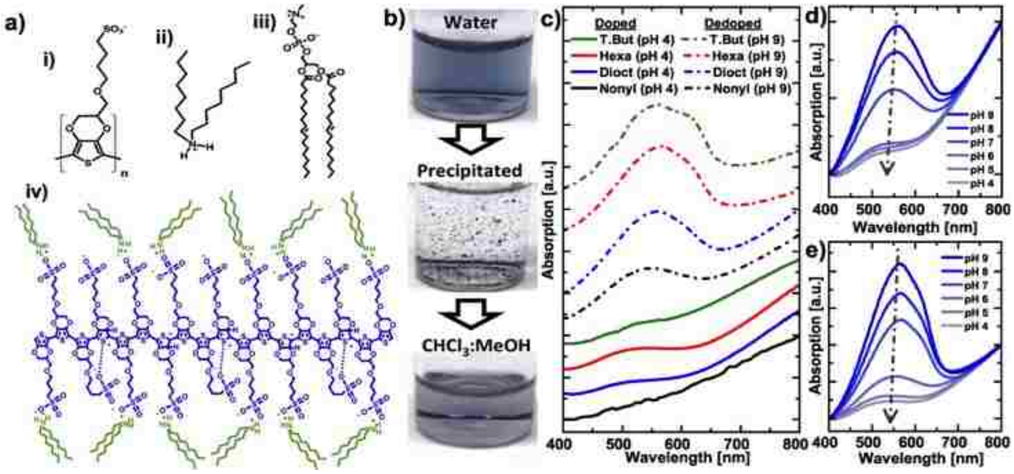

Figure C.1. Characterization of the PEDOT-S@alkyl-ammonium complexes. (a) i) The monomer of PEDOT-S, ii) dioctyl-ammonium chloride, iii) DOPC, iv) schematic of the complex. (b) PEDOT-S is soluble in water (top), but precipitates in 2.5 mM dioctyl-ammonium (middle) and the precipitate is soluble in $CHCl_3$:MeOH (bottom). (c) UV-vis spectra of complexes dissolved in $CHCl_3$:MeOH (2:1) after being precipitated from water solutions at pH 4 (solid) or pH 9 (dashed). The alkyl-ammonium salts used were tetrabutyl- (green), hexadecyl-trimethyl- (red), dioctyl- (blue) and nonyl-ammonium (black). Complexes from (d) dioctyl- and (e) hexadecyl-trimethyl-ammonium dissolved in $CHCl_3$:MeOH (2:1) were characterized after being precipitated from water solutions with pH in the range 9 - 4. The arrows indicate increased doping as the pH is decreased.

PEDOT-S@dioctyl-ammonium complexes were subsequently used to make P-S@dioct:DOPC structures by mixing with DOPC (1 mg/mL) in chloroform:methanol (2:1). By blowdrying with N_2 gas until the solvent was completely evaporated, a lipid cake was formed that was suspended in 2 mL PBS at pH 7.4. After swelling, the samples were extruded with polycarbonate membranes having 100 nm orifices. The structures were then adsorbed onto Au nanoelectrodes on silicon surfaces and the conductivity was measured with two probe measurements using a Keithley 4200 parameter analyzer. Structures extruded with 400 nm orifices were also adsorbed onto Pt films which had been sputtered onto SiO_2 substrates. Local electrical characterization was then conducted on the adsorbed structures in a Dimension 3100 (Bruker) microscope with a Nanoscope IV controller equipped with a C-AFM module (1 nA/V current sensitivity) and the results are presented in Figure C.2.

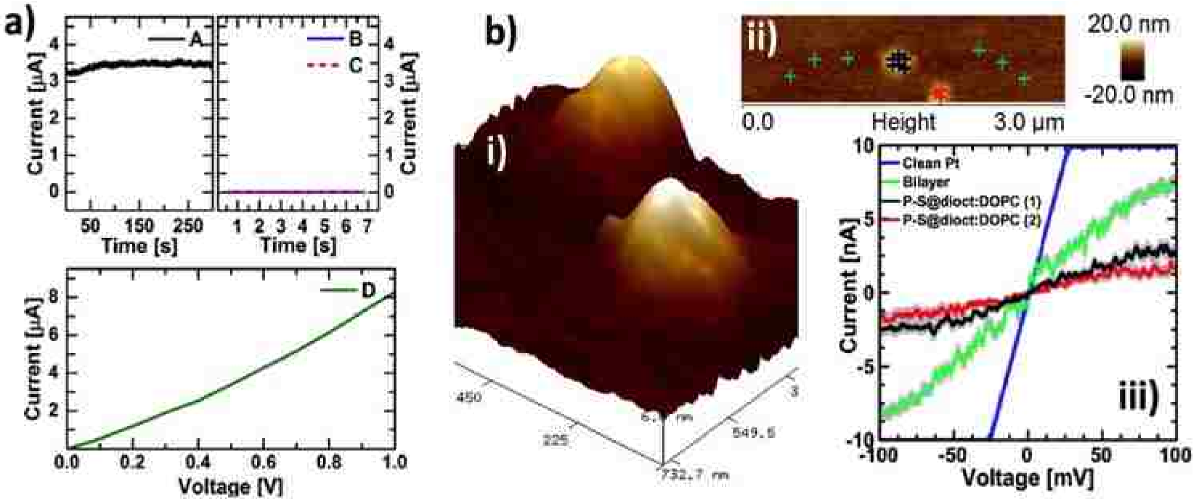

Figure C.2. Electrical characterization of P-S@dioct:DOPC structures. a) Supported lipid bilayers were prepared on nano-electrodes with 100 nm gaps, and 100 nm P-S@dioct:DOPC structures (500 µg/mL DOPC, 50 µg/mL PEDOT-S) were then adsorbed. A time-series during 300 s with 0.5 V applied voltage show stable electronic currents (A). References with either only lipid bilayers (B) or lipid bilayers treated with PEDOT-S dissolved in MilliQ (100 µg/mL) during 15 min (C) were not conductive and the measurements were terminated after 7s. (D) shows a voltage sweep for the P-S@dioct:DOPC structures between 0 - 1 V. b) 400 nm P-S@dioct:DOPC structures (500 µg/mL DOPC, 50 µg/mL PEDOT-S) were applied on Pt substrates and measured on by C-AFM. i) shows two representative 400 nm structures that had collapsed on the surface and had heights of 17 nm and 21 nm respectively. ii) shows the various spots that were measured and iii) shows the average currents in voltage sweeps between –100 to 100 mV for the two structures (17 nm black, 21 nm red), the surrounding lipid bilayer (green) and the clean Pt substrate (blue).

We also demonstrated effective quenching of the membrane dye Nile Red when it was included in the P-S@dioct:DOPC structures, which shows that PEDOT-S is closely coordinated in or on the liposome membranes (data not shown). This is a first demonstration of conductive lipid membranes with potential to carry electronic currents across the membrane as well as laterally over longer distances. Such electrical interfaces may have applications within many fields, such as biosensing, controlled release, directed cell growth and probing of bioprocesses - just to mention a few. We also demonstrated in this work that the produced structures can function as vehicles to deliver the metallic polythiophene PEDOT-S to the membranes of living cells, possibly by membrane fusion. When this was utilized on *Xenopus* oocytes with Shaker K channels expressed, the gating of these channels was modified (Figure C.3), which serves as an example that it is possible to access and control structures in the membranes of living cells with the electronic lipid:hybrid structures that we created. This is a major step towards incorporating these self-doped conductive polyelectrolytes into lipid membranes and thus create a new pathway to make conductive MMS and to achieve electronic access to redox active elements in biological systems.

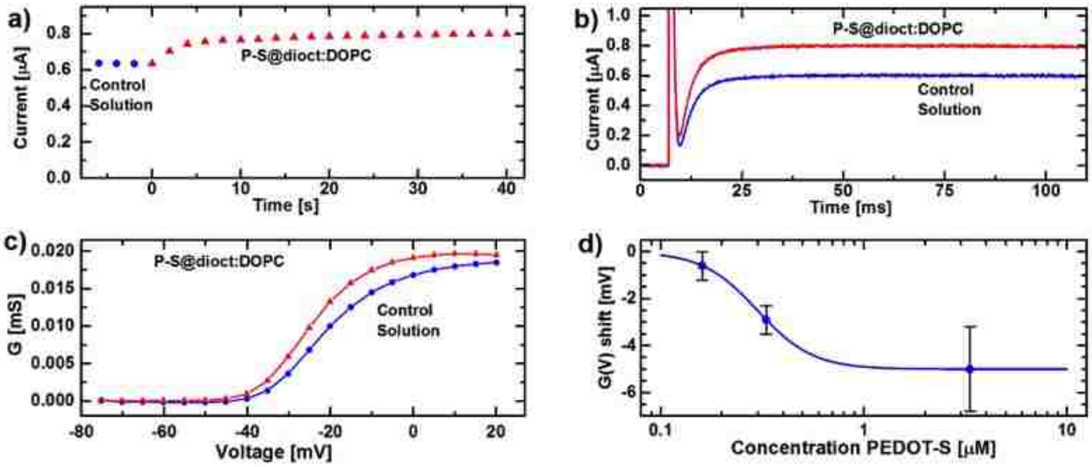

Figure C.3. SFG P-S@dioct:DOPC effect the on the Shaker K channel. (a) 0.33 µM P-S@dioct:DOPC applied to the extracellular solution increases the steady-state K$^+$ current at –20 mV. (b) Current traces at –20 mV from a holding voltage of –80 mV. (c) Steady-state K+ conductance vs. membrane voltage. (d) Dose-response curve of the induced shift.

APPENDIX D: EXPERIMENTAL DESIGN AND ANALYSIS OF ACTIVATORS REGENERATED BY ELECTRON TRANSFER-ATOM TRANSFER RADICAL POLYMERIZATION EXPERIMENTAL CONDITIONS FOR GRAFTING SODIUM STYRENE SULFONATE FROM TITANIUM SUBSTRATES

This appendix has been adapted with permission from a previously published research article (R. Foster, et al, *J. Vac. Sci. Technol. A.*, Vol 33, Issue 5, pp 05E131, **2015**, DOI: 10.1116/1.4929506). Copyright (2015) American Vacuum Society.

D.1. SUMMARY

A 2^4 factorial design was used to optimize the activators regenerated by electron transfer-atom transfer radical polymerization (ARGET-ATRP) grafting of sodium styrene sulfonate (NaSS) films from trichlorosilane/10-undecen-1-yl 2-bromo-2-methylpropionate (ester ClSi) functionalized titanium substrates. The process variables explored were: A) ATRP initiator surface functionalization reaction time; (B) grafting reaction time; (C) $CuBr_2$ catalyst concentration; (D) reducing agent (vitamin C) concentration. All samples were characterized using x-ray photoelectron spectroscopy (XPS). Two statistical methods were used to analyze the results: (1) Analysis of variance (ANOVA) with $\alpha = 0.05$, using average $\sqrt{Ti}$ XPS atomic percent as the response; (2) Principal component analysis (PCA) using a peak list compiled from all the XPS composition results. Through this analysis combined with follow-up studies, the following conclusions are reached: (1) ATRP-initiator surface functionalization reaction times have no discernable effect on NaSS film quality; (2) minimum ($\leq$ 24 hr for this system) grafting reaction times should be used on titanium substrates, since NaSS film quality decreased and variability increased with increasing reaction times; (3) minimum ($\leq$ 0.5 mg cm^{-2} for this system) $CuBr_2$

concentrations should be used to graft thicker NaSS films; (4) no deleterious effects were detected with increasing vitamin C concentration.

D.2. THIN FILM CHARACTERIZATION WITH SFG

SFG spectra were measured with a ps-pulsed laser system (EKSPLA, Nd:YAG and OPA/OPG/DFG). Spectra were collected for ClSi films on Ti surfaces, prepared during 1 day and 7 days respectively, in order to determine the effect of reaction time on the ClSi film quality. The incident angles relative the surface normal were 60° and 62° for the infrared (IR) and visible beams, respectively. The *ppp* (*p*-polarized SFG, *p*-polarized visible and *p*-polarized IR) polarization combination was used for all spectra. Average data acquired from three replicates of each sample (1 day and 7 days) were analyzed for each spectral region (ester: 1700 - 1800 cm^{-1} and C-H: 2800 - 3000 cm^{-1}) - with one exception (7 days, ester region: 1700-1800 cm^{-1}) where average data acquired from four replicates were analyzed. For the ester region, a step size of 1 cm^{-1} was used with 600 acquisitions per step, while a step size of 2 cm^{-1} and 400 acquisitions per step were used for the C-H region. In order to compensate for variations in IR and visible intensities throughout the spectra, all data points were normalized against signals produced in parallel from an SFG-active crystal (ZnS) that were captured simultaneously in a reference channel similar to the one used for the SFG signals from the samples. The spectra captured in the ester region were fitted with Eq. D.1, while the C-H_x spectra are presented without fits.

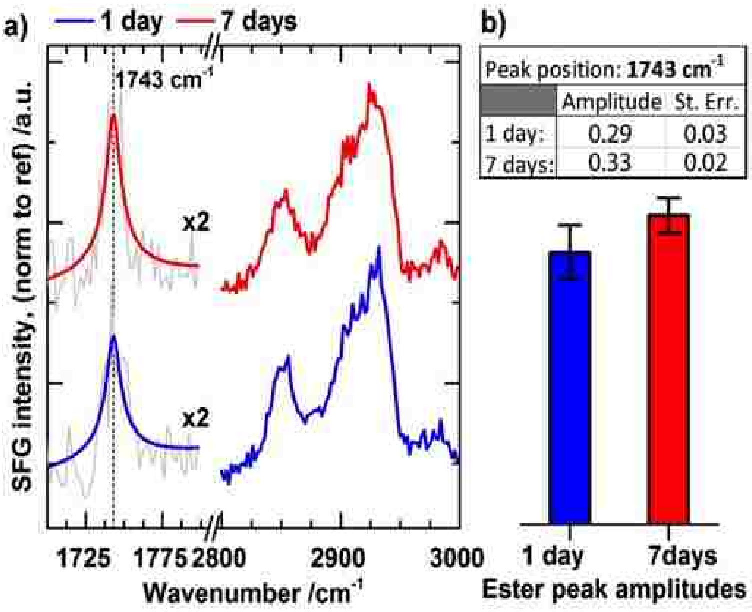

Peak position: 1743 cm^{-1}		
	Amplitude	St. Err.
1 day:	0.29	0.03
7 days:	0.33	0.02

Figure D.1. SFG spectra for ClSi films synthesized over 1 day (blue) and 7 days (red), respectively. For the ester region at 1743 cm^{-1}, the grey graphs are averaged data, while the blue and red graphs are fits. The vertical line at 1743 cm^{-1} denotes the peak position for the fits. For the C-H region only the averaged data are presented. The amplitudes of the fits in the ester region, with standard errors of the fits, are included in the table and bar-plot. The data indicate that the films prepared during for 1 day and 7 days reaction times are of similar quality.

In order to compare ClSi films prepared on Ti during 1 and 7 days reaction times, SFG spectra in the C-H and ester regions were recorded (Figure D.1). For a film such as ClSi, the relative spectral contributions of methyl and methylene vibrations in the C-H region (2800 - 3000 cm^{-1}) are related to the conformation of the alkane chains. A perfectly ordered alkane chain with the methylene groups in an all-*trans* conformation have a center of inversion in between the methylene groups, which do not appear in the spectra. In such a scenario, the C-H spectral region would be dominated by SFG signals from the terminal methyl vibrations. However, our results show that peaks from methylene vibrations (around 2855 cm^{-1} for symmetric and around 2920 cm^{-1} for asymmetric vibrations) dominate the C-H region, indicating that the alkane chains inhere gauche defects. Most importantly, the spectra for 1 and 7 days reaction times overlap almost perfectly showing that no significant change in molecular conformation is observable by SFG. We also measured the SFG spectra for the ester region (1700-1800 cm^{-1}) and detected the carbonyl stretching peak of the ester group at 1743 cm^{-1}, which confirms partial ordering of the ester group. In order to quantitatively compare the spectral intensities in the ester region for the 1 and 7 days reaction times, the spectra were fitted with

$$\chi_{SFG}^{(2)} = \chi_{NR}^{(2)} + \sum_q \frac{A_q}{\omega_q - \omega_{IR} - i\Gamma_q} \qquad \text{(D.1)}$$

where $\chi_{SFG}^{(2)}$ is the second order susceptibility; $\chi_{NR}^{(2)}$ is the non-resonant part; A_k, ω_k, Γ_k are the peak amplitude, peak wavenumber, and damping factor (peak width) for the k_{th} IR and Raman active vibration; and ω_{IR} is the IR wavenumber. The ester peak fits for 1 (blue) and 7 (red) days reaction times are presented in Figure D.1, in which the bar plot displays the value of the peak amplitudes from the two fits. Although the mean values are slightly different, the errors are overlapping. This, in conjunction with the striking similarity of the spectra in the C-H region, provides further evidence that the ClSi films prepared during 1 and 7 days reaction times are similar. As mentioned above, this conclusion is consistent with the results from the XPS and AFM experiments. It is therefore unlikely that an increased ClSi reaction time is leading to an improved NaSS film quality.

VITA

Patrik Johansson was born in Avesta, Sweden, in 1988. In 2005, he moved to Forsmark, near Östhammar, for his high school education. While attending Forsmark's High School, which he graduated from in 2007, Patrik was inspired by his teacher in biology who held a Ph.D. in biophysics. This prompted him to enroll in a Master of Science and Engineering program in engineering biology at Linköping University in 2007. While at the university, Patrik was heavily engaged in student affairs and took a sabbatical during 2010 – 2011 in order to work full-time for the student union as the head of corporate relations. The studies in Linköping stimulated Patrik's interest for biomaterials surface analysis, which lead him to perform the diploma work for his M.Sc. degree at NESAC/BIO at the University of Washington (UW) in Seattle, during the spring 2013 under the joint supervision of Dr. Patrick Koelsch and Prof. David G. Castner. Patrik earned his M.Sc. degree in the summer of 2013 and thereafter applied to the Ph.D. program in bioengineering at the UW. After working in Prof. Olle Inganäs' lab for biomolecular and organic electronics and a second visit at the UW during the spring 2014, he began his graduate studies towards a Ph.D. degree at NESAC/BIO in the autumn 2014, again under the supervision of Dr. Koelsch and Prof. Castner. When not thinking about science, Patrik enjoys long-distance running, playing squash, and watching movies.